Dissertation

submitted to the

Combined Faculty of Mathematics, Engineering, and Natural Sciences

of Heidelberg University, Germany

for the degree of

Doctor of Natural Sciences

Put forward by

Minjung Kim

born in: Seoul, South Korea

Oral examination: 31 May 2022

Measurement of prompt and non-prompt J/ψ production

in p–Pb collisions at $\sqrt{s_{\mathrm{NN}}}$ = 8.16 TeV with ALICE at the LHC

Referees: Prof. Dr. Johanna Stachel

Prof. Dr. Ulrich Uwer

Abstract

Heavy quarks (charm and beauty) are essential probes of the quark-gluon plasma (QGP), a hot and dense medium created in heavy-ion collisions. Since the heavy-quark production in high-energy collisions occurs earlier than the formation time of the QGP, heavy quarks witness the whole evolution of the QGP. Measurements in proton–nucleus (pA) collisions provide the genuine testing ground to study possible modifications of heavy-quark production in the presence of a nucleus, which is necessary information to interpret the measurements in heavy-ion collisions. A valuable observable is the production of J/ψ mesons, a bound state of a $c\overline{c}$ pair. Their production can be prompt, meaning that they are either produced directly or from the decay of heavier charmonium states, or it can be non-prompt when originating from the decay of beauty hadrons. Therefore, a measurement of J/ψ which separates these contributions allows one to study charm and beauty quark production simultaneously. In this thesis work, the J/ψ meson production was measured in p–Pb collisions at $\sqrt{s_{\mathrm{NN}}}$ = 8.16 TeV using a high-p_{T} electron enriched data sample collected using the Transition Radiation Detector (TRD). Based on the electron identification and tracking capabilities of the ALICE detector at the LHC, the J/ψ mesons are reconstructed in the dielectron decay channel at midrapidity. Relying on the long lifetime of beauty hadrons, prompt and non-prompt J/ψ contributions are separated on a statistical basis. The resulting p_{T} dependent nuclear modification factors (R_{pA}) of prompt and non-prompt J/ψ are consistent with unity within measured uncertainties at midrapidty in $2 < p_{\mathrm{T}} < 14$ GeV/c. Further, the results are described by theoretical calculations that include cold-nuclear-matter effects in p-Pb collisions. Thus, the result suggests a small impact of cold-nuclear-matter effects for charm and beauty quarks in the measured kinematic region.

Kurzfassung

Schwere Quarks (Charm und Beauty) sind äußerst wichtige Sonden für das Quark-Gluon Plasma (QGP), ein Medium aus heißer und dichter Materie, welches in Schwerionenkollisionen erzeugt wird. Da die Produktion schwerer Quarks in hochenergetischen Kollisionen vor der Ausbildung des QGP stattfindet, erleben die schweren Quarks die gesamte Entwicklung des QGP. Messungen in Proton-Kern(pA)-Kollisionen bieten eine gute Gelegenheit, mögliche Modifikationen in der Produktion schwerer Quarks in Anwesenheit eines Kerns zu untersuchen, was eine Voraussetzung für die Intepretation der Daten in Schwerionenkollisionen ist. Eine Wertvolle Messgröße ist die Produktion von J/ψ-Mesonen, ein gebundener Zustand eines $c\overline{c}$-Paares. Deren Produktion kann entweder "prompt" stattfinden, was bedeutet dass sie entweder direkt oder aus dem Zerfall schwererer Charmoniumzustände erzeugt werden oder aber "non-prompt" wenn sie aus dem Zerfall von Beautyhadronen resultieren. Eine J/ψ-Messung, die diese Beiträge voneinander trennt, gibt daher Einblicke in die Charm- und Beautyproduktion gleichzeitig. Für diese Arbeit wurde die J/ψ-Produktion in p–Pb-Kollisionen bei sNN= gemessen, wobei ein elektronenangereichterter Datensatz verwendet wurde, der mit Hilfe des Übergangsstrahlungsdetektors (TRD) aufgenommen wurde. Geleitet von den Fähigkeiten des ALICE-Detektors am LHC, wurden J/ψ-Mesonen im Dielektronenzerfallskanal bei mittleren Rapiditäten rekonstruiert. Basierend auf der langen Lebensdauer der Beautyhadronen wurden die "prompt" und "non-prompt" Beiträge auf statistischer Basis getrennt. Die resultierenden nuklearen Modifikationsfaktoren (R_{pA}) für diese Beiträge zeigen keine statistisch signifikante Abweichung von 1 für die Messung bei mittlerer Rapidität im Bereich $2 < p_{\mathrm{T}} < 14$ GeV/c. Die Messungen werden auch von theoretischen Rechnungen beschrieben, welche Effekte kalter Kernmaterie modellieren. Die Ergebnisse deuten daher auf einen geringen Einfluss der Effekte von kalter Kernmaterie auf Charm und Beautyquarks in der gemessenen kinematischen Region hin.

Contents

1 Introduction

1.1 Strong interaction and quantum chromodynamics (QCD)

Physics is part of the science that deals with the structure of matter and the interactions between the fundamental constituents of the observable universe [1]. As science and technology have evolved over times, it has become possible for Physicists to explore smaller length scale, far beyond what is visible to the naked eyes. A length scale of femtometre (10^{-15} m) was firstly reached in Rutherford gold foil experiment in 1911, which discovered the existence of the nucleus [2]. Eventually, by the discovery of the neutron in 1932, it became evident that the nucleus is built up of protons and neutrons with the presence of a force that holds them together [3]. The idea of strong interaction was firstly emerged by Yukawa, proposing the force to explain the interaction between protons and neutrons [4]. The existence of the middle-weight particle, in the range between the mass of electrons and of protons, was predicted as a mediator, a meson. Starting from the discovery of the π meson in cosmic rays in 1947 [5], a lot more strongly interacting particles, so called hadrons, were discovered over decades, opening the era of the particle zoo. Among them, the discoveries of kaon [6] and Λ [7] particles inspired theoretical physicists including Gell-Mann and Nishijima, introducing another quantity, called "strangeness", which is conserved in strong interactions but not in its decays, to distinguish particles together with spin and parity [8, 9].

In 1961, a new classification of hadrons according to their charge and strangeness, the so-called eightfold way, was suggested independently by Gell-Mann and Ne'eman [10] with an underlying approximate (broken) symmetry of the group SU(3) extended from the SU(2) isospin symmetry of the interaction between the proton and neutron as suggested by Heisenberg [11]. The eightfold way could predict the existence of the Ω^- particle before its actual discovery via the measurement [12]. Followed by the eightfold way, finally in 1964, what now called "quark" was independently proposed as a basic building block of hadrons by Gell-Mann [13] and Zweig [14]. Initially, three types of quarks (u, d, s), were introduced. Quarks are spin $\frac{1}{2}$ Dirac fermions carrying fractional charges, baryon number of $\frac{1}{3}$ and by convention, positive parity. The properties of quarks are listed in Table 1.1 [15]. Every baryon (antibaryon) is composed of three quarks (antiquarks) and every meson is made up of a quark and an antiquark. The quark model, however, had two main challenges to become a concrete theory. Firstly, some baryons, such as (Δ^{++} and Ω^-) composed of three quarks of identical quantum numbers, showed the anomaly of the spin-statistics theorem which implies that quark, as a fermion, should obey the Pauli exclusion principle [16]. As a consequence, the new quantum number for strongly interacting particles, so-called "colour" (red (r), green(g), blue(b)), was introduced by Greenberg in terms of a para-statistics model [17] and later by Han and Nambu, introducing double SU(3) symmetry [18]. The introduction of "colour"

Table 1.1: List of quarks and their properties [15]

		up (u)	down (d)	strange (s)	charm (c)	beauty (b)	top (t)
Q	: electric charge	$+\frac{2}{3}$	$-\frac{1}{3}$	$-\frac{1}{3}$	$+\frac{2}{3}$	$-\frac{1}{3}$	$+\frac{2}{3}$
I	: isospin	$\frac{1}{2}$	$\frac{1}{2}$	0	0	0	0
I_z	: isospin z-component	$+\frac{1}{2}$	$-\frac{1}{2}$	0	0	0	0
S	: strangeness	0	0	-1	0	0	0
C	: charm	0	0	0	+1	0	0
B	: bottomness	0	0	0	0	-1	0
T	: topness	0	0	0	0	0	+1

suggested the simple hypothesis of strongly interacting particles that all particles measured are colourless, which can explain that there are certain possible combinations of quarks to form hadrons. The another difficulty of the quark model was that quarks are never seen as single isolated objects. In addition to the fractional charge of quarks, this arose the question, whether quarks are real existing objects or just virtual particles for mathematical convention. The existence of quarks as point-like constituents of hadrons got supported by the results from a series of electron-proton scattering experiments at the Stanford Linear Accelerator Center (SLAC) by the MIT-SLAC collaboration from 1967 through 1973 [19]. The momentum transfer dependence of the measured scattering cross section showed strikingly different behaviour from what is expected for the elastic scattering of electrons at protons. Especially, the measured proton structure function satisfied the conjecture of Bjorken, so-called a (approximate) "scaling" behaviour, which should be appeared in the scattering of electrons on quasi-free and point-like constituents inside the protons [20]. Then, the discovery of J/ψ and, as a consequence, the charm quark showed crucial evidence of quarks as basic building blocks composing hadrons [21, 22].

The significance of the MIT-SLAC experiments was not merely the discovery of quarks, but also on the emergence of quantum chromodynamics (QCD), inspiring the discovery of asymptotic freedom in particular. Based on the advent of quantum field theories including the renormalizability of Yang-Mills theory studied by Hooft [23], a non-Abelian gauge theory with symmetry group of colour SU(3) emerged to describe the strong interaction in the early 70's [24, 25]. In QCD, the spin-1 massless coloured particles called "gluons" couple to the colour charges of quarks and gluons themselves and describe the dynamics of colour fields. The fundamental coupling underlying the interactions of quarks and gluons is expressed by the strong coupling constant α_s. A renormalization scale μ, a subtraction point for ultraviolet divergences, is introduced to describe a dimensionless physical quantity R in a renormalizable quantum field theory as a perturbation series in the coupling α_s. A dimensionless physical quantity R, however, should be invariant under change of an arbitrary scale. This requirement can be mathematically written by [26],

$$\mu^2 \frac{d}{d\mu^2} R(Q^2/\mu^2, \alpha_s) \equiv [\mu^2 \frac{\partial}{\partial \mu^2} + \mu^2 \frac{\partial \alpha_s}{\partial \mu^2} \frac{\partial}{\partial \alpha_s}] R = 0. \tag{1.1}$$

Choosing $\mu^2 = Q^2$ explicitly yields α_s to be a function of Q^2, running constant $\alpha_s(Q^2)$ as any dependence of R on the scale μ should be cancelled. The running of the coupling constant α_s is determined through the renormalization group equation,

$$Q^2 \frac{\partial}{\partial Q^2} \frac{\alpha_s(Q^2)}{4\pi} = \beta(\alpha_s(Q^2)). \tag{1.2}$$

The formula of the β-function in high momentum transfer regime (UV) is given as a perturbative series [27],

$$\beta(\alpha_s) = -(\frac{\alpha_s}{4\pi})^2 \sum_{n=0} (\frac{\alpha_s}{4\pi})^n \beta_n, \tag{1.3}$$

with the first term of β-series,

$$\beta_0 = 11 - \frac{2}{3} n_f, \tag{1.4}$$

where n_f is the number of quark flavours active at the scale Q^2 [28, 29]. The α_s decreases at high momentum transfer, where β_0 is positive for $n_f \leq 16$. This is one of the most important properties of QCD, so-called asymptotic freedom. The Q^2 dependent running coupling can be explicitly obtained by solving Equation 1.3 in full series, but exact analytical solution is known for β_0 order [27],

$$\alpha_s(Q^2) = \frac{4\pi}{\beta_0 \ln(Q^2/\Lambda^2)}, \text{ where } \Lambda^2 \equiv \mu^2 e^{-\frac{4\pi}{\beta_0 \alpha_s(\mu^2)}}. \tag{1.5}$$

A dimensional parameter Λ reflects the energy scale where the coupling strength diverges, giving the limits between the perturbative and non-perturbative domain. Due to the ambiguity of Λ, using the fixed energy scale, such as the mass of the Z boson, has become popular. Equation 1.5 gives α_s to decrease with increasing Q^2 so that quarks and gluons are asymptotically free, which is agreed with the conjecture of Bjorken explaining MIT-SLAC data discussed above. In opposite direction, the decreasing of Q^2 leads α_s to increase, indicating that coloured objects are confined in the colourless compound, the confinement. In addition, the smaller coupling strength for high momentum transfers or at short length scale allows the perturbative description of physical quantities in a language of QCD. Figure 1.1 presents the up-to-date world average α_s based on measurements at the scale of the Z-boson mass, as a function of Q^2 showing excellent agreement with numerous measurements of α_s in a wide energy range from various processes.

Over decades, various studies both in theoretical and experimental side have made QCD as a genuine theory of strong interaction. One of the remarkable progresses was the discovery of gluon in three-jet structure from the gluon bremsstrahlung in e^+e^- collisions [31] at the PETRA collider at DESY [32]. In addition, the lattice QCD calculation introduced by Wilson has been developed, opening opportunity to access physical quantities in the non-perturbative regime by numerically evaluating the theory in discretized space-time lattice [33].

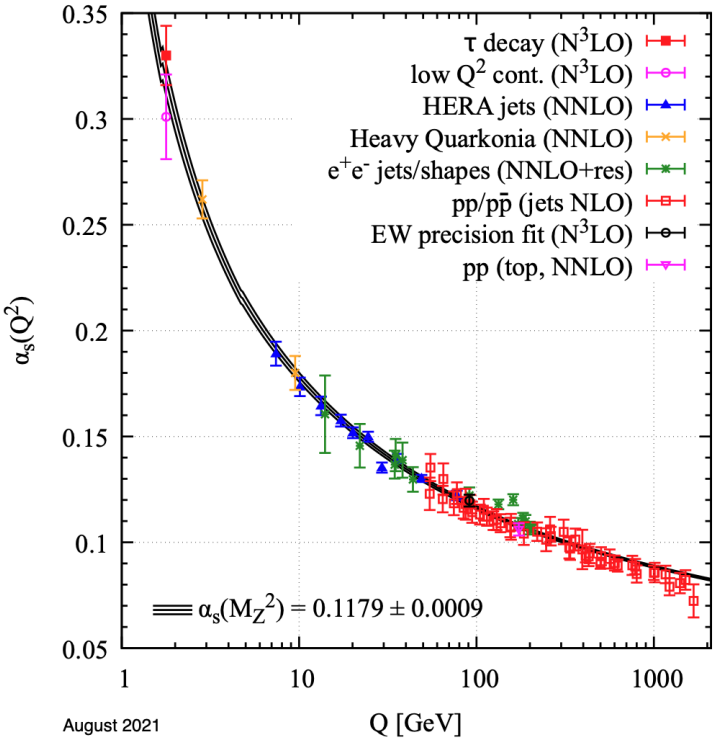

Figure 1.1: Running of the QCD coupling α_s as a function of momentum transfer Q^2. Measurements (shown as points) are compared with a world average α_s based on measurements at the scale of the Z-boson mass. The order to which perturbation theory is used is indicated in parentheses, further details can be found in [30], where the figure is taken from.

1.2 Quark-gluon plasma (QGP) and heavy-ion collisions

Soon after the discovery of the asymptotic freedom, Collins and Perry [34] and Cabibbo and Parisi [35] independently recognized its consequence for the existence of a new phase of QCD matter in extreme conditions, at sufficiently high pressure and/or temperature. The idea of Collins and Perry was that the interaction between quarks and gluons weakens as they get closer at sufficiently high density, and eventually these quarks are no longer confined inside the hadrons. The conjecture of Cabibbo and Parisi was started from the Hagedorn temperature, the highest temperature for the hadronic matter, obtained from the statistical bootstrap model [36]. They interpreted the existence of the Hagedorn temperature as the signature of a phase transition between hadronic matter and a deconfined state of quarks and gluons. The deconfined state of quarks and gluons is called the quark-gluon plasma [37]. The existence of a QCD phase transition was expected also from chiral symmetry of the massless quark QCD Lagrangian. In this point of view, the chiral symmetry is spontaneously broken at zero temperature and should be restored at high temperature [38]. The result from lattice QCD calculations supports that deconfinement and chiral symmetry restoring occurs at the same point at vanishing baryon chemical potential ($\mu_B = 0$). Moreover, lattice QCD calculations give a smooth cross over phase transition with the pseudo critical temperature of 156.5 ± 1.5 MeV at small μ_B [39]. The current understanding of QCD phases is illustrated in Figure 1.2 as a schematic phase diagram as a function of temperature (T)

and net baryon density (μ/μ_0). As discussed, at small μ/μ_0 and high T, crossover transition between hadron gas and quark-gluon plasma is presented.

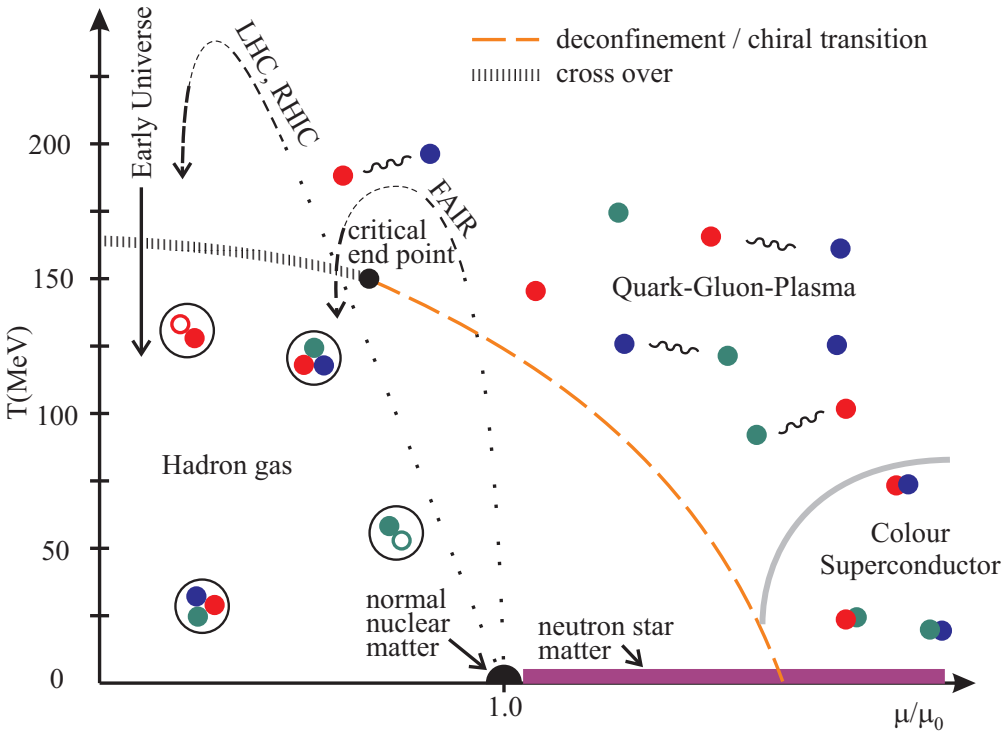

Figure 1.2: The phase diagram of QCD matter as a function of net baryon density (μ/μ_0) presented on the horizontal axis and temperature (T) on the vertical axis. The curvatures with arrows indicate the region where the corresponding collider experiments probe. Figure taken from [40].

The idea of creating and studying the quark-gluon plasma in a laboratory via colliding heavy nuclei at high energy emerged, expecting that energy density exceeds the normal typical hadronic value ($\approx 1.0\,\mathrm{GeV/fm^3}$) [41, 42, 43]. The space-time evolution of ultra-relativistic heavy-ion collision is schematically sketched in Figure 1.3. The light cone of the collision is defined by lines of the constant proper time of the particle $\tau = \sqrt{t^2 - z^2}$. The formation time of the QGP can be roughly estimated from the QCD scale $\tau_0 \approx 1/\Lambda_{\mathrm{QCD}}$, resulting proper time $\tau_0 \leq 1\ \mathrm{fm}/s$. The system reaches the local thermal equilibrium and evolves via expansion following the viscous relativistic hydrodynamics. Once the system, the QGP medium, cools down and reaches below critical temperature T_c, the system has to become hadron gas. The chemical freeze-out temperature T_{ch} is defined as where inelastic collisions between the constituents no longer continue so that the hadronic composition of the system becomes fixed. Similarly, the kinetic freeze-out temperature T_{fo} indicates the temperature where no further elastic collisions between the constituents (hadron) happen so that the momenta of the hadrons become fixed.

The first glimpse of the QGP was provided by collisions of lead beams at the SPS (Super Proton Synchrotron) in the late 90's [45]. The suppression of charmonimum states production in Pb–Pb collisions with respect to p–Be collisions was observed [46], which was proposed as a smoking gun of the QGP as a consequence of color screening in the QGP medium keeping charmed quark-antiquark pairs from

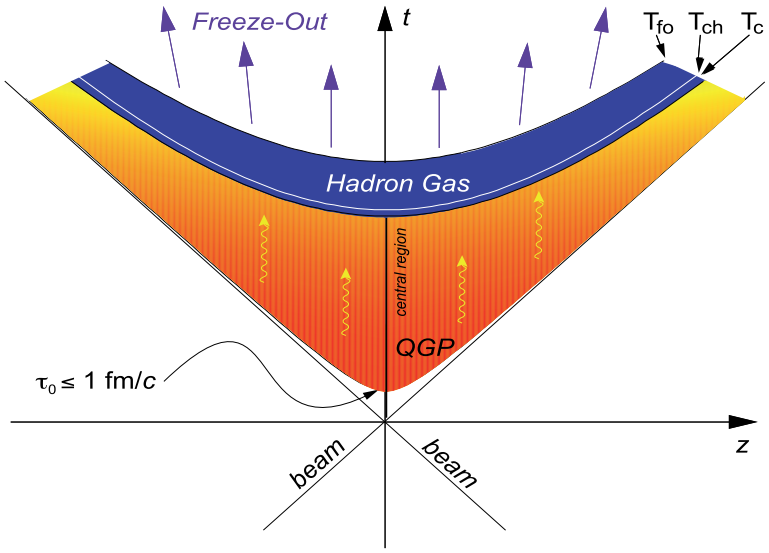

Figure 1.3: The schematic sketch of the space time evolution of ultra-relativistic heavy-ion collision. The time (t) and space direction (z) are presented on the vertical and horizontal axis, respectively. Figure taken from [44].

binding to each other [47]. The production enhancement of hadrons containing strange quarks in Pb–Pb collisions relative to p–Pb collisions was as well observed [48]. The strangeness pair production threshold in the QGP medium, is given by twice of the strange quark mass at parton level. As this threshold is much smaller compared to the energy threshold of the strange production in the initial hadronic interactions (e.g. $p + p \rightarrow p + K^+ + \Lambda$) and in indirect production in hadronic gas via re-scattering (e.g. $\pi + N \rightarrow K + \Lambda$), the presence of the QGP leads the enhancement of strangeness production. More clear evidence of the QGP could be found at RHIC (Relativistic Heavy Ion Collider). A strong suppression was observed for hard probes, which are predominately created in the initial hard scattering before the QGP formation, including heavy flavour-hadrons and jets [49, 50]. This suppression was the one of the early predicted QGP signatures due to the energy loss of partons in the medium [51]. At the same time, the collective flow of particles, which arises from the combination of pressure gradients in the medium and partonic energy loss within the QGP at high transverse momentum, was observed as anisotropic flow (v_n) [52]. The measured flow exhibited the "perfect" fluid like behavior described by ideal relativistic hydrodynamics, indicating a strongly coupled quark-gluon Plasma (sQGP) [53]. The highest beam energy has been reached in heavy-ion collisions at the LHC (Large Hardon Collider), resulting in significantly larger cross sections of hard-scattering processes compared to RHIC. As a consequence, more differential measurements in a larger kinematic range have been carried out by experiments at the LHC which are crucial inputs for understanding the characteristics of the QGP [54].

1.3 Small collision systems

Small collision systems hereafter refer to collisions of proton–proton and proton (deuteron)–nucleus collisions. Small collision systems are a part of the heavy–ion physics program as they are expected to be free from the QGP medium, i.e. hot nuclear matter effects. Measurements of proton–proton

collisions are crucial as a benchmark for the measurements in heavy-ion collisions, especially for the case that observables cannot be calculated precisely from theories in pp collisions. For this reason, various measurements in pp collisions can as well contribute to theoretical developments.

Collisions of proton (deuteron)–nucleus take a role as a proxy to disentangle the so-called cold nuclear matter effects, the effects arising from the presence of a nucleus, from genuine final state QGP effect. For example, the modification of parton distribution functions (PDFs) for nuclei from those of the free nucleon are reflected in several nuclear effects as illustrated in Figure 1.4. The horizontal axis of

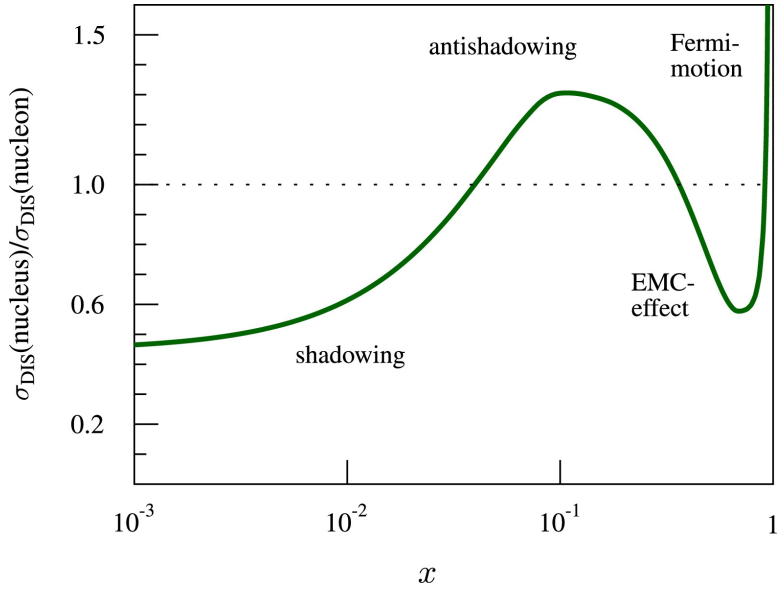

Figure 1.4: The schematic sketch of typical nuclear effects in the deeply inelastic scattering (DIS) as a function of x for a given fixed Q^2. Figure taken from [55].

Figure 1.4 shows the dimensionless Bjorken scaling variable x, referring to the fraction of momentum carried by the parton inside nucleon with respect to the nucleon momentum. The vertical axis presents the ratio of deeply inelastic scattering (DIS) cross sections between the one from nucleus and free nucleon case, at fixed four-momentum transfer Q^2. Thus, the vertical axis represents the partonic nuclear modification factor. At small values of x, $x < 0.05$, the partonic nuclear modification factor is smaller than 1 and gets smaller as x decreases, which is the so-called shadowing effect, occurring in high-density systems when gluons from nearby nucleons interact [56]. The enhancements is shown in between $0.1 < x < 0.3$, namely the antishadowing region, which compromises the shadowing effect following momentum conservation. In the region of $0.3 < x < 0.8$, the depletion of partonic nuclear modification factor is experimentally observed, named EMC effect [57]. Finally, the region close to $x \approx 1$, the motion of nucleons in the nucleus (Fermi motion) causes the enhancement. The measurements in proton–nucleus collisions provide valuable input for constraining nuclear PDFs as well as a native environment to study possible modifications of particle production due to the modification of the nuclear PDFs. Nuclear modifications for quarks and gluons in lead nuclei obtained by the EPPS16 [58] and nCTEC15 [59] parameterization are presented in Figure 1.5. The large uncertainty is seen in all nPDF distributions at low x range, in particular. As illustrated in Figure 1.6, the four LHC experiments in p-Pb

collisions provide the accessibility of wide kinematic region in $x - Q^2$. For example, depending on Q^2, which is relevant for particles produced in the collisions, the ALICE muon spectrometer permits to access the x between 10^{-5} to 10^{-3} and 10^{-3} to 10^{-1}. And the ALICE central barrel detector provides the range around $x \sim 10^{-3}$. Therefore, the measurements from the four LHC experiments will be useful inputs for constraining and reducing the uncertainty of the nPDFs at low x range. Depending on physical observables, there are other possible initial state effects proposed from the theoretical side. The theories related to this thesis work will be discussed in detail in Chapter 2.

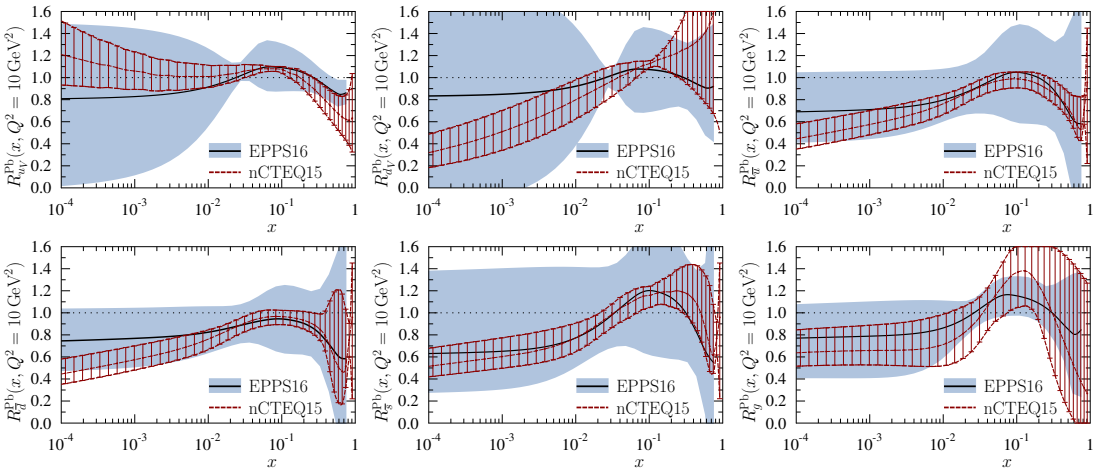

Figure 1.5: The EPPS16 nuclear modifications for valence u and d quarks (R^{Pb}_{uV}, R^{Pb}_{dV}), sea u, d, s quarks ($R^{Pb}_{\bar{u}}$, $R^{Pb}_{\bar{d}}$ and $R^{Pb}_{\bar{s}}$) and gluon ($R^{Pb}_{\bar{g}}$) for lead at the parametrization scale of $Q^2 = 10$ GeV^2 with those from the nCTEC15 analysis [58, 59]. Figure taken from [58].

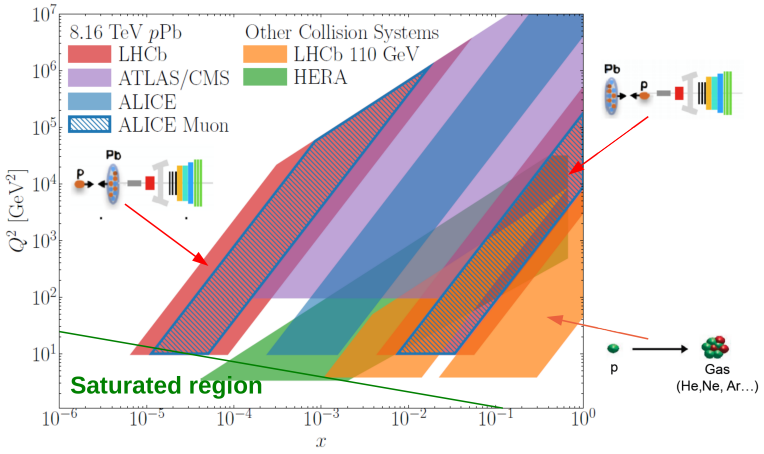

Figure 1.6: Kinematic coverage of the four LHC experiments in p–Pb collisions at $\sqrt{s_{\rm NN}}$ = 8.16 TeV considering corresponding acceptance of the each detector. Figure taken from [60].

One of striking results from early LHC measurements is the observation of a ridge like structure in pp collisions by the CMS collaboration [61]. Figure 1.7 shows the two-particle angular correlation in relative pseudo-rapidity ($\Delta\eta$) and relative azimuthal angle in the transverse plane ($\Delta\phi$) of two particles measured in pp collisions for low and high track multiplicity [62] and in p–Pb and Pb–Pb collisions [63]. The clear ridge-like structures around $\Delta\phi \approx 0$ along the $\Delta\eta$ are seen for all collision systems except for

the low multiplicity pp collisions. Naturally, this has raised the question whether the collective behavior observed in small collision systems is from the same origin as in heavy-ion collisions, the hydrodynamic response of QGP medium to the energy density gradients in the initial state. The interpretation of the collectivity observed in the small system is not obvious since there are various sources which can generate the angular correlation between particles, such as resonance decays and jet fragmentation [64]. Moreover, in the theoretical point of view, the application of the hydrodynamics for small, thermally non-equilibrium system has only recently started [65, 66]. A complete understanding of the collective phenomena discovered in small systems is not yet clear and detailed studies are needed both from the theory and experimental sides.

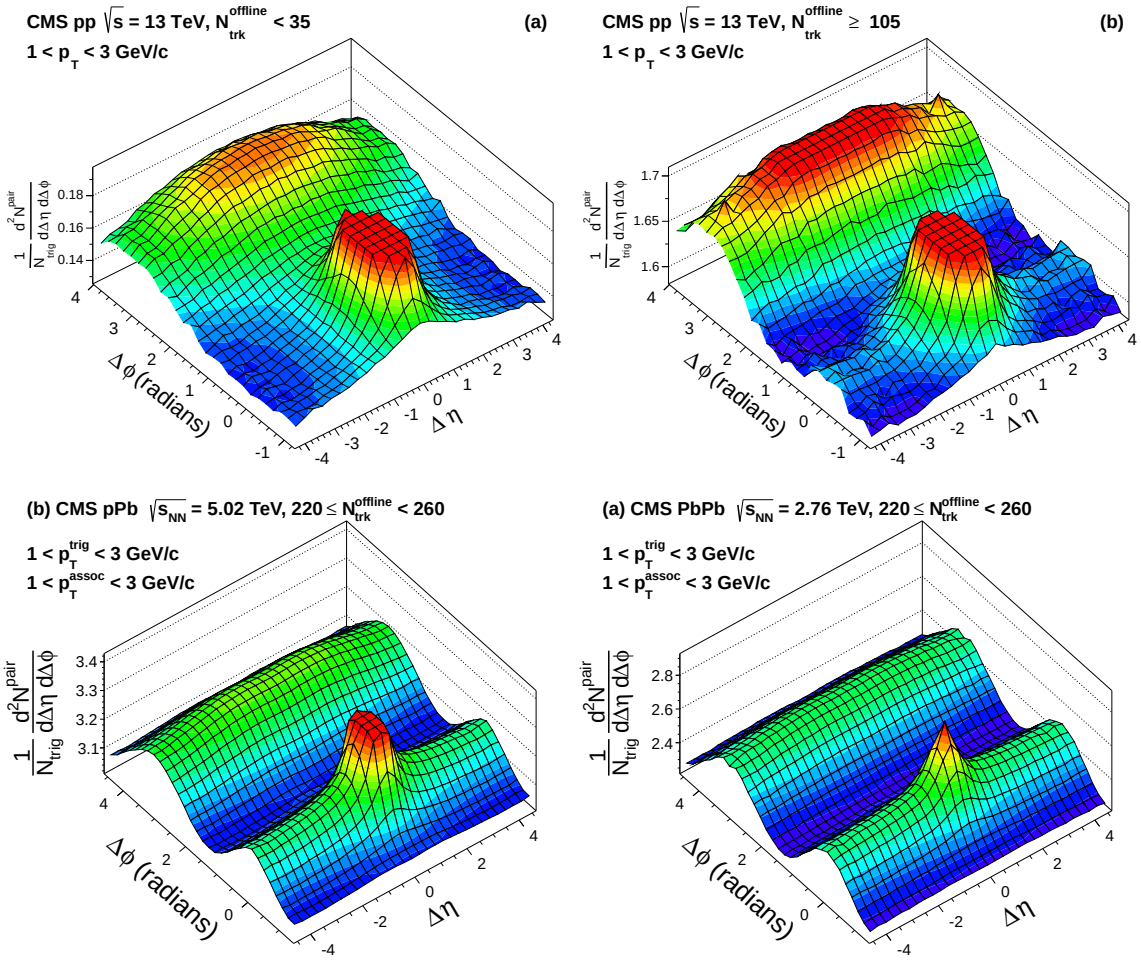

Figure 1.7: Two-particle angular correlation functions in relative pseudo-rapidity ($\Delta\eta$) and relative azimuthal angle ($\Delta\phi$) in pp [62] (upper left: low multiplicity events, upper right: high multiplicity events), p–Pb (bottom left) and Pb–Pb collisions (bottom right) [63] measured by the CMS collaboration at the LHC.

2 Heavy-flavour and quarkonium production in hadronic collisions

Due to the large masses of charm and beauty quark (m_Q) compared to $\Lambda_{\rm QCD}$ and to the typical temperature reached in the ambient medium ($T_{\rm QGP}$) [42], heavy quarks are primordially produced in initial hard partonic scattering processes in heavy-ion collisions. The time scale of heavy quarks production is estimated by the inverse of the virtuality of the hard scattering (Q), $\Delta\tau \sim 1/Q$. The minimum virtuality of heavy quark pair production, $2 \times m_Q$, gives $\Delta\tau \sim (10^{-1})$ fm/c, which is smaller than the formation time of the QGP, $\tau_0 \sim 1/\Lambda_{\rm QCD} \sim O(1)$ fm/c [67]. Consequently, heavy quarks undergo the full evolution of the QGP, thus being sensitive to the QGP properties. In addition, $m_Q >> \Lambda_{\rm QCD}$ implies that the m_Q act as a long-distance cut-off, which allows describing the heavy quark production in the framework of perturbative QCD (pQCD) down to low $p_{\rm T}$ [68]. Therefore, heavy flavour observables, i.e. heavy-flavour hadrons containing charm or beauty quark, and quarkonium, the bound state of a heavy quark pair ($c\bar{c}$ or $b\bar{b}$), are penetrating observables to study the QGP created in heavy-ion collisions.

Measuring the same observables in small systems collisions is crucial to provide a baseline for heavy-flavour studies in heavy-ion collisions. For example, one of the intuitive observables is the nuclear modification factor $R_{\rm AA}$ defined as the ratio of the production in nucleus-nucleus collisions to that in pp collisions at the same energy scaled by the number of binary collisions, which quantifies the modification of the particle production in heavy-ion collisions with respect to the one in proton-proton (pp) collisions. Besides, the measurements of heavy-flavour production in pp collisions provide a testing ground for our knowledge of QCD.

In nucleus-nucleus collisions, along with the genuine effects from the QGP medium, cold nuclear matter (CNM) effects, induced by the presence of heavy nuclei in the initial state, affect heavy-flavour and quarkonium production. The CNM effects can be divided into twofold, an initial state effect acting on heavy quark production and a final-state effect on the produced heavy-flavour hadrons and quarkonium. The kinematic distributions of heavy quark pair can be modified by the multiple scattering of incoming partons, which leads to parton energy loss [69] or gluon radiation [70]. For quarkonium, one of the well known final state CNM effects is nuclear absorption, the break-up of the bound state while passing through the nucleus [71]. Quarkonium can also be dissociated by interactions with other hadrons (co-movers) produced in the collision without the presence of the QGP fireball [72]. Under the assumption that the QGP is not formed in p–A collisions, the measurements provide a clean environment to study cold nuclear matter effects, which is essential to interpret the results in nucleus-nucleus collisions.

As shown in Figure 2.1, the highest collision energies at the LHC provide a significantly larger cross

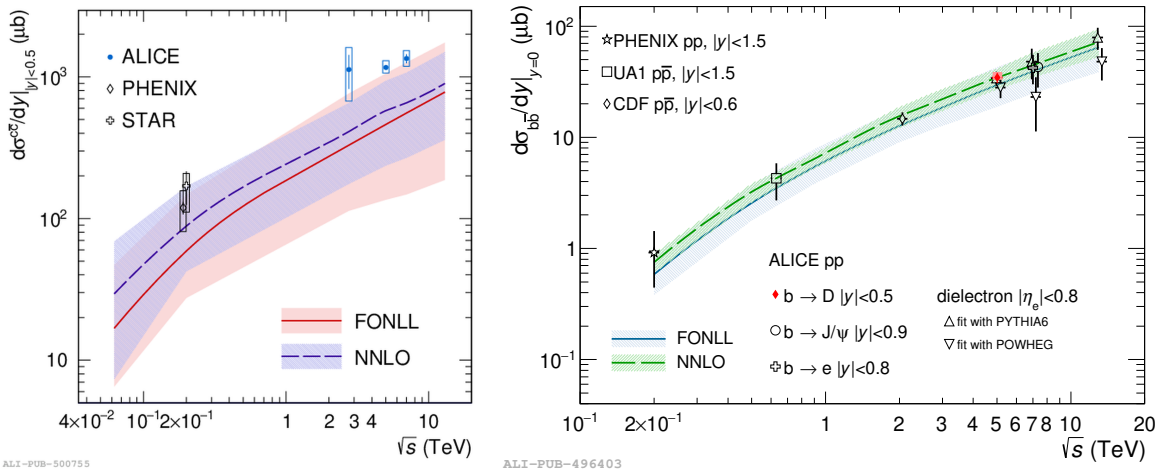

Figure 2.1: Charm (left) and beauty (right) production cross section at midrapidity per unit of rapidity as a function of the collision energy. Figure taken from [73] and [74] for charm and beauty, respectively. The PHENIX and STAR results on the left panel and ALICE data points on the right panel are shifted in horizontal axis for better visibility.

section of the heavy-flavour production cross sections compared to previous experiments, enabling more precise and more differential measurements in the heavy-flavour sector. The J/ψ meson, a key observable in this thesis work, is a bound state of $c\overline{c}$ pair. The measured J/ψ mesons are composed of three components, those directly produced from $c\overline{c}$ pair, those from (strong or electromagnetic) decays of excited charmonium states and those from a weak decay of beauty hadrons. The first two components are called prompt J/ψ, originating from charm quark production, and the last component is called non-prompt J/ψ, inherited from beauty quark production. The feed down contribution of J/ψ from excited charmonium states depends on the momentum of the J/ψ meson, summarized in Table 2.1. Therefore, the measurement of J/ψ meson production with the ability to disentangle the prompt and the non-prompt contribution allows one to study charm and beauty quark production simultaneously. In this chapter, the experimental and theoretical study of open heavy-flavour and quarkonium production will be discussed, focusing on the recent progress in the LHC era. First, the current understanding of the open heavy-flavour and quarkonium production mechanism will be reviewed with measurements in pp collisions. Then, the measurements in Pb-Pb collisions will be briefly discussed, showing the properties of the QGP learnt from the measurements of the open heavy-flavour and quarkonium production. Finally, the recent measurements and theoretical developments of open heavy-flavour and quarkonium production in p–Pb collisions will be discussed, which are crucial inputs for interpreting the results of this thesis work later in Chapter 6.

	direct	from χ_{c1}	from χ_{c2}	from $\psi(2S)$
"low" p_{T} J/ψ	79.5 ± 4 %	8 ± 2 %	6 ± 1.5 %	6.5 ± 1.5 %
"high" p_{T} J/ψ	64.5 ± 5 %	23 ± 5 %	5 ± 2 %	7.5 ± 0.5 %

Table 2.1: J/ψ feed down fraction in hadroproduction at Tevatron and LHC energies. Table taken from [75]

2.1 Heavy-flavour and quarkonium production in pp collisions

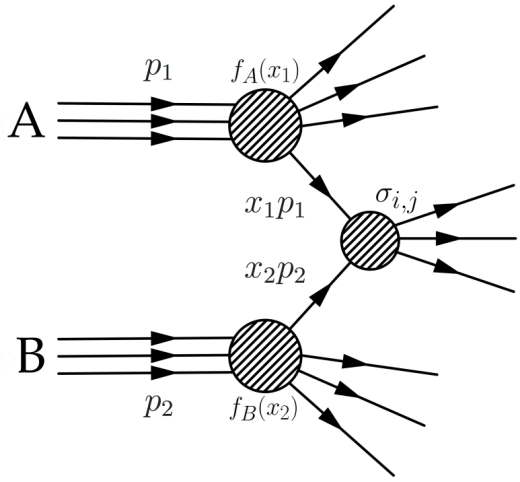

Figure 2.2: Schematic drawing of a hard parton-parton scattering process in a collision of hadron A and hadron B.

In the framework of pQCD, the basic production process of heavy-flavour hadrons in hadronic collisions is described by the factorization theorem [76], as a product of the production of a heavy quark and the formation of color neutral hadrons. As illustrated in Figure 2.2, under the factorization theorem, the production cross section of a heavy quark Q with the transverse momentum of p_{T} and at the rapidity y, at the center of mass energy s can be written as

$$\sigma^{Q+X}[s, p_{\mathrm{T}}, y, m_Q] \simeq \sum_{i,j} \int_0^1 \mathrm{d}x_i \int_0^1 \mathrm{d}x_j \, f_i^{\mathrm{A}}(x_i, \mu_F) \, f_j^{\mathrm{B}}(x_j, \mu_F) \, \hat{\sigma}_{ij\to Q\overline{Q}}[x_i, x_j, s, p_{\mathrm{T}}, y, m_Q, \mu_F, \mu_R], \tag{2.1}$$

where f_i^{A} (f_i^{B}) is the parton distribution function of the colliding hadron A (B), i (j) denotes all possible partons in the colliding hadrons carrying a fractional momentum x_i (x_j) and $\hat{\sigma}_{ij\to Q\overline{Q}}$ is the partonic scattering cross section, which can be calculated in pQCD, μ_F is the factorization scale which is generally proportional to m_Q and μ_R is the renormalization scale at which the strong coupling constant α_s is evaluated. The factorization scale μ_F is introduced in order to separate the short and long distance effects, so that the short distance interaction of the partonic scattering cross section and the long distance effect arising from the parton distribution functions can be independently justified. The remaining term, the formation of color neutral hadrons is non-perturbative process and is distinct for open heavy-flavour hadrons and quarkonium states. While heavy quark and its antiquark independently fragment to form open heavy-flavour hadrons, quarkonium states are produced from the evolution of $Q\overline{Q}$ to bound state. In this section, the heavy quark production as well as the formation of open heavy-flavour hadrons and quarkonium states will be discussed.

2.1.1 Heavy quark production in hadronic collisions

In perturbative theory, there are two leading order (LO) processes for heavy quark production in hadronic collisions, which are shown in Figure 2.3. For these 2→2 processes, the momentum fraction of x_1 and

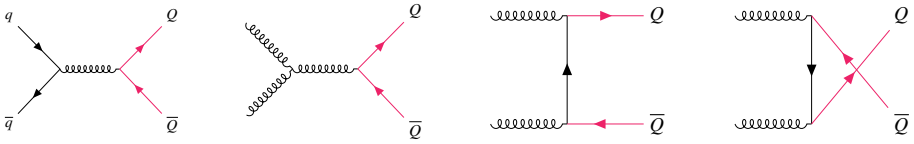

Figure 2.3: Feynman diagram at leading-order (LO) of initial hard scattering for heavy quark production. The left diagram shows the scattering of quark and antiquark. Feynman diagrams represent s-channel, t-channel and u-channel flavour production of gluons from the second left.

x_2 can be written as the function of the transverse mass ($m_{\mathrm{T}} = \sqrt{m_Q^2 + p_{\mathrm{T}}^2}$) and the rapidity ($y$) of the produced heavy quarks. In the centre-of-mass (CM) frame of the incoming hadrons,

$$\begin{aligned} x_1 &= \frac{m_{\mathrm{T}}}{\sqrt{s}}(e^{y_Q} + e^{y_{\overline{Q}}}), \\ x_2 &= \frac{m_{\mathrm{T}}}{\sqrt{s}}(e^{-y_Q} + e^{-y_{\overline{Q}}}). \end{aligned} \tag{2.2}$$

In terms of the m_{T} and the rapidity difference between a heavy quark and antiquark (Δy), the Mandelstam variables for heavy quarks in 2→2 processes can be conventionally written as

$$\begin{aligned} \tilde{s} &= (p_1 + p_2)^2 = 2p_1 \cdot p_2 = 2{m_{\mathrm{T}}}^2(1 + \cosh \Delta y), \\ \tilde{t} &= (p_1 - p_3)^2 - m_Q^2 = -2p_1 \cdot p_3 = -2{m_{\mathrm{T}}}^2(1 + e^{-\Delta y}), \\ \tilde{u} &= (p_2 - p_3)^2 - m_Q^2 = -2p_2 \cdot p_3 = -2{m_{\mathrm{T}}}^2(1 + e^{\Delta y}), \end{aligned} \tag{2.3}$$

that the minimum virtuality exchanged is, at least m_Q^2, for all channels. The strong coupling constant α_s, is set in the scale of the minimum transverse momentum transferred, which is the order of the mass m_Q. Thus, perturbative calculation can be reliably applicable for heavy quark production [77].

The perturbative calculation of heavy quark production, including the corrections for higher order processes, is carried out in different schemes [78]. One example is the Fixed-Flavour-Number scheme (FFNS), where the heavy quark is not an active parton in the proton. In the FFNS scheme, the logarithms of the heavy quark mass $\alpha_s \ln(\mu/m)$ arise in each order of perturbation expansion. Consequently, when the momentum transfer gets larger, the calculation become divergent, so that only a fixed order (FO) calculation is possible. An alternative scheme is the so-called zero-mass variable-flavour-number scheme (ZM-VFNS), in which the heavy quark is treated as massless above a certain threshold so that the resummation of the logarithms is possible. At the same time, the heavy quark is an active parton in the PDFs and final-state Fragmentation Functions (FFs). Below the threshold, the heavy quark is considered as infinitely massive, thus, the production process is prohibited. There are several model calculations which provides the description for the intermediate regime between FFNS and ZM-VFNS by matching procedure and are valid in the entire kinematic range, such as Fixed Order

plus Next-to-Leading Logarithms (FONLL) [79] and General-Mass Variable Flavour Number Scheme (GM-VFNS) [80] in the NLO.

2.1.2 Open heavy-flavour production

In order to describe the measurements from the collisions, the production cross section of heavy quarks is transformed into the production cross section of heavy-flavour hadrons. The effects arising from the hadronization process are expressed in terms of a non-perturbative fragmentation function (FF). In general, the FF describes the probability of each parton fragmenting into a hadron with a momentum fraction z of the parton. Several models are available, combined with heavy quark production mechanisms described above, to provide the theoretical predictions of open heavy-flavour measurements. Since the fragmentation of a heavy quark is assumed to be independent of the production mechanisms of a heavy quark (universality), most of the models used the FFs measured in e^+e^- reactions. Some of Monte Carlo generators provide the fragmentation process, such as PYTHIA [81] and HERWIG [82] which are based on the Lund string model [83, 84], and cluster hadronization model [85], respectively.

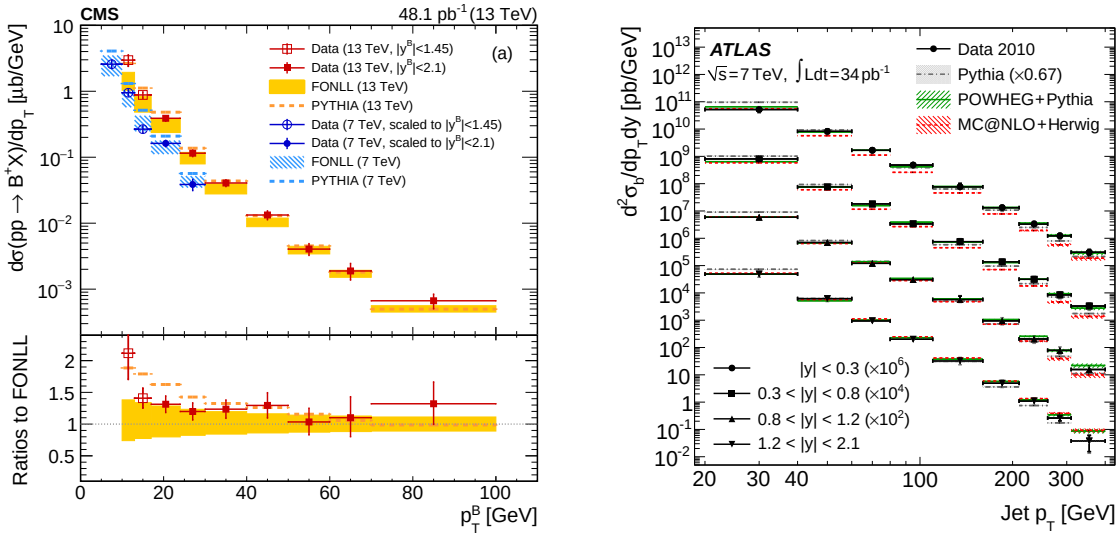

Figure 2.4: (Left) p_{T}-differential cross section of B^+ mesons in pp collisions at $\sqrt{s}$ = 7 (blue circle) and 13 TeV (red square) measured by the CMS collaboration compared with theoretical predictions [86].(Right) p_{T}- and $y-$ double differential cross section of $b-$jets in pp collisions at $\sqrt{s}$ = 7 TeV measured by the ATLAS collaboration shown as circle. Coloured lines with boxes represent different theoretical calculations [87].

Experimentally, open heavy-flavour production has been explored in various ways in hadron colliders through their decay products, relying on the properties of the hadrons, such as invariant mass and lifetime. Depending on the characteristics of the detectors and the abundance of the data sample, different approaches are used to measure open heavy-flavour hadron production. The left panel of Figure 2.4 shows the p_{T} differential cross section of B^+ mesons in pp collisions at $\sqrt{s}$ = 7 and 13 TeV measured by the CMS collaboration [86] via full reconstruction of a decay chain, $B^+ \rightarrow J/\psi(\rightarrow \mu\mu) + K^+$. On the right panel of Figure 2.4, the p_{T} and y differential cross section of $b-$ jets is shown as a function of jet p_{T}, obtained by the flavour tagging for the reconstructed jets [87]. In addition, the heavy-flavour production has been measured via leptons from semileptonic decays relying on the

substantial branching ratio. For example, the p_{T} and y differential cross sections of electrons from open heavy-flavour decays and beauty-hadron decays are shown in the left panel of Figure 2.5 [88, 89]. As additional $q\overline{q}$ pairs can be created in the beauty hadron decays, beauty hadrons have much more decay modes than other hadrons. Therefore, instead of one specific decay channel, inclusive decay daughters, such as non-prompt J/ψ and non-prompt D meson, have been measured, providing the opportunity to access both charm and beauty quark production simultaneously. The right panels of Figure 2.5 show the differential cross section of non-prompt J/ψ as a function of p_{T} (upper) and of y (bottom) in pp collisions at $\sqrt{s}$ = 5 TeV measured by the LHCb collaboration [90]. The measurements at low p_{T} for electrons from beauty-hadron decays and B^+ mesons tend to lie at the upper limit of FONLL uncertainty. Overall, all measurements of beauty-hadron production carried out in various ways in various kinematic ranges are, however, well described with the pQCD model predictions. The situation is similar for charm hadron production [67].

Recently, a significant difference of the charm fragmentation fractions at LHC energies compared to those measured in $\mathrm{e^+e^-}$ and ep collisions was observed by the ALICE collaboration [73]. Similarly, beauty fragmentation fractions measured by the LHCb collaboration [91, 92] show a clear discrepancy with respect to what was observed in $\mathrm{e^+e^-}$ and ep collisions. These observations suggest that the fragmentation functions are not universal across different collision systems and thus, stimulate further theoretical developments.

2.1.3 Quarkonium production

The J/ψ meson was first discovered in 1974 as the first quarkonium state, via its dielectron decays in p–Be collisions at the Brookhaven National Lab (BNL) [94] and dimuon decays in e^+e^- collisions at the Stanford Linear Accelerator Center (SLAC) [95]. The mass ($M_{\mathrm{J}/\psi}$) and width ($\Gamma_{\mathrm{J}/\psi}$) of the J/ψ meson are known as [15]

$$\begin{aligned} M_{\mathrm{J}/\psi} &= 3096.900 \pm 0.006 \text{ MeV}, \\ \Gamma_{\mathrm{J}/\psi} &= 92.6 \pm 1.7 \text{ keV}. \end{aligned} \tag{2.4}$$

The J/ψ meson has quantum numbers of $J^{PC} = 1^{--}$, where the the parity (P) and charge conjugation (C) are related to the orbital angular momentum (L) and spin (S) as follows, $P = (-1)^{L+1}$ and $C = (-1)^{L+S}$ [15]. Remarkably, the J/ψ meson was discovered via dilepton measurements, involving the electromagnetic decays. Since the $M_{\mathrm{J}/\psi}$ is smaller than open charm threshold (e.g. $2M_{D^\pm} \approx 3738$ MeV [15]), the decay of J/ψ into open charm hadron is hindered. Considering the colour-charge conservation and the charge parity, the lowest allowed hadronic decays require three gluons. However, this decay is suppressed by the OZI rule, which states that the processes in which the initial quark pair does not appear in the final state particles are suppressed [96, 97, 98]. As a result, the electromagnetic decay rate of the J/ψ meson is considerable, a similar order of magnitude as its strong decay rate. The branching ratio of J/ψ into dielectron, as known today, is 5.971 ± 0.032% [15]. Over decades, many other quarkonium states have been discovered, including the exotic states, which are unpredicted in the

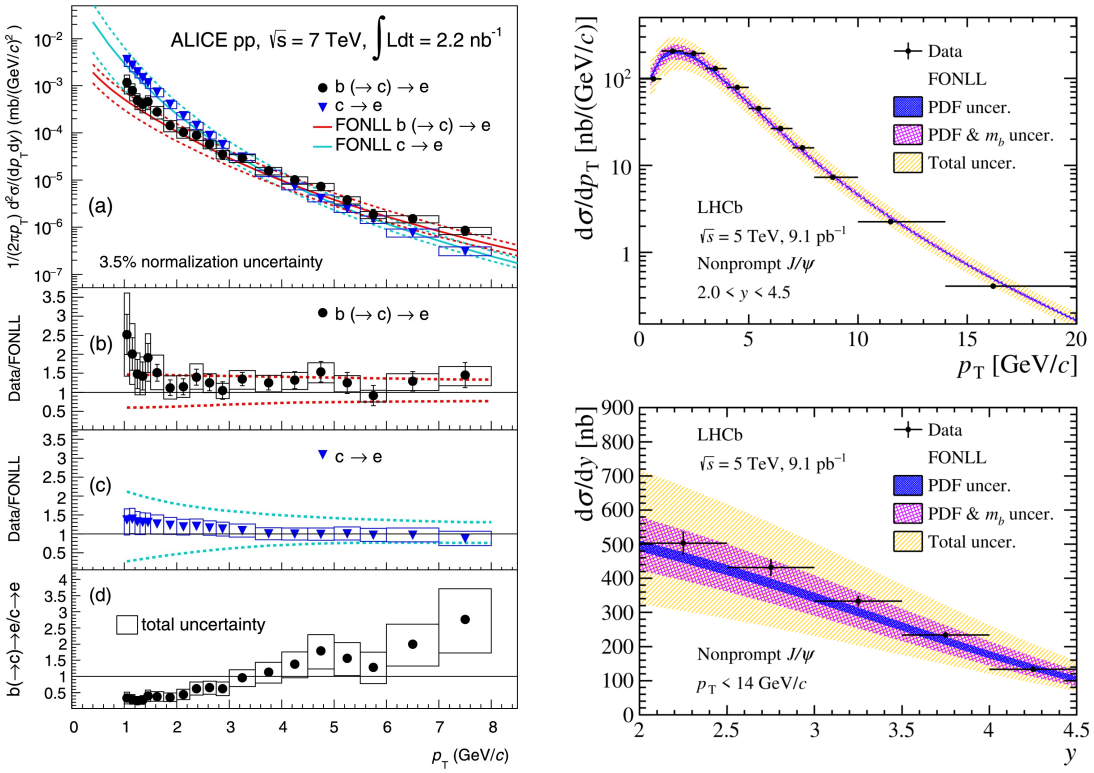

Figure 2.5: (Left) p_{T}-differential invariant cross sections of electrons from beauty and from charm hadron decays in pp collisions at $\sqrt{s}$ = 7 TeV measured by the ALICE collaboration [88, 89]. The solid lines indicate the corresponding FONLL predictions. Ratios of the data and the FONLL calculations are shown in (b) and (c) for electrons from beauty and charm hadron decays, respectively. (Right) The differential cross section of on-prompt J/ψ as a function of p_{T} (upper) and of y (bottom) in pp collisions at $\sqrt{s}$ = 5 TeV measured by the LHCb collaboration compared with FONLL predictions [90].

conventional quark model, as shown in Figure 2.6 for the charmonium family. In analogy to positronium in quantum electrodynamics, quarkonium, the bound system of the quark and antiquark, has been described by so-called Cornell-type potential [99, 100] as follows,

$$V(r) = -\frac{4}{3}\frac{\alpha_s}{r} + k \cdot r, \tag{2.5}$$

where the r is the distance between the quark and antiquark. While the $1/r$ term effectively works in short distance with coupling constant (α_s) as a Coulomb potential, the linear term with string tension k parametrizes the non-perturbative long-distance behaviour, the confinement.

Similar to the production of open heavy-flavour hadrons, the descriptions of quarkonium production are based on the factorization between the heavy quark pair production and quarkonium formation process (binding). Consequently, the main difference between models is the treatment of the non-perturbative hadronization process, which may also require specific description in heavy quark pair production. The simplest model of quarkonium formation is the colour singlet model (CSM), assuming that the quantum state of intermediate $Q\overline{Q}$, i.e. spin and colour, does not change in the final-state quarkonium [101]. In other words, the quarkonium is only formed if $q\overline{q}$ pair is created in a colour singlet states that has the

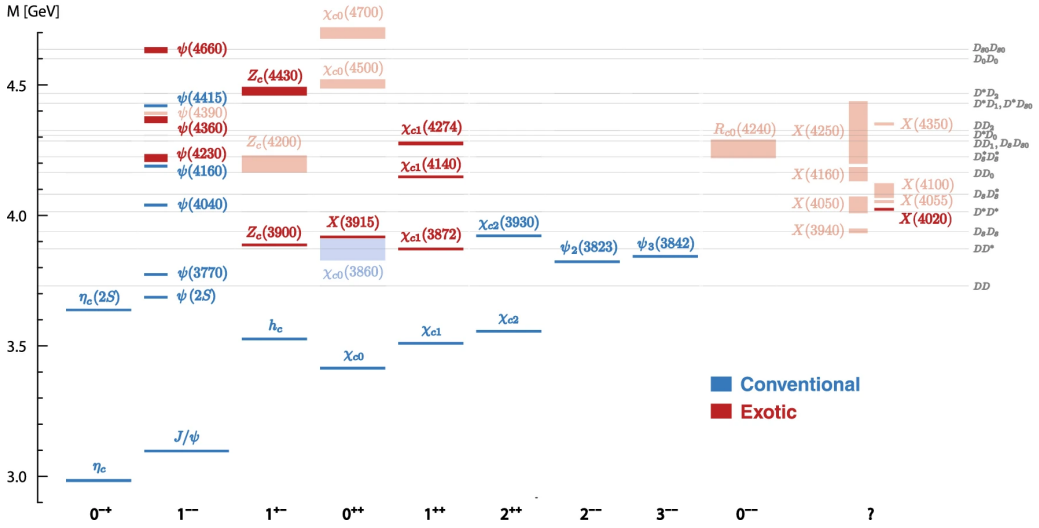

Figure 2.6: Charmonium spectrum as of July 2020 from the PDG [30]. Horizontal axis shows the quantum numbers J^{PC} and vertical axis is for the mass. Not well-established states are shown in pale colors and the box heights are the mass ranges. The open-charm thresholds are shown as horizontal lines with labels on the vertical axis of right side. Figure taken from [93]

same quantum numbers as the final-state. For the zero relative velocity between quark and antiquark (v), the production cross section can be estimated with the Schrödinger wave function of the quarkonium at the origin $R_H(0)$ in the colour-singlet state,

$$\sigma_{\mathrm{CSM}} \propto \sigma^{pp\to Q\overline{Q}}(v=0)\cdot|R_H(0)|^2. \tag{2.6}$$

The colour evaporation model (CEM) is another simple model for the quarkonium formation process, relying on a different assumption. As opposed to the CSM, the probability of forming a specific quarkonium state below the open-charm threshold is independent of the quantum state of the intermediate $Q\overline{Q}$, assuming that colour in $Q\overline{Q}$ is neutralized by the interaction with the collision-induced colour field [102, 103]. Under this assumption, only a part of the total $q\overline{q}$ production cross section is relevant for the quarkonium formation process. Thus, the production cross section of quarkonium can be written as so-called sub-threshold cross section, obtained by integrating the $q\overline{q}$ production cross section over the kinematic region between the invariant mass threshold of heavy-quark pair ($2m_Q$) and that of the lightest open heavy-flavour hadron pair ($2M$),

$$\sigma_{\mathrm{CEM}} = F_H \int_{2m_Q}^{2M} \mathrm{d}m_{Q\overline{Q}} \frac{\mathrm{d}\sigma^{pp\to Q\overline{Q}}}{\mathrm{d}m_{Q\overline{Q}}}. \tag{2.7}$$

A fixed fraction F_H of the sub-threshold cross section is independent of energy and determined empirically, or on the basis of statistical assumptions [104]. An effective field theory for two heavy quarks called nonrelativistic QCD (NRQCD) provides the framework for studying heavy quarkonium production based on first principles [105]. In addition to α_s, the relative velocity (v) works as an additional scale in the theory [106]. The $Q\overline{Q}$ state is described as an expansion over Fock states of determined angular momentum and colour properties, $\overline{Q}(2S+1L[n])$, where n = 1 (colour singlet) or 8 (colour octet). The probability of the $Q\overline{Q}$ state evolving to a quarkonium is described by the long-distance matrix elements (LDME) ($< O_H^n >$), which are not fully calculable and partly extracted from measurements. The production cross section of the quarkonium state is then written as

$$\sigma_{\mathrm{NRQCD}} = \sum_n \sigma^{pp\to Q\overline{Q}}. < O_H^n > . \tag{2.8}$$

The measurements of triplet S-wave states of quarkonium, such as the J/ψ, ψ(2S) and Υ(nS) have been carried out with dilepton decay mode with the branching ratio of $O(1)$ % [15]. The triplet P-waves are usually reconstructed via their radiative decays into a triplet S-wave, i.e. $\chi_c \to \mathrm{J}/\psi + \gamma$ [107]. The

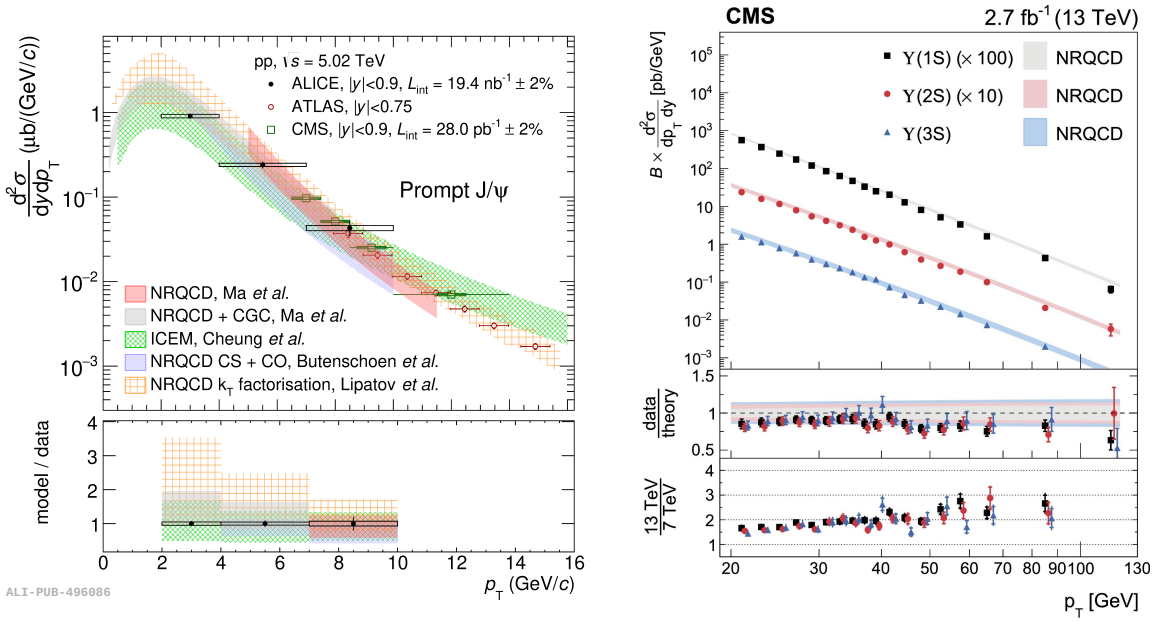

Figure 2.7: (Left) p_{T}-differential cross section of prompt J/ψ meson in pp collisions at $\sqrt{s}$ = 5.02 TeV by ALICE [108], ATLAS [109] and CMS [110] with theoretical predictions. Figure taken from [108].(Right) p_{T}-differential cross section of Υ(1S),Υ(2S) and Υ(3S) in pp collisions at $\sqrt{s}$ = 13 TeV measured by the CMS collaboration with the prediction from NRQCD [111].

left panel of the Figure 2.7 shows the p_{T}-differential cross section of prompt J/ψ meson in pp collisions at $\sqrt{s}$ = 5.02 TeV from the ALICE [108], ATLAS [109] and CMS collaborations [110]. The NRQCD based models [112, 113, 114, 115] and ICEM on the basis of the colour evaporation model [116] provide a good description of the prompt J/ψ cross section in the given kinematic ranges. On the right panel of the Figure 2.7, p_{T}-differential cross section of Υ(1S),Υ(2S) and Υ(3S) in pp collisions at $\sqrt{s}$ = 13 TeV measured by the CMS collaboration is presented [111]. All states are well described by the NRQCD

calculations [117]. As shown for both measurements of prompt J/ψ and Υ(nS), the comparison of data with model calculations is mainly limited by the theoretical uncertainties arising from heavy quark mass, scales, etc. In addition, the measurements of the J/ψ polarization parameters [118, 119] are not described by the NRQCD calculations well, showing there is still room for improvement in the theory.

2.2 Heavy-flavour and quarkonium production in nucleus–nucleus collisions

Charm and beauty quarks are excellent probes of the QGP created in heavy-ion collisions as they have a heavy mass. First, the shorter formation time of the heavy quark production via initial parton-parton scattering (≤ 0.07 fm/c for $c\bar{c}$ and ≤ 0.02 fm/c for $b\bar{b}$) [120] with respect to the QGP formation time, which is about $0.3 \sim 1.5$ fm/c at LHC energies [121, 122] makes heavy quarks witness of full evolution of the QGP. In addition, the mass of heavy quark is much larger than the temperature reached in heavy-ion collisions at LHC energies so that the contribution of thermal production is expected to be negligible [123].

Final-state heavy-flavour hadrons, experiencing the whole evolution of the QGP, will deliver the medium information via the modification of particle yields and phase-space distributions. The aforementioned modification can be quantified with the nuclear modification factor (R_{AA}), which is defined as the ratio between the particle yields in nucleus-nucleus (AA) collisions ($\mathrm{d}^2N_{\mathrm{AA}}/\mathrm{d}p_{\mathrm{T}}\mathrm{d}y$) and the corresponding yields in pp collisions ($\mathrm{d}^2N_{\mathrm{pp}}/\mathrm{d}p_{\mathrm{T}}\mathrm{d}y$) scaled by the average number of nucleon-nucleon collision ($< N_{\mathrm{coll}} >$),

$$R_{\mathrm{AA}} = \frac{1}{< N_{\mathrm{coll}} >} \frac{\mathrm{d}^2N_{\mathrm{AA}}/\mathrm{d}p_{\mathrm{T}}\mathrm{d}y}{\mathrm{d}^2N_{\mathrm{pp}}/\mathrm{d}p_{\mathrm{T}}\mathrm{d}y}. \tag{2.9}$$

While the absence of any medium effects leads to $R_{\mathrm{AA}} = 1$, in-medium energy loss of partons implies a softening of the final-state hadron p_{T} spectrum, resulting in $R_{\mathrm{AA}} < 1$ at large p_{T}. There are several sources of the heavy quark energy loss in the QGP medium. For high energetic quarks, the gluon radiation through the scattering to the medium constituents are expected to be dominant mechanism. The amount of radiative energy loss is not same for all hadrons but depends on colour coupling factor and mass [124]. A distinctive mass hierarchy and colour charge dependence will reflect in R_{AA} measurements as $R^{\pi}_{\mathrm{AA}} < R^{D}_{\mathrm{AA}} < R^{B}_{\mathrm{AA}}$ [120]. Furthermore, partons lose their energy via elastic scatterings with the medium as well providing hint of possible heavy quark collectivity in the medium.

Besides the R_{AA}, the interaction of heavy quark with the QGP medium can be accessed via the measurements of the azimuthal anisotropic flow parameter v_2. The reaction plane of a collision is defined as a plane formed by the beam axis and the impact parameter vector of the colliding nuclei. Then, Fourier expansion of the invariant triple differential distributions with respect to the reaction plane is

$$E\frac{\mathrm{d}^3N}{\mathrm{d}^3\mathbf{p}} = \frac{1}{2\pi p_{\mathrm{T}}}\frac{\mathrm{d}^2N}{\mathrm{d}p_{\mathrm{T}}\mathrm{d}y}\left(1 + 2\sum_{n=1}^{\infty} v_n \cos[n(\varphi - \Psi_{\mathrm{RP}})]\right), \tag{2.10}$$

where E is the energy of the particle, p the momentum, φ the azimuthal angle and Ψ_{RP} the reaction plane angle. The second order Fourier coefficients is defined as the anisotropic flow parameter v_2, which is given by

$$v_2(p_{\mathrm{T}}, y) = \langle \cos[2(\varphi - \Psi_{\mathrm{RP}})] \rangle, \tag{2.11}$$

where the angular brackets denote an average over the particles [125]. In the left panel of Figure 2.8,

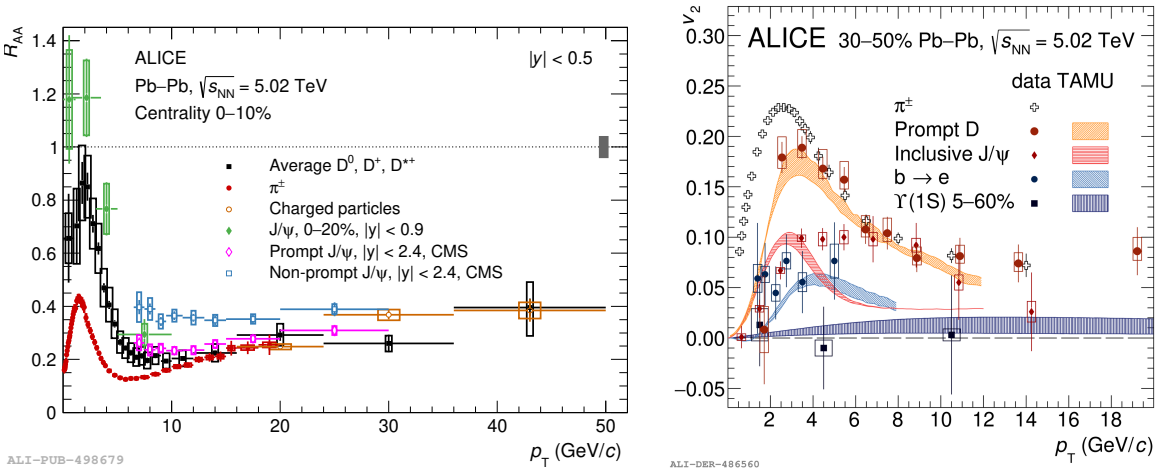

Figure 2.8: (Left) Nuclear modification factor of prompt D mesons (average D^0, D^+, D^{*+}) [126], charged particles [127], charged pions [128] and inclusive J/ψ from ALICE [129], and of prompt and non-prompt J/ψ measured by CMS in Pb–Pb collisions at $\sqrt{s_{\mathrm{NN}}}$ = 5.02 TeV [130]. Figure taken from [126]. (Right) ALICE measured anisotropic flow parameter v_2 of charged pions [131], prompt D mesons [132], inclusive J/ψ [133], electrons from beauty-hadron decays [134] and Υ(1S) [135] as a function of p_{T} in Pb–Pb collisions at $\sqrt{s_{\mathrm{NN}}}$ = 5.02 TeV compared with model predictions [136].

the strong suppression of prompt D meson and non-prompt J/ψ was observed which was not seen in the p-Pb collisions, indicating in-medium energy loss of charm and beauty quark in Pb–Pb collisions. In addition, an ordering of R_{AA} is observed below $p_{\mathrm{T}} \lesssim 10$ GeV/c for charged pions, prompt D meson and non-prompt J/ψ originating from beauty-hadron decays, supporting the quark mass dependence energy loss. It is noteworthy that the interpretation of the different suppression patterns for each hadrons is not straightforward, as several effects, such as a degree of thermalization, different fragmentation function can also play a role, in addition to the in medium-energy loss mechanisms discussed above. In the right panel of Figure 2.8, measurements of v_2 for various hadrons are shown as a function of p_{T}. Measured v_2 of charged pions, prompt D meson and inclusive J/ψ exhibit an universal trend in p_{T} with different amplitude, suggesting charm quark thermalization in the QGP medium. Furthermore, a smaller but non-zero v_2 of electrons from beauty-hadron decays was measured, consistent with less thermalization of beauty quark and charm quark expected by their masses. The Υ(1S) meson, however, shows no indication of non-zero v_2. Therefore, the thermalization of beauty quark is not conclusive yet, and further measurements with improved precision in beauty sector are required. In Figure 2.8, it is also visible that the trend of the J/ψ R_{AA} is different from other results, showing an enhancement at low p_{T}. This can be further understood by looking at the J/ψ R_{AA} as a function of charged particle multiplicity, which is proportional to energy density as shown in the left panel of Figure 2.9. A significantly larger

J/ψ R_{AA} is measured in Pb–Pb collisions at $\sqrt{s_{NN}}$ = 5.02 TeV by the ALICE collaboration at LHC with respect to the J/ψ R_{AA} measured in Au–Au collisions at $\sqrt{s_{NN}}$ = 200 GeV by the PHENIX collaboration at RHIC, as a result of charmonium (re-)generation due to the copiously produced charm quarks at LHC energies as shown in Figure 2.1. The regeneration is expected to happen either at hadronization [137] or throughout the evolution of the QGP [138], which is consistent with the significant non-zero v_2 of J/ψ. Meanwhile, the measured Υ (nS) R_{AA} presented in the right panel of Figure 2.9 shows a clear mass ordering of the suppression. The ordering is expected in the sequential melting scenario [139, 140] based on colour screening [141]. The theory describes the suppression of quarkonium as a melting in thermal medium and thus, the differences in the quarkonium binding energies lead to a sequential melting with increasing temperature. Interestingly, the sequential suppression of Υ (nS) was also observed in p–Pb collisions with much smaller magnitude [142], requiring further theoretical developments than the simple idea of colour screening in Pb–Pb collisions.

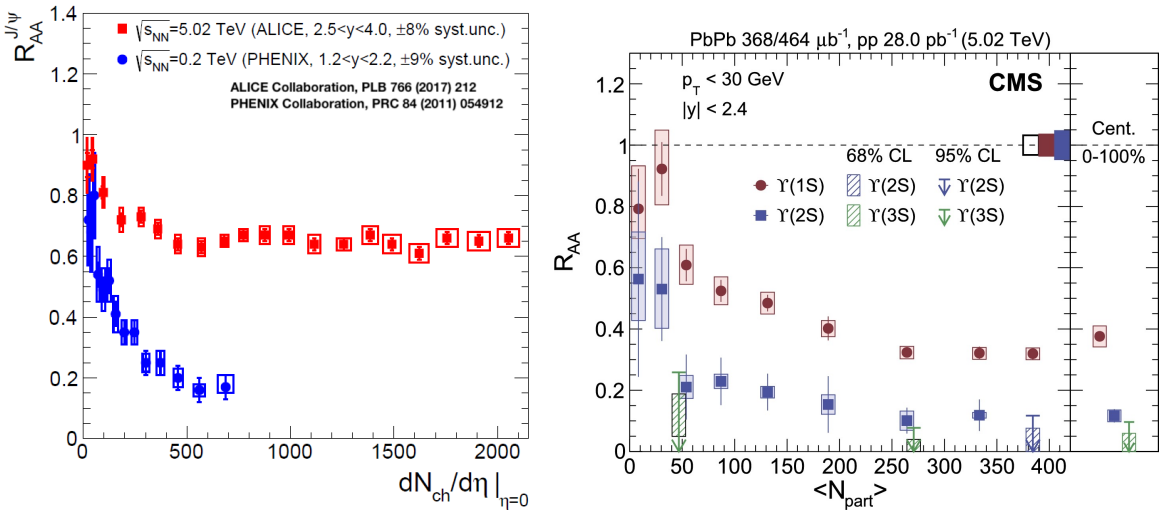

Figure 2.9: (Left) Nuclear modification factor of inclusive J/ψ at forward rapidity as a fucntion of charged particle multiplicity at midrapidity measured in Pb-Pb collisions at $\sqrt{s_{NN}}$ = 5.02 TeV by ALICE [143] and in Au–Au collisions at $\sqrt{s_{NN}}$ = 0.2 TeV by PHENIX [144]. (Right) Nuclear modification factor of Υ(nS) at midrapidity versus average number of participants in Pb-Pb collisions at $\sqrt{s_{NN}}$ = 5.02 TeV measured by the CMS collaboration [145].

2.3 Heavy-flavour and quarkonium production proton-nucleus collisions

2.3.1 Initial state effects from Cold Nuclear Matter (CNM)

The presence of heavy nuclei in the initial states modifies the parton densities, and thus, affects the production of heavy quark. The basic approach for quantifying the modification of heavy-flavour production is replacing the parton distribution functions $f_i^A(x_i, \mu_F), f_j^B(x_j, \mu_F)$ in Equation 2.1 to set of nuclear PDF (nPDF). The set of nPDF has been extracted by the parameterization of various experimental measurements in $Q^2 - x$ plane. There are several sets of nPDF available. The main difference between them is the different set of measurements included in the parameterization and error handling

approaches. In the left panel of Figure 2.10, the R_{pPb} of B^{+} meson and non-prompt J/ψ in p–Pb collisions at $\sqrt{s_{\mathrm{NN}}}$ =8.16 TeV measured by the LHCb collaboration is presented as a function of y together with the NRQCD based model [146, 147, 148] using different sets of nPDF, namely EPPS16 [58] and nCTEQ15 [59]. While the measurements are consistent with unity at backward rapidity, a significant suppression is observed at forward rapidity. The models using different nPDF sets provide good description of the modification trend shown in measurements.

The initial collision environment in p–Pb collisions can be also described in the colour Glass Condensate (CGG) framework [149]. When the Bjorken-x decreases, the gluon density is expected to increase until the maximal occupation is reached. Then, the system eventually saturates due to the large number of self interacting gluons. The saturation effects are characterized as the saturation scale $Q^{2}_{s,A}$ where $\sqrt{s}$ is the collision energy and A is the nucleon number. The model provides predictions for open heavy-flavour quarkonium production at forward rapidity at LHC energies in which the production suppression gets larger towards forward regions, reflecting stronger saturation effects at smaller Bjorken-x values.

The so-called Cronin-effect is also one of the well-known phenomena in proton-nucleus collision [150]. The Cronin effect refers an enhancement of hadron production in proton-nucleus collisions with respect to pp collisions at a transverse momentum of a few GeV/c. It is interpreted as the result of multiple scattering of the partons in the nucleus prior to the hard scattering. Energy loss of individual partons undergoing soft collisions or radiating gluons in the initial state incoherent from other partons, results in transverse momentum broadening of parton distribution, causing Cronin-enhancement. The opposite scenario is possible such that a nucleus has a single collective parton distribution. In this picture, the interaction of partons become coherent, leading the attenuation of the production [70].

In the right panel of Figure 2.10, the R_{pPb} of electrons from beauty-hadron decays in p–Pb collisions at $\sqrt{s_{\mathrm{NN}}}$ =5.02 TeV measured by the ALICE collaboration is presented as a function of p_{T}. In the measured kinematics range, the R_{pPb} is consistent with unity. The based heavy-flavour production mechanism including nPDF, coherent scattering and incoherent multiple scattering, give reasonable description for the measurements, indicating small cold nuclear matter effect for beauty- hadron production in this kinematic range.

2.3.2 Final state effects in small system?

The huge abundance of heavy quarks at LHC energies allows one to access to new observables, such as the production of excited quarkonium states and v_2 of open and hidden heavy-flavour production. The left panel of Figure 2.11 presents the y-dependence of the R_{pPb} of ψ(2S) and J/ψ in p–Pb collisions at $\sqrt{s_{\mathrm{NN}}}$ =8.16 TeV measured by the ALICE collaboration [153]. At backward rapidity, the ψ(2S) shows larger suppression with respect to J/ψ. A similar trend was also found in the bottomonium sector [142, 154]. Since the initial-state effects for the heavy quark pair are expected to affect similarly all different final quarkonium states, the ordering of the suppression suggests a possible presence of final state effects in p–Pb collisions. In the figure, the measurements are well described by the comover interaction model, assuming a break-up of the quarkonium resonances by collisions with particles with similar

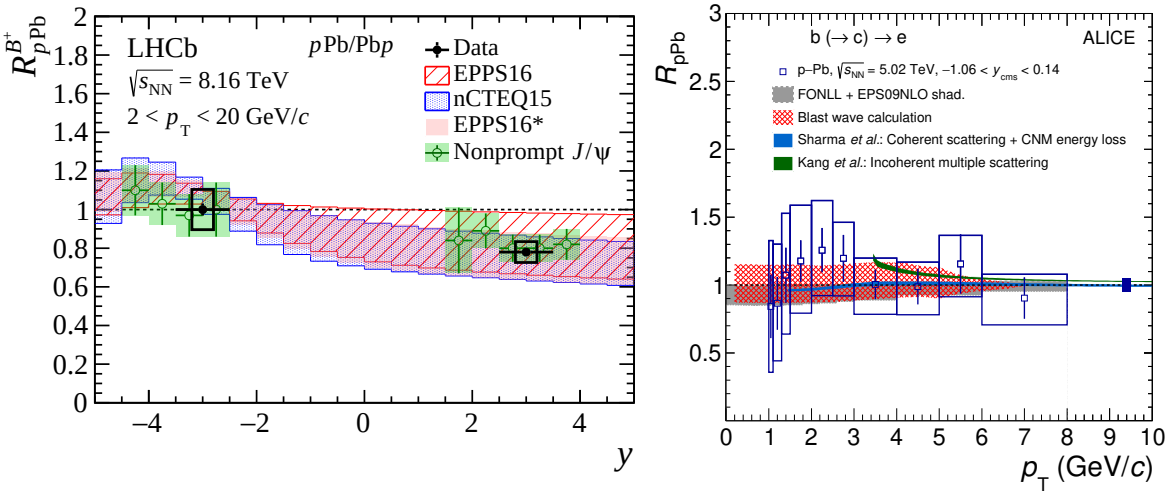

Figure 2.10: (Left) The y-dependence of R_{pPb} of the B^+ meson (filled circle) and non-prompt J/ψ (open circle) in p–Pb collisions at $\sqrt{s_{\mathrm{NN}}}$ =8.16 TeV measured by the LHCb collaboration compared with different nPDF [151] (Right) R_{pPb} of electrons from beauty-hadron decays as a function of p_{T} in p–Pb collisions at $\sqrt{s_{\mathrm{NN}}}$ =5.02 TeV measured by the ALICE collaboration [152]

rapidities from the underlying event [155, 156]. It is noteworthy that the QGP formation is not necessarily required explaining this final state effect.

As in Pb–Pb collisions, possible collectivity in p–Pb collisions was investigated via measurements of v_2. The non-zero v_2 for various hadrons in p–Pb collisions measured in the last years raises the question of whether a fluid-like QGP is also created in small systems or not [157]. In the right panel of Figure 2.11, v_2 of various hadrons measured in high multiplicity p–Pb collisions by the CMS collaboration is presented as a function of p_{T}. As well as for light hadrons, positive v_2 for heavy-flavour hadrons, prompt and non-prompt D^0 mesons and prompt J/ψ. In addition, the hint of mass ordering in the magnitude of v_2 seems consistent with the scenario of being generated via final-state re-scatterings, where heavier quarks tend to develop a weaker collective signal. Nevertheless, as shown in the same figure, the theoretical calculation based on CGC framework, assuming the quark and gluon interaction with the nucleus in a high gluon density environment and irrelevant of further QGP formation, provide a good description for the measurements. In summary, it is still an open and interesting question, whether the QGP-droplet is formed in small systems and further heavy-flavour measurements in p–Pb collisions would shed more light on this puzzle.

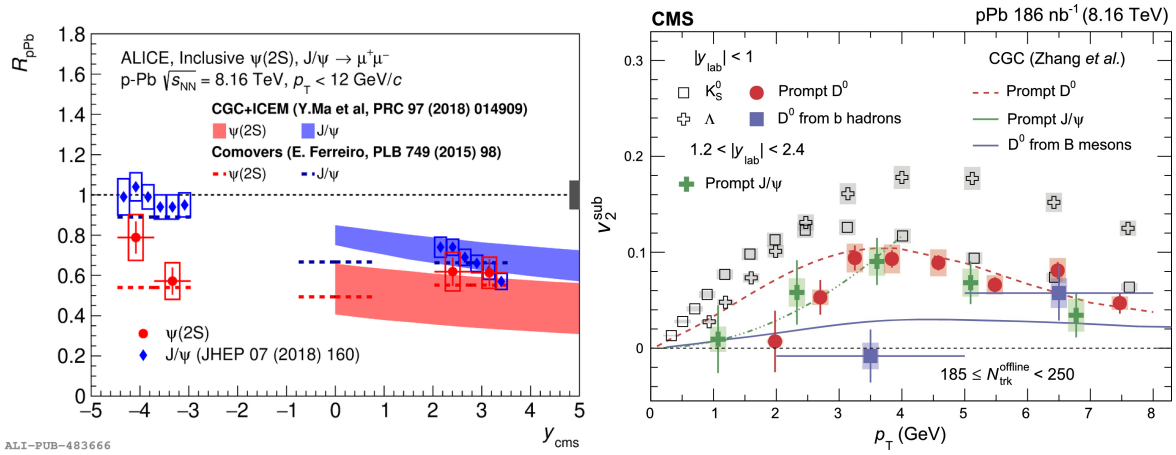

Figure 2.11: (Left) The y-dependence of R_{pPb} of ψ(2S) and J/ψ in p–Pb collisions at $\sqrt{s_{\mathrm{NN}}}$ =8.16 TeV compared with models including final-state effects [153]. (Right) v_2^{sub} for prompt and non-prompt D^0 mesons and prompt J/ψ as functions of p_{T} in high multiplicity p–Pb collisions at $\sqrt{s_{\mathrm{NN}}}$ = 8.16 TeV [158] with theoretical predictions including the CGC approach [159, 160].

3 ALICE at the LHC

3.1 The Large Hadron Collider (LHC)

The Large Hadron Collider (LHC) [161] is a particle accelerator and collider located at CERN, European Organization for Nuclear Research. The LHC consists of 27 km double ring with counter-rotating beams guided by superconducting magnets at a mean underground depth of about 100 m and a number of accelerating structures.

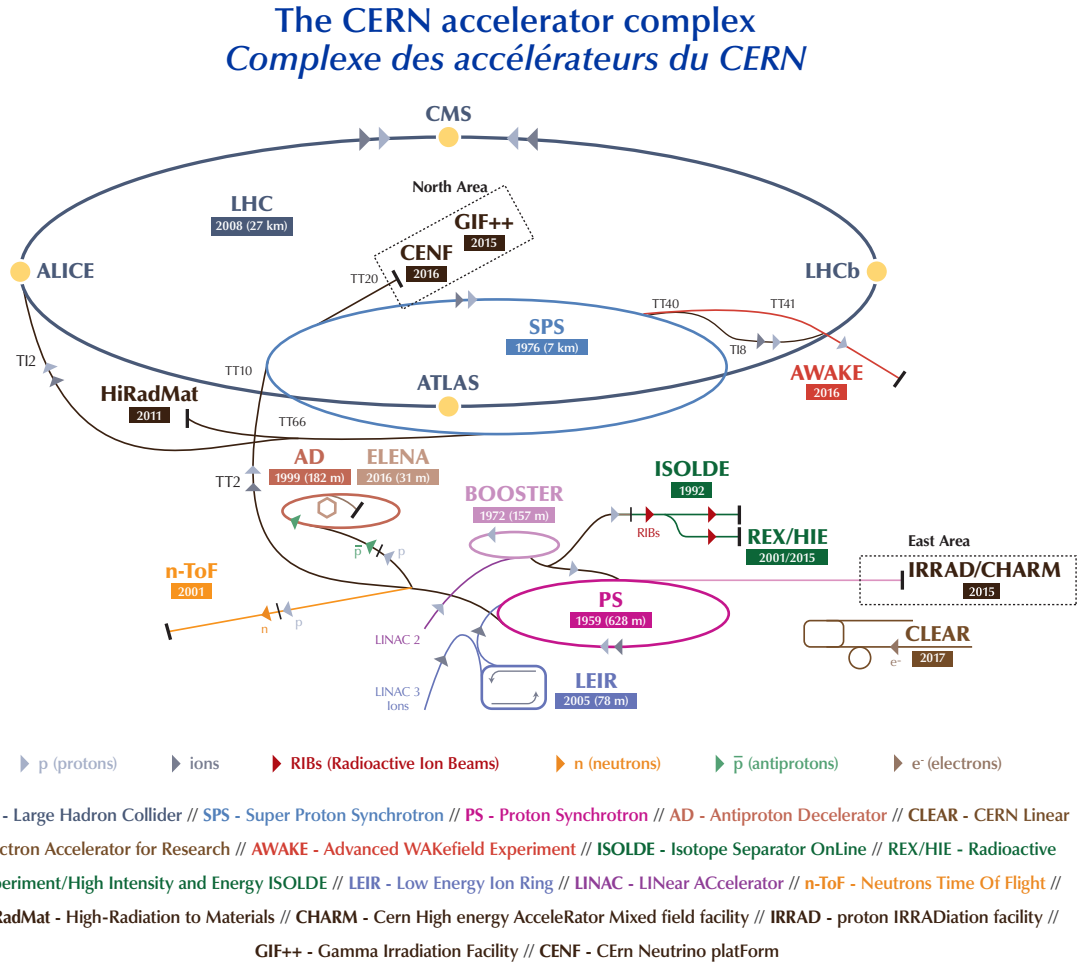

Figure 3.1: The CERN accelerator complex. Protons start from LINAC2 passing through the Booster and reaching the PS while ions start from LINAC3 through LEIR. Both protons and ions are accelerated sequentially through PS, SPS and LHC and are eventually delivered to the four big experiments located at the LHC ring. Figure taken from [162].

The beam is prepared for collisions in several steps as illustrated in Figure 3.1, called the CERN accelerating chain. Linear accelerator 2 (LINAC2) [163] was the starting point for the protons used in experiments at CERN for 40 years and was replaced by Linear accelerator 4 (LINAC4) [164] in 2020. In LINAC2, protons, obtained from hydrogen atom by stripping off its electrons using electric field, had reached the energy of 50 MeV at the end and were then injected into the Proton Synchrotron Booster [165]. Unlike in its predecessor, in LINAC4, negative hydrogen ions consisting of hydrogen atoms with an additional electron are accelerated to 160 MeV and the ions are stripped of their two electrons during injection from LINAC4 into the Proton Synchrotron Booster to leave only protons. The Proton Synchrotron Booster accelerates protons from LINAC2 and LINAC4 to 1.4 GeV and to 2 GeV, respectively, and transfers the beam to the Proton Synchrotron (PS) [166]. For heavy ions like lead (Pb), on the other hand, the accelerating chain starts from the Linear accelerator 3 (LINAC3). Lead ions (Pb^{+29}) are obtained by solid lead evaporation and ionized in an Electron Cyclotron Resonance Ion Source (ECRIS) called GTS-LHC [167]. They are accelerated up to 4.2 MeV/nucleon and further stripped from their electrons to Pb^{+54} in LINAC3. Long pulses from LINAC3 are transformed into high-density bunches and accelerated up to 72 MeV/nucleon in LEIR [168] and transferred to the PS. At the PS, the protons and lead ions are accelerated to 25 GeV and 5.9 GeV/nucleon, respectively, in the desired bunch spacing and delivered to the Super Proton Synchrotron (SPS) [169]. Additional stripper foils between the PS and SPS strip the ions their remaining electrons, leaving a lead ion beam only consisting of nuclei, Pb^{+82}. The SPS accelerates the protons up to 450 GeV and the lead ions up to 177 GeV/nucleon. Beams from the SPS are injected into the LHC via TI2 close to ALICE and TI8 close to LHCb as shown in Figure 3.1 in both clockwise and anticlockwise direction and are then further accelerated to the desired collision energies. Beams inside the LHC are made to collide at four locations, corresponding to the positions of the four particle detectors, ALICE [170], ATLAS [171], CMS [172] and LHCb [173].

Since September 2008 when the LHC started up, various collisions (pp, p−Pb, Pb−Pb and Xe−Xe), at multiple energies, have been provided to the particle detectors [174] through the first physics beam campaign between 2009 and 2013 and the second physics beam campaign between 2015 and 2018, called Run 1 and Run 2, respectively. After the Run 2 campaign, the LHC as well as the experiments including ALICE were in shutdown for upgrading the facilities and maintenance. If there is no special comment, the further description of the LHC and detectors in this chapter will be based on the Run 2 operation configuration as the data used in the analysis in this thesis was taken during Run 2.

3.2 A Large Ion Collider Experiment (ALICE)

ALICE (A Large Ion Collider Experiment) [170] is a detector dedicated to heavy-ion physics, focusing on the physics of strongly interacting matter at extreme energy densities. As a general-purpose detector, the ALICE detector tracks and identifies particles with a very low p_{T} threshold of 0.150 GeV/c in an environment with large charged-particle multiplicities. For example, an average number of charged particles produced per unit rapidity of 2035 ± 52 was measured at midrapidity in Pb−Pb collisions with

small collision impact parameter at centre-of-mass energy of 5.02 TeV per nucleon [175]. As shown in Figure 3.2, the detector is composed of multiple sub-detectors.

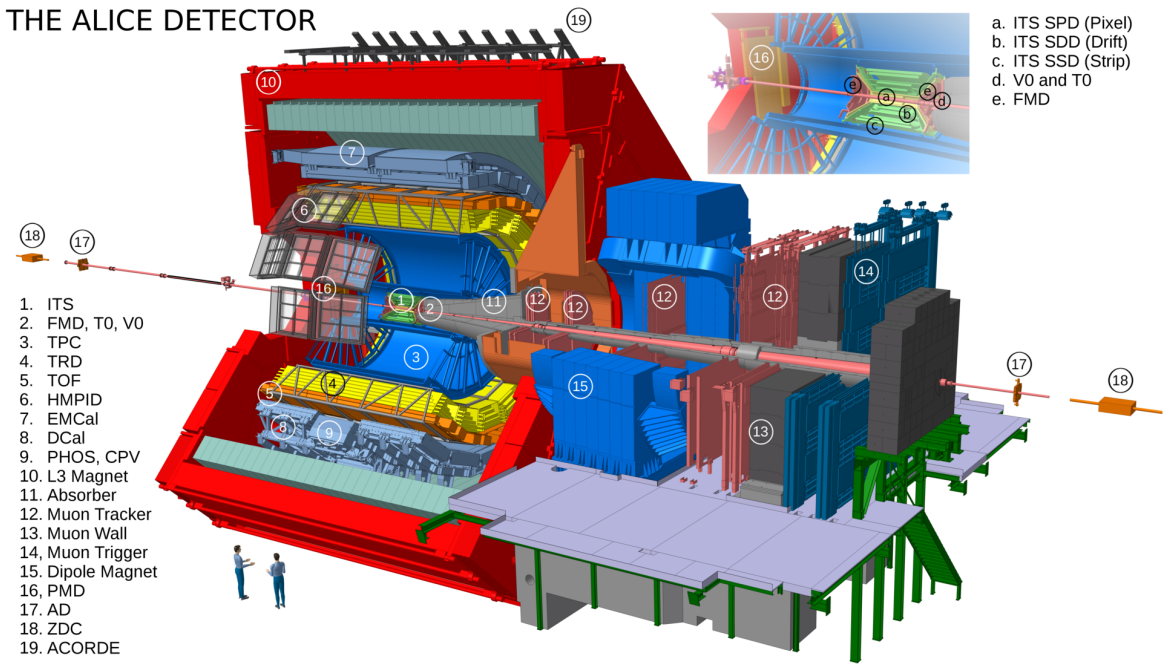

Figure 3.2: Schematic view of the ALICE detector during LHC Run 2 operation. A detailed description is given in the text. Figure taken from [176].

A solenoid magnet previously used in the L3 experiment [177] houses the central barrel detectors covering midrapidity. The magnet provides the magnetic field parallel to the beam axis in nominal magnetic flux density of 0.5 T. Occasionally, the magnet operates in lower magnetic flux density, 0.2 T. From the interaction point to large radii, the Inner Tracking System (ITS), the Time Projection Chamber (TPC), the Transition Radiation Detector (TRD) and the Time-of-Flight (TOF) detector are located, providing full azimuthal angle coverage for tracking and particle identification. In addition, there are several detectors with reduced azimuthal acceptance, dedicated for specific purposes. The High Momentum Particle IDentification detector (HMPID) is a Ring Imaging Cherenkov (RICH) counter offering 3σ separation of pion and kaon up to 3 GeV/c and kaon and proton up to 5 GeV/c [178]. A large Pb-scintillator sampling calorimeter, the ElectroMagnetic CALorimeter (EMCal) and Di-Jet Calorimeter (DCal), provides an opportunity to study jet quenching as well as direct photons and neutral meson production. The photon spectrometer (PHOS) is also an electromagnetic calorimeter, based on scintillating PbWO4 crystals. PHOS is dedicated for measurements of direct photons and neutral mesons with help of a Charged Particle Veto (CPV) detector.

The Muon Arm at forward rapidity ($-4.0 < \eta < -2.4$) provides the acceptance of muons down to low p_{T} around 2GeV/c. It consists of an absorber for suppressing all particles except muons, a dipole magnet with a field integral along the beam axis of 3 Tm, 10 tracking chambers in 5 stations (Muon Tracker), 4 trigger chambers grouped in two stations (Muon Trigger) and an iron wall (Muon Wall) in front of the Muon Trigger for reducing background in the trigger chambers.

At large rapidities, several detectors are installed for characterizing the event and providing the trigger. The Forward Multiplicity Detector (FMD) based on silicon strip detectors and the Photon Multiplicity Detector (PMD) provide event multiplicity. The collision time is measured by the T0 detector, which is an important reference for TPC and TOF measurements. The V0 scintillating detector is used to deliver a minimum bias trigger based on its fast response. The V0 provides centrality determination in addition to the Zero Degree Calorimeter (ZDC), measuring the energy carried by spectator nucleons. The both V0 and the ZDC are used for rejecting beam-gas background. It is not clearly visible in the Figure 3.2, however, the T0, V0 and FMD are installed both sides.

The detectors relevant for the analysis in this thesis are described in detail in the following subsections.

3.3 Measurements in central barrel of the ALICE

3.3.1 Time Projection Chamber (TPC)

A Time Projection Chamber (TPC) is a three-dimensional tracking detector, providing information on many space points of a particle track with the specific energy loss of the particle. TPCs have been developed and widely used in many experiments [179] since it was proposed as a tracking detector for the PEP-4 experiment in 1975 [180]. The TPC was chosen as a main detector in the central barrel of the ALICE for tracking of charged particles and particle identification [181]. The ALICE TPC [182] was designed to cope with the large charged-particle multiplicities, up to 20000 tracks in one interaction in the TPC acceptance and with a high rate readout, about 300 Hz for Pb–Pb collisions and 4 kHz for proton–proton collisions.

The ALICE TPC has a cylindrical shape aligned with the beam pipe and parallel to the magnetic field of solenoid magnet. Its acceptance covers the full azimuthal angle and pseudo-rapidity of $-0.9 < \eta < 0.9$. The active volume is about $90\ \mathrm{m}^3$, with an inner radius of about 85 cm, an outer radius of about 250 cm, and an overall length along the beam direction of 500 cm. The volume is divided into two parts by the central electrode at 100 kV which provides a constant field of 400 V/cm along the beam axis with a voltage dividing network (resistor rods) at the surface of the outer and inner cylinder. During Run 2, the detector was filled with a counting gas consisting of an Ar-CO_2 (88:12) gas mixture [183] which yields an electron drift velocity around 2.7 cm/μs resulting in a drift time of about 96 μs. The maximum event rate is about 1.7 kHz, which is limited by gating grid operation for ion collection [184]. The electrons, produced in the ionization of the gas due to charged particles traversing the detector, drift to the end plates of the cylinder. On the plates, Multi-Wire Proportional Chambers (MWPCs) with cathode pad readout are installed in 18 trapezoidal azimuthal sectors for readout, which have been replaced by Gas Electron Multipliers (GEMs) for the upcoming Run 3 [185]. Considering radial dependence of the track density, the size of the readout-chamber changes in radius, resulting in the Inner Read-Out Chambers (IROCs), divided in 63 pad rows with size of 4 × 7.5 mm^2 ($r\phi \times r$) from 84.8 to 132 cm and the Outer Read-Out Chambers (OROCs) from 134.6 to 246.6 cm, composed with small (6 × 10 mm^2 in 64 rows) and large cathode pads (6 × 15 mm^2 in 32 rows). In total, 557568 readout channels provide the

precise measurement of the arrival point on the transverse plane. The position information along the beam axis is obtained from the measured drift time and the drift velocity which is determined by the gas composition as well as the density which depends on temperature. Thus, a complete three-dimensional trajectory of the charged particle track can be determined with space point resolution in the transverse plane of 300 – 800 μm for high momentum tracks. Using the curvature of the trajectory, the momentum of the particle is calculated with a momentum resolution of 6% at 10 GeV/c, becoming larger to 20% at 100 GeV/c and smaller to 1% at 1 GeV/c.

The amount of energy loss in the TPC active volume is translated into the pulse height of the signal collected at the readout chamber. The measurement of the energy loss per each track is sampled on up to 159 pads, the total number of pad rows in radial direction. Due to the long tail towards high pulse height in the straggling function from the contribution of large energy transfers in a single collision (i.e. δ electrons), the truncated mean ($< \mathrm{d}E/\mathrm{d}x >$), average calculated after excluding the upper 40% of the sampled distribution, is used for the particle identification. The average energy loss per unit path-length can be described by the Bethe-Bloch formula between a travelling particle with momentum $\beta\gamma$ and atoms of the absorber. By correcting the screening of the particle field by polarizable atoms, the so-called "density effect" ($\delta(\beta\gamma)$), and introducing the maximum possible energy transfer in a single collision (W_{max}), the Bethe-Bloch formula reads as follow [186],

$$\left\langle -\frac{\mathrm{d}E}{\mathrm{d}x} \right\rangle = \frac{4\pi N e^4}{mc^2}\frac{1}{\beta^2} z^2 [\ln \frac{\sqrt{2mc^2 W_{\mathrm{max}}}\beta\gamma}{I} - \frac{\beta^2}{2} - \frac{\delta(\beta\gamma)}{2}\ ], \tag{3.1}$$

where mc^2 is the rest energy of the electron, z is the charge number of incident particle, N is the number density of electrons in the matter traversed, e is the elementary charge and I is the mean excitation energy. In practice, Equation 3.1 is often replaced by a simple parametrization of the form with 5 free parameters (P_i):

$$f(\beta\gamma) = \frac{P_1}{\beta^{P_4}}\left(P_2 - \beta^{P_4} - \ln\left(P_3 + \frac{1}{(\beta\gamma)^{P_5}}\right)\right). \tag{3.2}$$

Figure 3.3 shows as an example of the paramerization as a function of particle momentum for different particle species (denoted i, for electrons, pions, kaons, protons,...) together with the measured TPC signal. The deviation of the measured signal of a track ($\mathrm{d}E/\mathrm{d}x$) from the expected signal for a given particle ($< \mathrm{d}E/\mathrm{d}x >_i$) species i in units of the corresponding detector resolution (σ) is defined as a selection variable for particle identification,

$$n_{\sigma_i} = \frac{\mathrm{d}E/\mathrm{d}x - < \mathrm{d}E/\mathrm{d}x >_i}{\sigma}. \tag{3.3}$$

The measurement of the energy loss is influenced by the system-wise effects (e.g. gas composition and pressure, pad size, ...) which is typically about 5% for gaseous detector [188] and a statistical effect, i.e. inversely proportional to the number of samples. With a cosmic-ray data sample, the energy resolution of single tracks was obtained as a function of the number of clusters (N_{cl}), resulting in about 9 % for N_{cl} = 60 and nearly 5 % for N_{cl} = 159 [182]. The usage of the TPC for electron identification for this analysis will be discussed in Chapter 5.

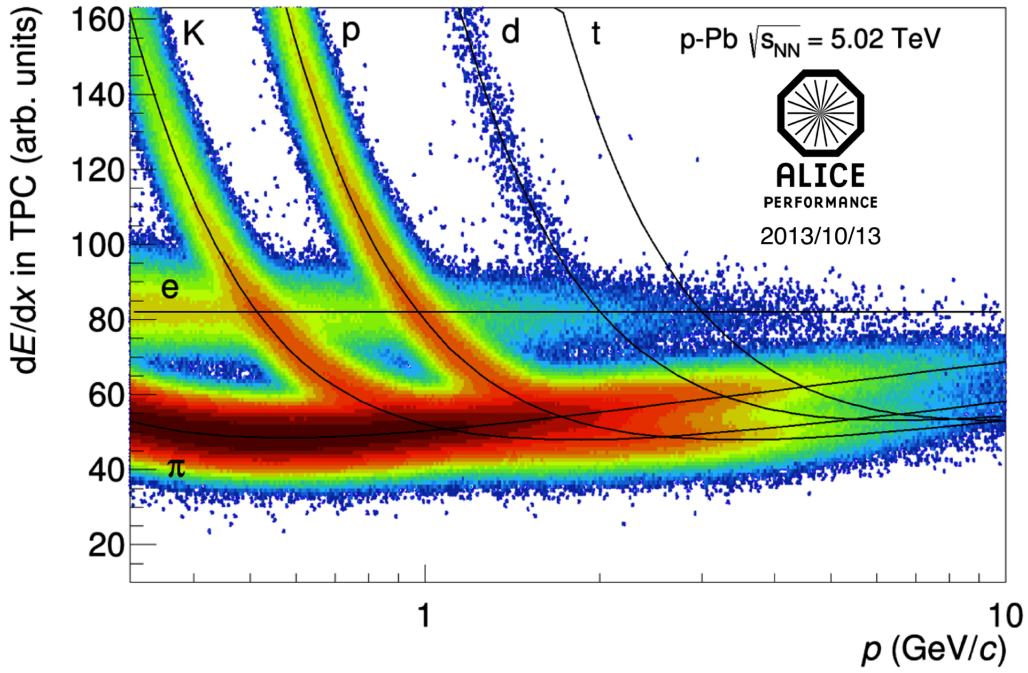

Figure 3.3: Specific energy loss ($\mathrm{d}E/\mathrm{d}x$) in the TPC in p–Pb collisions at $\sqrt{s_{\mathrm{NN}}} = 5.02$ TeV. Solid lines represent the expected signal for each particle species. Figure taken from [187].

3.3.2 Inner Tracking System (ITS)

The Inner Tracking System (ITS) [189] consists of six cylindrical layers of silicon detectors covering the $-0.9 < \eta < 0.9$. The tasks of the ITS are to localize the primary vertex and secondary vertices from decays of hyperons and charm and beauty hadrons, to track and identify particles with momentum below 0.1 GeV/c which are not detected by the TPC, as well as to improve the momentum and spatial resolution of high-momentum particles traversing the TPC. To fulfill its duties, the ITS is located innermost of the ALICE detector surrounding beam pipe, at radii 3.9, 7.6, 15.0, 23.9, 38.0 and 43.0 cm from the interaction point, optimized for efficient tracking with high spatial resolution. As the track density decreases from small radii to large radii, three different technologies were adopted for the silicon sensors. The two innermost layers consist of Silicon Pixel Detectors (SPD). Silicon Drift Detectors (SDD) are used for the two intermediate layers. The two outer layers of the ITS are made of Silicon Strip Detectors (SSD). In addition, due to the high-particle density expected in the collisions, the radiation hardness and material budget were considered for the design of the ITS.

The basic element of the SPD is a module including a two-dimensional sensor matrix composed of 256 $\times$ 160 cells (pixels) covering 12.8 $\times$ 70.7 ($r\phi \times z$) mm^2 active area. Each cell measures 50 μm and 425 μm in the $r\phi$ and the z direction, respectively. In total, 240 modules are installed (80 for the 1^{st} layer and 160 for the 2^{nd} layer) resulting in 9.8 $\times$ 10^6 cells providing clear two-track separation and precise position resolution with fast read-out in 25.6 μs as digital output.

The module of the SDD [190] is 300 μm thick and has an active area of 70.2 $\times$ 75.3 ($r\phi \times z$) mm^2 , split into two drift regions by a central cathode. Each drift region consists of 256 anodes with a pitch of 294 μm collecting the charge drifting orthogonally to the beam axis. On the surface of the module, the cathode strips with 120 μm pitch fully deplete the detector volume and generate the drift field. The coordinate along the beam axis is obtained directly from the position of the anode. The coordinate in the transverse plane with respect to the beam axis is derived from the drift time. The $\mathrm{d}E/\mathrm{d}x$ information for particle identification is read as an analogue signal. Since the readout time of the SDD is about 1 ms, part of the data was recorded without SDD information [191]

Double-sided silicon strip sensors with an active area of 73 $\times$ 40 ($r\phi \times z$) mm^2 are the basic units for the SSD. Each side of the sensor is composed of 768 strips with a pitch of 95 μm and length of 40 mm. The strips on one side of the sensor (p-type) are oriented at an angle of 7.5 mrad with respected to the beam axis and those on the other side of the sensor (n-type) are at an angle of 27.5 mrad, resulting in a 35 mrad stereo angle. For certain azimuthal angles, there are four different strip orientations, as a result of mounting the sensor p-type(n-type) in the inner(outer) layer of the SSD facing the beam pipe. This reduces the fake track probability significantly by reducing the rate of ambiguities in track reconstruction. In addition, as the strip orientations are nearly parallel to the magnetic field, the better position resolution is obtained in the bending direction. The sensors have a thickness of 300 μm, to provide a reasonable signal-to noise ratio for analog readout, the $\mathrm{d}E/\mathrm{d}x$ information for particle identification.

3.3.3 Global tracking

The reconstruction of the primary vertex is one of the main tasks of the SPD. The reconstruction starts by building SPD tracklets, virtual lines made from pairing clusters from each layer. The space point which gives the minimum distance for all contributing tracklets is defined as the primary vertex and is used as an input for global tracking. Global tracking is performed in three stages as shown in Figure 3.4. The track reconstruction starts from the outermost TPC by building the track seeds with two TPC clusters and the primary vertex reconstructed with SPD tracklets. The track candidates are propagated inwards to the inner TPC radius, the innermost ITS layer and primary vertex. Based on the point of the closest approach to the primary vertex obtained by extrapolation of the reconstructed track, the outward propagation starts. The tracks are refitted by the Kalman filter [193] in this step, using the clusters found at the previous inward propagation. The tracking continues outwards up to the TOF or detectors located at larger radii such as the EMCal if they are available for the propagation. Nevertheless, the detectors located outside the TPC do not contribute in the update of the track properties, but their information is stored as additional track properties. In the final stage, the refit is performed again inwards and the track parameters are determined. Then, the interaction vertex with better precision than the one from SPD tracklets are extracted again based on reconstructed tracks.

The track distance of the closest approach to the primary vertex, the so-called impact parameter (d_0) is one of the crucial track properties in analyses using the displaced secondary vertex information,

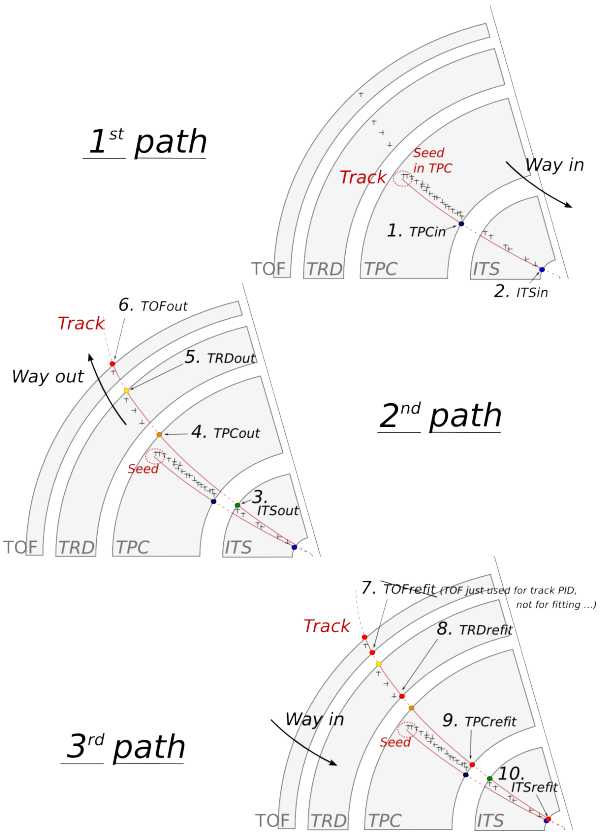

Figure 3.4: An illustration of global tracking in the ALICE central barrel. Figure taken from [192].

like this thesis work. In ALICE, the transverse impact parameter, $d_{0,\mathrm{xy}}$, is frequently used since the tracks are bent due to the magnet and more granular active area of the SPD provides better resolution in transverse plane. Figure 3.5 shows the illustration of $d_{0,\mathrm{xy}}$ for a track originated from the primary interaction vertex and secondary vertex. Ideally, a track originating from the primary interaction vertex has $d_{0,\mathrm{xy}} = 0$. The $d_{0,\mathrm{xy}}$ of a track originating from secondary vertex, however, is proportional to the distance between the primary and secondary vertex, so-called flight distance. The measured $d_{0,\mathrm{xy}}$ for a track originated from the primary interaction vertex, however, can be non-zero due to the finite detector resolution as well as the straggling of a track traversing the detector material. For example, Figure 3.6a shows the $d_{0,\mathrm{xy}}$ of reconstructed electron candidates from Dalitz decays of π^0 in data in $1.6 < p_{\mathrm{T}} < 2.0\mathrm{GeV}/c$, fitted with a Gaussian and symmetric exponential tails. The mean of the distribution is at 0 and the width, representing the resolution of $d_{0,\mathrm{xy}}$, is about few 10 μm. Figure 3.6b shows the resolution of $d_{0,\mathrm{xy}}$ for pions, kaons and protons reconstructed with the ITS and the TPC in pp collisions at $\sqrt{s}$ = 7 TeV as a function of p_{T} compared with the corresponding simulations. First, the p_{T} and particle-species dependence of the $d_{0,\mathrm{xy}}$ resolution is clearly seen, which originates from the multiple scattering effects [194]. Although the overall trend of the $d_{0,\mathrm{xy}}$ resolution is well described by MC simulation, at the same time, small discrepancies between the data and MC simulation are observed which indicate that the spatial resolution of reconstructed track in data is not precisely described in MC simulation. The physics observable in this thesis is extracted based on the decay length, which highly depends on spatial resolution of tracks, from MC simulations. Therefore, it was essential to estimate the impact of

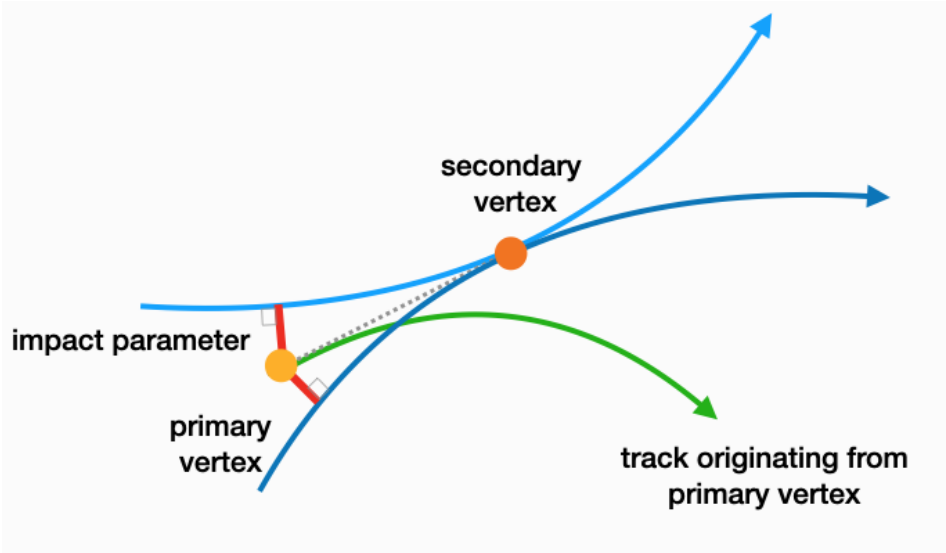

Figure 3.5: An illustration distance of the closest approach to the primary vertex for a track originating from the primary vertex and secondary vertex in the transverse plane perpendicular to beam axis.

the discrepancy in this thesis as well as to understand the origin of the discrepancy. Various studies were carried out and described in Chapter 4.

The Figure 3.7 shows the transverse momentum (p_{T}) resolution as a function of the inverse of p_{T}. It is clearly visible that constraining the primary vertex significantly improves the resolution of TPC standalone tracks. In addition, better resolution is achieved for tracking performed with the TPC and the ITS combined. Using reconstructed tracks, the primary vertex is recalculated providing a higher precision than the one from SPD tracklets only.

3.4 Electron trigger with Transition Radiation Detector (TRD)

3.4.1 Transition Radiation Detector (TRD)

Various probes of the QGP involve electrons, e.g. dielectron pairs from direct decays of vector mesons (ρ, ω, ϕ, J/ψ, Υ, ...), electrons from Dalitz decays of scalar and pseudoscalar mesons (π^0, η, η', ...) and from thermal radiation of the QGP, as well as single electrons from the decays of open heavy-flavour hadrons which have substantial branching ratios. The ALICE Transition Radiation Detector (TRD) was originally built to provide electron identification in the central barrel for momenta above 1 GeV/c, enabling the measurement of those probes for the large charged-particle multiplicities of heavy-ion collisions. In addition, it was designed to derive a fast trigger for charged particles with high momentum not only for rare probes associated with electrons but also for jets. As clearly indicated by its name, the TRD is based on the transition radiation (TR) which occurs when an ultra-relativistic particle ($\beta\gamma > 800$) crosses the border between materials with different dielectric constants.

The TRD is located in the central barrel of the ALICE detector, it surrounds the TPC at a radius from 2.90 m to 3.68 m. The basic building block of the TRD is a multi wire proportional chamber (MWPC)

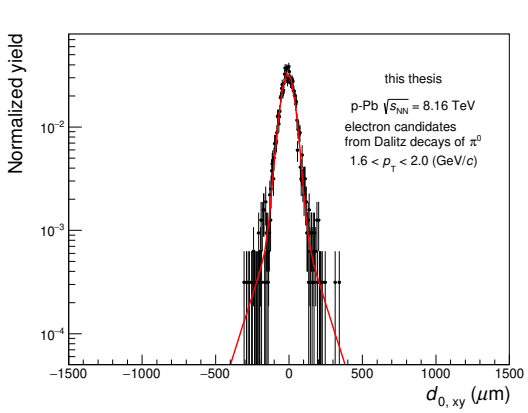

(a) Identified particles in pp collisions for data and simulation (MC).

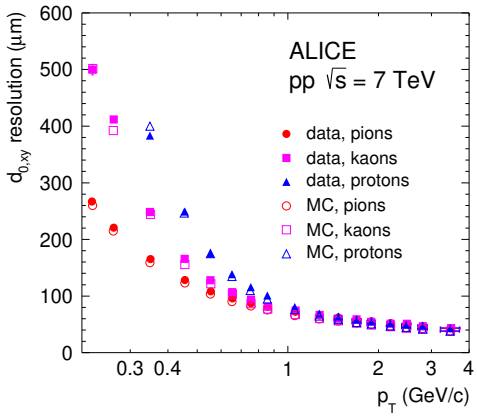

(b) Identified particles in pp collisions for data and simulation (MC).

Figure 3.6: Resolution of the $d_{0,\mathrm{xy}}$. The contribution of the primary vertex resolution is included. Figures taken from [191].

as illustrated in Figure 3.8 [196]. Each chamber has pad readout preceded by 3 cm of drift region filled with a Xe-CO_2 (85-15) gas mixture with a drift field of 700 V/m, resulting in a drift velocity of 1.56 cm/μs. A radiator, made up of polypropylene fibre mats of 3.2 cm thickness sandwiched between two plates of laminated carbon fibre sheets of 100 μm thickness, is mounted in front of the drift region. Six chambers are layered in radial direction to form a stack. A sector, a bundle of the five stacks along the beam direction, is combined in a mechanical casing with all service connections and called as supermodule. In full azimuth, 18 supermodules are installed matching to the 18 trapezoidal sectors in the TPC. Exceptionally, the middle stack of three sectors located at the azimuthal coverage of the PHOS detector were not installed to minimise the material in front of the PHOS detector. In total, 522 individual readout chambers are installed. The active area and the geometry of the cathode pad plane for each chamber were adjusted to achieve a homogeneous granularity in radial direction and along the beam direction. The active area per chamber varies radially and along the beam axis from 0.9 m $\times$ 1.06 m to 1.13 m$\times$ 1.43 m ($y \times z$), resulting in the total active area of the TRD of 673.4 m^2. The cathode pad plane of each chamber is segmented into 16 pads (12 pads for the chambers located in the middle stack of each supermodule) along the z-direction and 144 pads in the bending plane ($r\phi$ plane). The small width of the pad row in the bending plane ($r\phi$ plane) varies from 0.635 cm to 0.785 cm radically. This size of the width enables the charge to be shared over typically three adjacent pads, resulting in a spatial resolution of 400 μm in the bending plane. The length of the pad from 7.5 cm to 9.0 cm along the beam-axis provides sufficient resolution along the beam direction for reconstructing and matching the track with the TPC, which is improved by tilting the pads by $\pm$ 2° (sign alternating layer-by-layer) in $z-$direction. Overall, there are 1150848 readout channels within the TRD covering full azimuth and $-0.84 < \eta < 0.84$.

The average pulse height, which is proportional to the charge deposition, is shown as a function of drift time for electrons and pions in Figure 3.9. For all distributions, an arbitrary offset of 0.3 μs is shown. The time axis can be read as the distance between cathode pad and the point where the source of

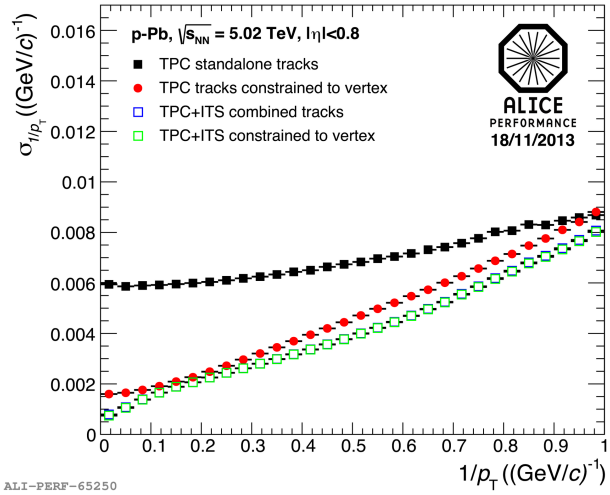

Figure 3.7: Inverse-p_{T} resolution ($\frac{\sigma_{p_{\mathrm{T}}}}{p_{\mathrm{T}}} = p_{\mathrm{T}}\sigma_{\frac{1}{p_{\mathrm{T}}}}$) for tracks reconstructed in different ways, standalone TPC and ITS–TPC tracks with and without constraint to the primary vertex estimated with the SPD tracklets. Figure taken from [191].

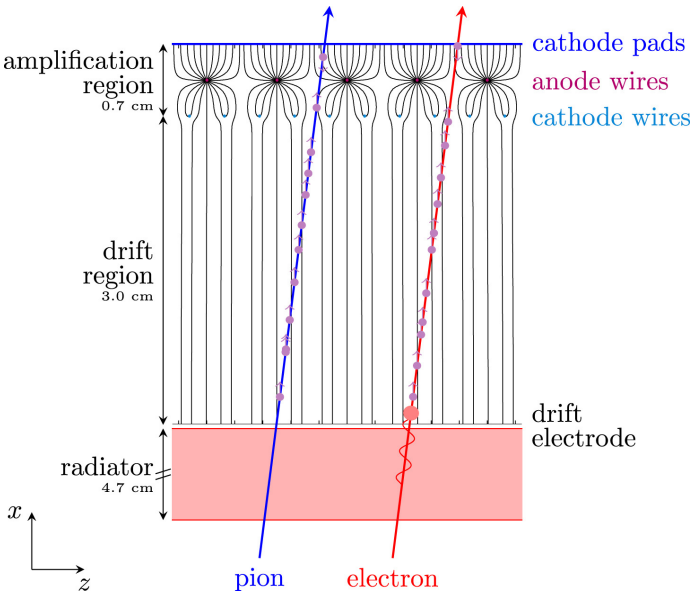

Figure 3.8: A schematic view of the TRD readout chamber in $x - z$ plane with tracks of an electron and a pion. Drift lines are calculated with Garfield [195] for nominal operation conditions. Circles along the drift lines indicate charge deposition. The short wave and the large circle along the electron trajectory represent the transition radiation photon and its absorption. Figure taken from [196].

signal is generated. For instance, the large amplitude shown at early times is from the amplification region and peak position in the amplification region represents the position of the anode wire, caused by charges coming from both sides of the anode wires. The average pulse height is the gain in the TRD, which is composed with the ionization energy loss created by the particle traversing the drift region and TR. The difference of the ionization energy loss between pions and electrons is clearly visible in the Figure 3.9, by comparing the pulse height of pions and electron without TR. From the comparison of electron with and without TR, the contribution of TR can be clearly seen at late times, i.e. the time

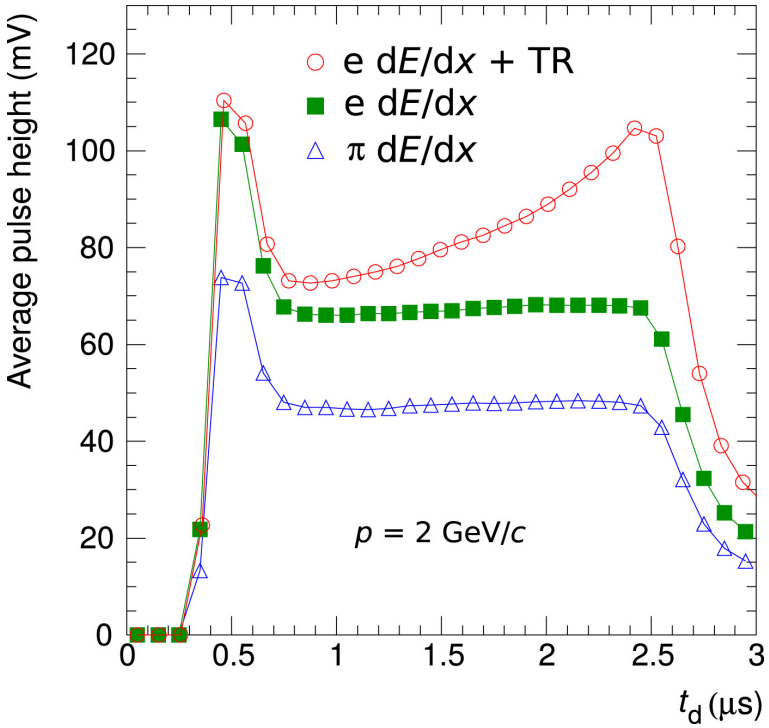

Figure 3.9: Average pulse height as a function of drift time for electrons and pions, measured with a prototype read-out chamber at a CERN test beam. Figure taken from [197].

around 2.5 μm, corresponding to the entrance of the chamber where the TR photons are most likely to be absorbed. Tails of the distributions reflect the slow ion movement. One of the variables expressing the electron identification performance in the TRD is a pion rejection factor, which is defined as the inverse of the fraction of pions that are incorrectly identified as electrons. At a momentum of 1 GeV/c, the pion rejection factor better than 100 at an electron efficiency of 90% in p–Pb collisions was obtained. And the pion rejection factor gradually decreased to about 50 at $4 < p < 5$ GeV/c [198].

3.4.2 TRD electron trigger

The Central Trigger Processor (CTP) of the ALICE detector evaluates the trigger inputs from the trigger detectors and the LHC burst crossing signal and generates the trigger decision. In ALICE, the trigger inputs are divided into three different levels upon their associated latencies, Level-0 (L0), Level-1 (L1) and Level-2 (L2). The decision of the L0 is made in 0.9 μs after the collision using the input from fast detectors such as V0, SPD and T0, mainly to trigger the minimum-bias interaction and sent to the detectors in 1.2 μs. The events accepted at L0 are further evaluated with the L1 trigger inputs with specific Physics interest from the slower detectors due to their computation time including TRD and the long propagation time (ZDC) arriving in 6.1 μs at CTP. The L1 trigger decision is made at about 6.5 μs. The L2 trigger is issued after about 100 μs after the collision which dictated by the drift time of the TPC. The interval 100 μs is the time window during the TPC gating grid open and ionization electrons from the TPC drift volume can enter the amplification region. The gating grid has to be closed for 300–500 μs to keep the drift volume free of large space-charge accumulations from back-drifting ions [182].

The main purpose of the L2 trigger is to prevent events with multiple collisions from different bunch crossings piled-up in the TPC (past–future protection).

As shortly mentioned above, the TRD contributed to the L1 trigger during the LHC Run 1 and Run 2. Besides zero-suppressed readout of ADC data (raw data), the TRD supports so-called tracklet read-out in online. The trigger input is evaluated from the online reconstructed tracklet within a stack to select the events having physics observables, i.e. high p_{T} electrons, light nuclei and jets. In the following subsections, the local online tracking and global online tracking as well as the triggering on electrons with the TRD are discussed.

TRD Front-End Electronics (FED) and tracklets

Each readout chamber is equipped with 6 (for central stacks in each supermodules) or 8 readout boards (ROB). On each ROB, 16 Multi-Chip Modules (MCM) are mounted in order to connect to pads and to process the data. For some chambers, there are additional MCMs for merging signals from other MCMs. Each of the 65000 MCMs used for data processing is directly connected to 18 pads and hosts two custom chips, an analog PreAmplifier and ShAper (PASA) and a TRAcklet Processor (TRAP). The induced signal on the cathode pad plane, typically 7 μA during 1 ns, is amplified and optimally shaped for the digitization through the PASA and fed into the TRAP ADC. The TRAP digitizes the signal with a sampling frequency of 10 MHz corresponding to time bins of 100 ns. The number of time bins can be configured in the FEE and at maximum 30 time bins are technically supported. Considering the drift time, 22 time bins were chosen for Run 2 operation to reduce the unnecessary readout time and the data volume.

The next step of the signal processing is handled by a configurable digital filter chain after appending two digits to the ADC output to avoid rounding effects. First, through the pedestal filter, the channel-specific baseline is subtracted from the pedestal of the signal and a common baseline is added again to guarantee that all signals have a configurable value. Then, the gain filter plays a role, correcting for the local variation of the gain. Correction factors for individual channels are obtained from dedicated calibration runs with meta-stable Krypton ($^{83\mathrm{m}}$Kr) added to the gas system [199], using the decay energy of Krypton ($^{83\mathrm{m}}$Kr) to the ground state. There are additional filters in digital filter chain [200], but not used for the Run 2 data taking.

The filtered data are sent to a hardware pre-processor for cluster finding. In order to determine a cluster, time bin-wise data from three adjacent pads are used [201]. A set of pads should fulfil the following selection criteria to be a cluster, 1) the charge of three neighboring pads has to exceed a certain threshold which can be configured in the FEE and 2) the central pad has the largest charge. The local transverse position of found clusters is defined as the centre of gravity of the charges calculated with a correction based on the pad response function using look-up tables. For each channel, the sums of several properties (the number, $y-$positions, time bins and charge of found clusters) are calculated and stored for further processing. A maximum of four channels, having the largest number of clusters in the MCM and fulfilling the following two conditions, can be further processed on the CPUs, 1) the number of clusters

found exceeds a certain threshold which can be configured in the FEE, and 2) the sum of the number of clusters found in given channel and in neighboring channel exceeds another configurable threshold. In the CPU, the channel-wise sums are accumulated with those of the neighboring channels, considering the shift in transverse position of the neighboring channel. Then, a straight line fit ($y(t) = y + b \cdot t$) is computed to obtain the transverse position (y) with respect to the centre of the chamber and the deflection over the bending plane (d_y) as illustrated in Figure 3.10. The latter one is converted from the

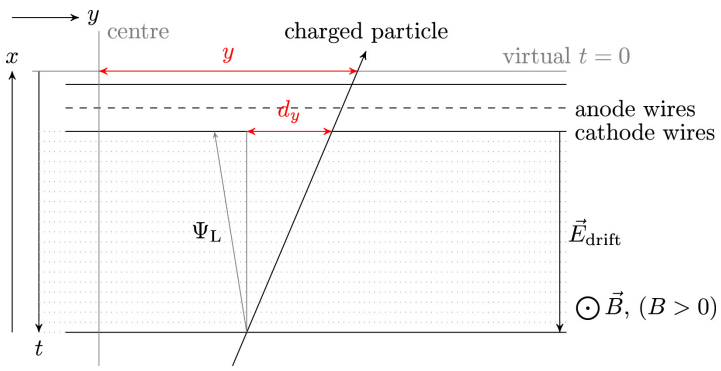

Figure 3.10: A sketch of the tracklet reconstruction processed in the TRAP presented in the xy plane. The transverse position y with respect to the centre of the chamber at the beginning of the drift time (virtual t = 0) and the deflection d_y are obtained from the described fit. The effect of the Lorentz drift is represented by Lorentz angle Ψ_L. Figure taken from [196].

slope parameter (b) using known parameters of pad width, drift velocity and drift length. The resulting y and d_y from the fit are corrected for the effect of the pad tilt of 2° with respect to the z axis as the tilted pad introduces as small z–position dependency for y and d_y. In addition, there is another effect which is considered for better description of d_y. Due to the presence of a magnetic field perpendicular to the drift field, the drift path is not a straight line perpendicular to cathode plane, but tilted by Lorentz angle (Ψ_L) as shown in Figure 3.10. Both effects were calculated for each MCMs in advance as constant values, stored and corrected in the TRAP [202]. The longitudinal z position is derived from the position of the pad row, matching to the MCM. The accumulated charge is translated into the likelihood value of electron (PID value), based on the total integrated charge distribution of electrons in a configurable look-up table. The tracklet information is encoded into a 32-bit word, merged in merger MCMs and sent to the Global Tracking Unit (GTU) through Optical Readout Interfaces (ORI) via optical links (DDL).

Global online tracking

The data is transmitted stack-wise to the corresponding Track matching units (TMUs) implemented in the FPGAs of the GTU. As a first step, tracklets are first grouped by their positions in the xz plane. The tracklets of each selected group are projected onto a virtual yz plane in the middle of the stack. The groups having at least four tracklets which are close enough to assume that they are originating from the same track are selected for online track reconstruction. The position of the tracklets are fit with straight lines which is a reasonable approximation of the trigger-relevant tracks above 2 GeV/c as they have little curvature. The transverse offset a from the nominal primary vertex position is translated into $1/p_{\mathrm{T}}$ of the reconstructed track. In addition, the average PID value of tracklets contributing to

the track reconstructed online is assigned as a PID value for the track. The information of the five TMUs from same supermodule are combined on the SuperModule Unit (SMU) and delivered to the Data AcQuisition system (DAQ) for the trigger decision. The online tracks and matching offline track correlation and the width of the trigger turn-on curve were used for parts of the quality assurance of the online reconstructed tracks. The results give about 10% momentum resolution for online-reconstructed tracks with momenta of 1.5 - 5 GeV/c [196].

Trigger on electrons

As briefly discussed in the previous section, the TRD measures the specific energy loss in the gas and the transition radiation of charged particles passing through. Figure 3.11 shows the average charge per

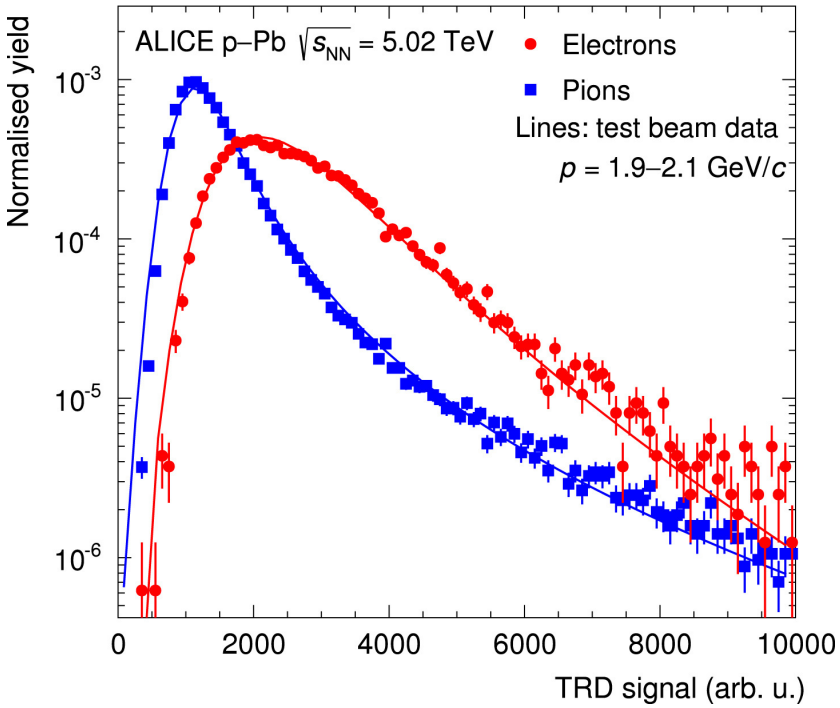

Figure 3.11: Total integrated charge normalized to the tracklet length measured in a single read-out chamber for electrons (circle) and pions (square) in p–Pb collisions at $\sqrt{s_{\mathrm{NN}}} = 5.02$ TeV for $1.9 < p < 2.1$ GeV/c. Sold lines along the data points represent results from test beam measurements [197, 203]. Figure taken from [196].

unit tracklet length measured in a single read-out chamber for electrons and pions in p–Pb collisions at $\sqrt{s_{\mathrm{NN}}} = 5.02$ TeV for $1.9 < p < 2.1$ GeV/c. In order to obtain electrons and pions with high purity, in addition to the particle identification with the TPC and TOF, topological selection criteria were applied to select electrons from photon conversion in material ($\gamma \rightarrow \mathrm{e^+e^-}$) and charged pions from K^0_s ($\mathrm{K}^0_{\mathrm{s}} \rightarrow \pi^+\pi^-$). As already seen in Figure 3.9, the charge deposition of electrons is larger than pions due to the larger specific energy loss of the ionization and transition radiation. The results are consistent with measurements taken at the CERN PS in 2004 with electron and pion beams [197, 203] and used for online particle identification for the trigger decision. The charge distribution of electrons is written on one-dimensional universal look-up table considering a correction factor for the tracklet length. The look-up table is stored on MCM and used to calculate the electron likelihood of reconstructed track as

discussed in the previous section. An electron likelihood, which has a value between zero and one, is translated into an integer PID value from 0 to 255 (unsigned 8 bits). So, the trigger decision for high-p_{T} electron is derived from p_{T} and the PID value.

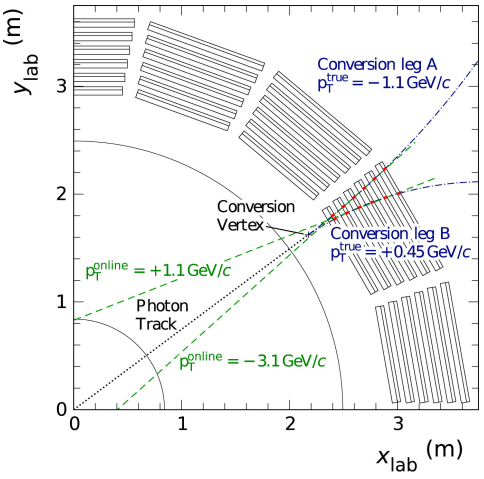

Figure 3.12: Electron-positron pair produced by photon conversion at a large radius, in front of the TRD shown in the transverse plane. Figure taken from [196].

There were two modes for high-p_{T} electron trigger available in the LHC Run 2 data taking period. One mode (HSE) is defined with a p_{T} threshold of 3 GeV/c focusing on reaching a higher p_{T} range in the measurement of electrons from semileptonic decays of heavy-flavour hadrons. For another mode (HQU), the p_{T} threshold is set to 2 GeV/c to cover most of the cross section of quarkonium production. The PID threshold for each mode is optimized to have both triggers run at the similar rate. The PID is set to 120 and 135 for HSE and HQU, respectively, achieving a rejection of minimum bias events by a factor of about 100. The dominant background of the electron triggers is caused by electrons from "late" conversion of photons at large radii, which is especially problematic in online tracking as the track reconstruction algorithm is designed based on the assumption that tracks originate from the primary vertex. As illustrated in Figure 3.12, the reconstructed conversion leg tends to have larger p_{T} than the actual value due to their displaced conversion vertex. In order to suppress the contribution of late conversions, two additional conditions are required for online reconstructed tracks. One condition is that the track must have at least five tracklets and one of which must be in the innermost layer of the TRD. Another is that the Sagitta in the readout chambers ($\Delta 1/p_{\mathrm{T}}$) calculated online must be smaller than a certain upper limit, which was optimized to $0.2c/\mathrm{GeV}$ for the Run 2 data taking period [204].

The specific energy loss in the TPC of electrons for the minimum bias data sample and the TRD electron triggered data sample is presented in Figure 3.13. It is clearly visible that the ratio of electrons to hadrons is much larger for the triggered data sample. The further suppression of hadrons was achieved by using the offline TRD PID information. To quantify the enhancement of electrons with the trigger, an enhancement factor is calculated as a ratio of the number of electrons in the TRD triggered data sample to the one in the minimum-bias data sample. The enhancement factor as a function of p_{T} in p–Pb collisions at $\sqrt{s_{\mathrm{NN}}} = 8.16$ TeV is presented in Figure 3.14. First, the turn-on curve around p_{T}

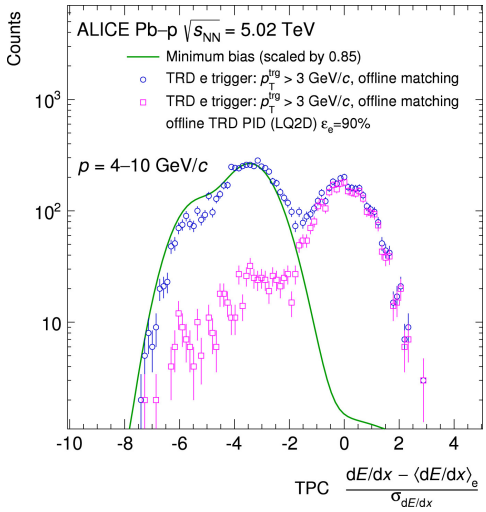

Figure 3.13: TPC $\mathrm{d}E/\mathrm{d}x$ expressed as a deviation from the expected energy loss of electrons, normalized by the energy loss resolution in p–Pb collisions at $\sqrt{s_{\mathrm{NN}}} = 5.02$ TeV for tracks with momenta of 4 - 10 GeV/c. Events which are likely to be triggered by electrons from photon conversion were rejected by matching the online track with a track in the TPC. The distribution of the minimum bias data sample is scaled by 0.85 to match its maximum to the maximum of the distribution for the triggered data sample. Figure taken from [196].

threshold is clearly visible in both configurations. The enhancement factor of the HQU trigger is about 62 and that of the HSE trigger is about 82. The further properties of the TRD triggers for electrons including the trigger efficiency will be discussed in Chapter 4.

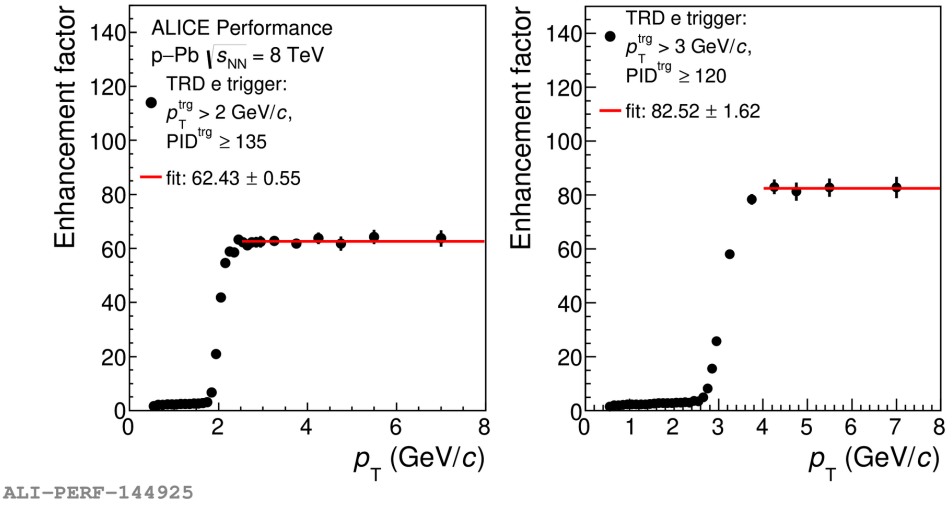

Figure 3.14: Enhancement factor of the TRD electron triggers as a function of p_{T} (left for HQU and right for HSE) in p–Pb collisions at $\sqrt{s_{\mathrm{NN}}} = 8.16$ TeV obtained by comparing the number of electrons in the TRD triggered data sample to the one in the minimum bias data sample.

4 Data and Monte Carlo samples, and calibration of the Monte Carlo Simulation

4.1 Data sample

The data sample used in this thesis work was collected by the ALICE detector described in Chapter 3 in week 47 and 48 in 2016, where proton and lead beams were brought into collisions. The proton and lead beams had an energy of 6.5 TeV and 2.51 TeV per nucleon, respectively, resulting in a nucleon–nucleon centre-of-mass collision energy of $\sqrt{s_{\mathrm{NN}}}$ = 8.16 TeV. The asymmetry of the beam energy per nucleon leads to a shift of the nucleon–nucleon center-of-mass rapidity frame in direction of the proton beam by $\Delta y = 0.465$. The data sample consists of two data taking periods having opposite beam direction, one with protons going towards and another with lead ions moving towards the direction of the muon spectrometer. The data sample from both periods was combined to reduce the statistical uncertainty and referred to as p–Pb collisions from hereafter. The recorded events were reconstructed as described in previous chapter, containing lists of charged tracks as well as global event properties used for this thesis work.

Not all collected events can be used for the analysis. For example, one or more collisions occurring in bunch crossings different from the one which triggered the acquisition and beam induced background events were removed using the time information of the V0 detector. In addition, several criteria based on reconstructed vertex were required to guarantee full ITS acceptance and to reject unwanted collisions from other bunches, summarized in Table 4.1. The contributions of nonphysical events got negligible.

selection criteria
$\lvert z$ position of global vertex$\rvert < 10\ cm$
$\lvert$Difference between z position of global vertex and of SPD vertex$\rvert < 0.5\ cm$
Resolution of z position of SPD vertex < 0.25

Table 4.1: List of event selection criteria applied in this analysis. The SPD vertex refers to the reconstructed vertex only with SPD tracklet information while the global vertex was reconstructed with the full central barrel tracking.

As described in Chapter 3, two independent TRD electron triggers were available during the data taking period. Since the triggers were independently operated, a fraction of the events satisfies both trigger conditions. The triggered events were selected in the offline analysis by level-1 filterbit information, having at least one electron trigger.

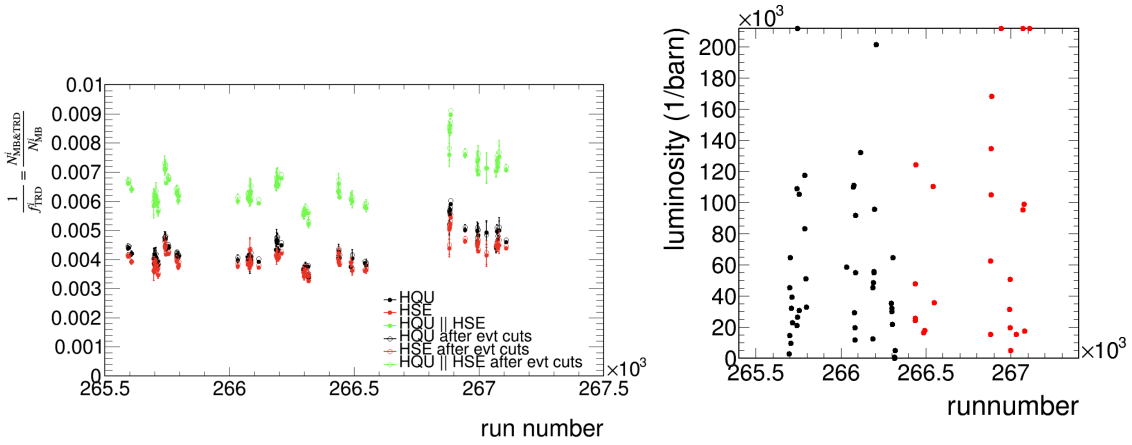

Figure 4.1: (Left) Inverse of the trigger normalization factor as a function of run number for HQU, HSE and HQU+HSE. Open symbols show same quantity obtained after applying event selection criteria listed in Table 4.1. (Right) Integrated luminosity of the TRD triggered events (HQU+HSE) used in this analysis as a function of run number. Black ad red points stand for p–Pb and Pb–p collisions respectively. Figures taken from [205].

4.1.1 Luminosity

The integrated luminosity of the data sample was determined from the number of equivalent minimum bias events (N_{MB}), divided by the minimum bias cross section obtained from Van der Meer scan (see below) σ_{MB}, $\mathcal{L} = \frac{N_{\mathrm{MB}}}{\sigma_{\mathrm{MB}}}$. The integrated luminosity was estimated for each run, a small chunk of data sample collected closely in time that included events sharing similar data taking conditions.

Since TRD-triggered events were required to have an absolute z position of the global vertex smaller than 10 cm for the analysis, some fraction of the events was excluded due to the absence of reconstructed vertex. In other words, the total number of TRD triggered events (N_{TRD}) is not equivalent to the number of the events used in the analysis, thus, had to be estimated separately. As a first step, $f_z^i = \frac{N^i(|z|<10cm)}{N^i(|z|<\infty)}$ was evaluated for each run, i, by fitting to z-vertex distribution with Gaussian function. Assuming that there is no difference between $z-$component of vertex distribution of events with reconstructed vertex and without, N^i_{TRD} was estimated by scaling the total events without applying selection criteria on vertex information (N^i_{raw}) with f_z^i, $N^i_{\mathrm{TRD}} = f_z^i \times N^i_{\mathrm{raw}}$. Then, the trigger normalization factor (f^i_{TRD}) was defined as a number of minimum bias events equivalent to one TRD triggered event. The fraction of minimum bias events which in addition have the TRD trigger input present was evaluated as shown in the left of Figure 4.1 for each run, which is the inverse of the trigger normalization factor ($\frac{1}{f^i_{\mathrm{TRD}}}$). The corresponding uncertainty was calculated based on binomial distribution as the numerator is subset of the denominator. Finally, the number of equivalent minimum bias events (N_{MB}) was determined as $N^i_{\mathrm{MB}} = f^i_{\mathrm{TRD}} \times N^i_{\mathrm{TRD}} = f^i_{\mathrm{TRD}} \times f^i_z \times N^i_{\mathrm{raw}}$.

The visible cross-section of minimum bias events was determined via Van-der Meer scans for each beam direction, σ_{MB} = 2.09 ± 0.03 b and 2.10 ± 0.04 b for p–Pb and Pb–p collisions respectively [206]. With these numbers, the integrated luminosity was calculated for each run as presented in the right of Figure 4.1, resulting $694.8 \pm 13.3 \mu$b in total.

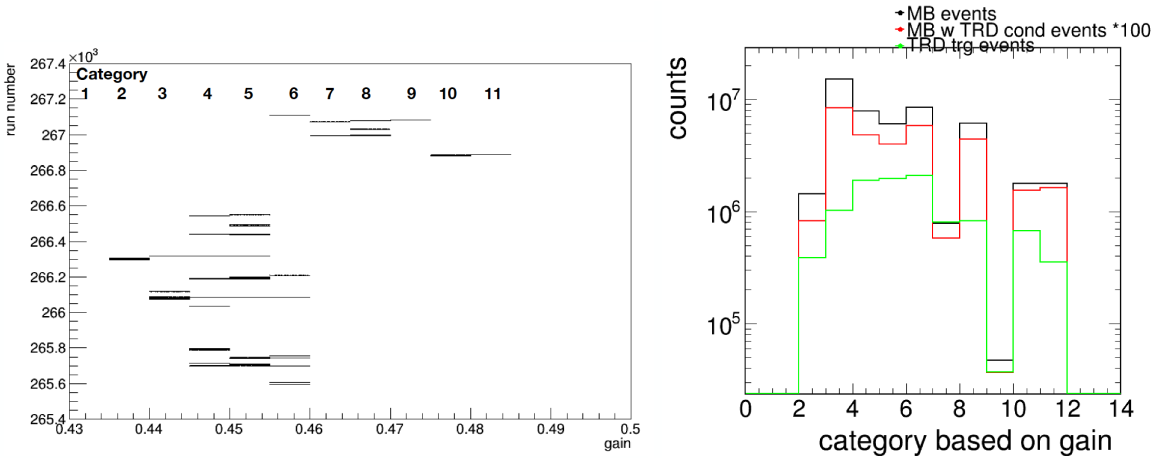

Figure 4.2: (Left) Average gain of the TRD for each run. Binning of the gain was adjusted considering the measurement precision of the gain, which is about 1.4% [196]. Categories for the trigger efficiency estimation were presented on left upper corner. (Right) Number of events in each category for minimum bias events (black), minimum bias events having the TRD trigger input present scaled by 100 for visualization (red) and TRD triggered events (green). Figures taken from [205].

4.1.2 TRD single electron trigger efficiency

Similar to the determination of the trigger normalization factor, minimum bias events and the subset of them having the TRD trigger input present were used for the trigger efficiency estimation. It should be noted that the data for global event and TRD trigger was separately read and stored in the raw data and only the data for global event was used for the event reconstruction, so that, the TRD online track information could not be directly associated with global tracks in reconstructed events. For tracks in the events, several selection criteria described in Table 5.1 were required for electron identification. Then, the trigger efficiency was calculated as a function of p_{T} by

$$\epsilon_{\mathrm{trg}}(p_{\mathrm{T}}) = \frac{N_e^{\mathrm{MB+TRD}}(p_{\mathrm{T}})}{N_e^{\mathrm{MB\ events}}(p_{\mathrm{T}})} \tag{4.1}$$

where $N_e^{\mathrm{MB\ events}}$ and $N_e^{\mathrm{MB+TRD}}$ represent the number of electrons in minimum bias events and in subset of minimum bias events, which also have the TRD trigger input respectively.

As a gaseous detector, the TRD gain which is directly connected to the particle identification capability, can change sensitively by small variation of pressure and gas composition. During the operation, these effects could be mitigated by adjusting high voltage of the detector. Nevertheless, to cope with residual effects, the average gain over all TRD chambers was investigated for each run as illustrated in Figure 4.2. In order to avoid statistical fluctuations, runs with similar gains were grouped. For each group, the trigger efficiency defined as Equation 4.1 was estimated. Since the fraction of events in each gain group is different for the minimum bias events and TRD triggered events as shown in Figure 4.2 (right), the obtained trigger efficiency for each group was averaged with the number of TRD triggered events as a weight. The resulting trigger efficiency for the two trigger operation modes, HSE and HQU are presented separately for electrons and positions in Figure 4.3. First of all, the different trend between

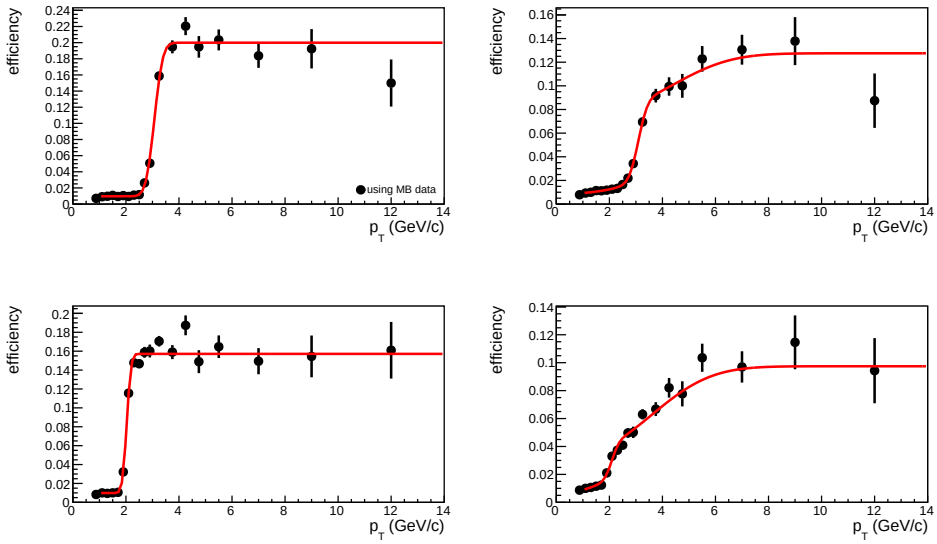

Figure 4.3: TRD trigger efficiency (HSE top row and HQU bottom row) for electrons (left column) and positrons (right column) given as a function of the reconstructed p_{T}. The lines indicate the fit functions for the parameterization described in the text in detail. Figures taken from [205]

electrons and positrons is seen for both HSE and HQU as expected due to the $E \times B$ effect. Though the reconstructed p_{T} shown on the x-axis is not exactly the same as the TRD online p_{T} used for the trigger decision, all four distributions show the onset of the p_{T} threshold. As briefly mentioned above, since TRD online tracks could not be matched to reconstructed tracks, in case there are more than 1 electron in the events, not only the electron which actually triggered the given event, but all electrons enter in the efficiency calculation. As a consequence, even below the p_{T} threshold, a non-zero trigger efficiency was obtained for all cases. This additional contribution was studied in more detail with the MC sample, discussed in the next sub-section. The red solid lines along the data points in Figure 4.3 show the functional parameterization of the measured trigger efficiency. An error function with a constant offset was used to describe the measurement of electrons while one more error function was added for the description of positrons.

Possible dependence of the trigger efficiency on η and ϕ was studied via calculating the integrated efficiency as a function of η and ϕ with high p_{T} electrons and found to be negligible [205]. And the obtained trigger efficiency was cross-checked with an alternative method using the trigger normalization factor obtained for the luminosity estimation (f_{TRD}) in following:

$$\epsilon(p_{\mathrm{T}}) = \frac{\frac{\text{number of electrons in TRD triggered events}}{(\text{number of TRD triggered events}) \times f_{\mathrm{TRD}}}}{\frac{\text{number of electrons in minimum bias events}}{\text{number of minimum bias events}}}, \tag{4.2}$$

which gives similar results.

4.2 Monte Carlo simulation

Dedicated Monte Carlo (MC) simulations were produced to better understand the detector response of the signal, J/ψ in this analysis, and correct for geometrical acceptance and efficiency introduced by applying selection criteria to enhance the signal to background ratio. Minimum bias p–Pb collisions were simulated with the EPOS-LHC model [207]. For 70% of the minimum bias events, one J/ψ meson per event with a flat rapidity distribution and a natural p_{T} distribution from previous measurement [208] was embedded to simulate the prompt J/ψ production. Based on the J/ψ polarization measurements [119], the J/ψ mesons were simulated unpolarized. For the remaining 30 % of the events, a $b\bar{b}$ pair per event was added and forced to decay into J/ψ with PYTHIA 6.4 [81] to generate non-prompt J/ψ. The decay of J/ψ to di-electrons was governed by EvtGen [209] with enabling PHOTOS [210] for QED radiative corrections in the decays. All generated particles were transported through the detector setup using GEANT3 [211] considering a realistic detector response and reproducing the detector performance during the data taking period. Due to the imperfection of MC describing data, some corrections of the MC simulation were required. In this analysis, a correction was applied for the improper description of the track pointing resolution and of the TRD trigger performance in MC which are described in following sections.

4.3 Calibration of the trigger efficiency in Monte Carlo simulations

As well as other detectors, the TRD response was simulated in the MC production. Nevertheless, the trigger efficiency in the MC sample shows a large discrepancy with respect to data as presented in Figure 4.4. As shown in Figure 4.5, TRD PID distribution of data and MC looked similar, further study was focused on other effects than trigger performance itself, such as the abundances of particles, electrons in particular.

Upper plots in Figure 4.6 show the trigger efficiency for the events with prompt J/ψ and events with a beauty quark pair forced to decay to non-prompt J/ψ separately. The difference of the trigger efficiency between the events with prompt J/ψ and events with beauty quark pair forced to decay to non-prompt J/ψ became much smaller when the events were required to contain only one J/ψ per event, as shown in the bottom plots of Figure 4.6. Based on this result, the events with beauty quark pair to non-prompt J/ψ were excluded from the further study of the trigger efficiency as having more than one non-prompt J/ψ in the event with beauty quark pair is extremely rare in real data sample considering the branching ratio and introducing artifact. The effect of the electron abundance in the MC sample was further studied. As presented in the upper two plots of Figure 4.7, the trigger efficiency of MC events containing prompt J/ψ were decomposed in three types of events, the events triggered by an electron, by a positron and by a hadron other than electron or positron. Assuming that di-electron decay mode is far less likely to happen in real data with respect to decay modes creating the single electrons, the events triggered by a counter-particle were excluded and compared with data as shown in the bottom two plots of Figure 4.7. The subtraction of those contributions in MC results in a better description of the data,

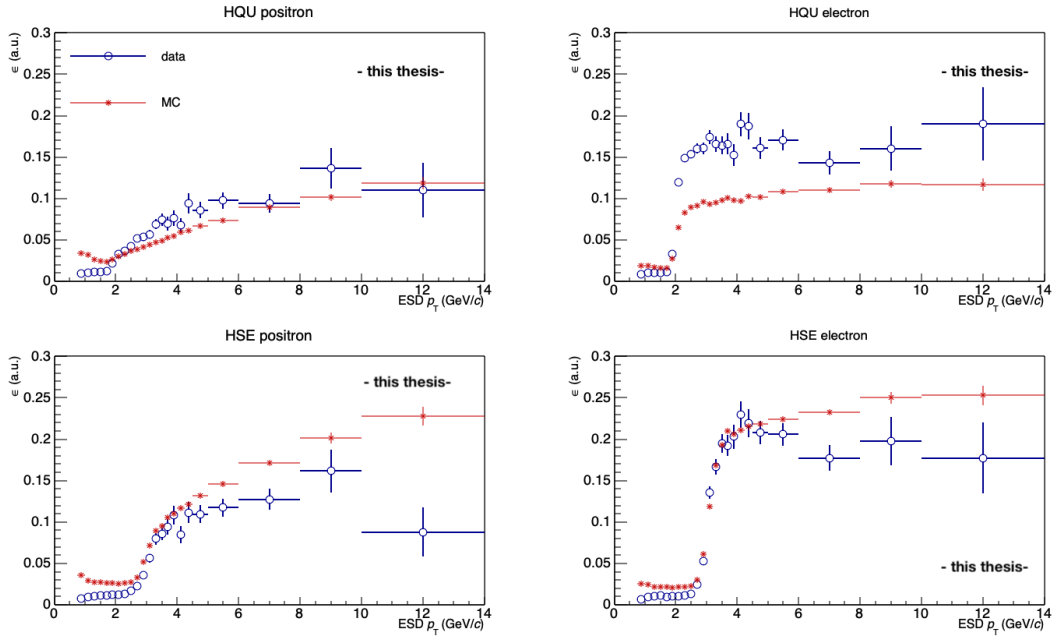

Figure 4.4: TRD trigger efficiency as a function of reconstructed p_{T} in data (open circle, blue) and MC (star, red) applying same electron selection criteria for HQU in top row and HSE in bottom row. Positrons (left column) and electrons (right column) are presented separately.

especially comparing the offset below the p_{T} threshold. In addition, the source of the offset present in trigger efficiency curves both in data and MC got clear, i.e. due to the contribution of underlying events. Although the event was triggered by other particles than an electron, this electron is added into trigger efficiency calculation under the definition in Equation 4.1. If there is no strong correlation between the trigger particle and the electron, the electron spectrum in events triggered by other particles is the same as the one in minimum bias events but scaled by a constant value proportional to the trigger rate, resulting in constant trigger efficiency as a function of p_{T}. Small residual discrepancy between data and MC was improved by optimizing the PID thresholds for the MC that give the same single track trigger efficiency as in the data. Figure 4.8 shows the trigger efficiency in MC simulation with applying different TRD PID thresholds for HSE and HSU separately for electrons, positrons and the contribution of the underlying events (UE). The resulting optimized TRD PID threshold values are summarized in Table 4.2. The origin of the residual discrepancy could be different particle abundances as well as their p_{T} shape in data and MC since the optimized threshold for underlying events differs more to the original value. The MC sample was tagged as TRD triggered events with new optimized threshold and used for calculation of trigger efficiency for J/ψ and extraction of non-prompt J/ψ fraction.

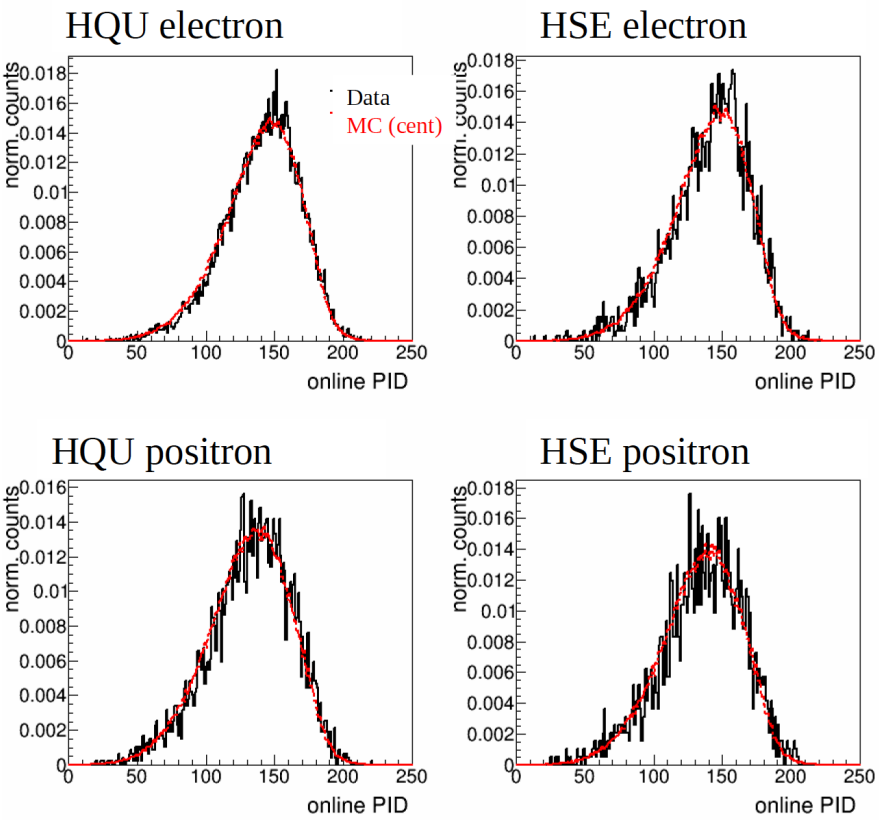

Figure 4.5: Distributions of TRD PID value in data and MC for electrons (top row) and for positrons (bottom row). Plots in left column represent for HQU and in right column for HSE. Electrons (positrons) in $3 < p_{\mathrm{T}} < 10\ \mathrm{GeV}/c$ was selected based on TPC $\mathrm{d}E/\mathrm{d}x$ signal. Figures taken from [205].

trigger and charge	new GTU PID threshold
HQU UE	163
HQU electrons	153
HQU positrons $2 < p_{\mathrm{T}} < 3$ GeV/c	151
HQU positrons $p_{\mathrm{T}} > 3$ GeV/c	154
HSE UE	148
HSE electrons	145
HSE positrons $3 < p_{\mathrm{T}} < 4$ GeV/c	143
HSE positrons $p_{\mathrm{T}} > 4$ GeV/c	146

Table 4.2: Optimized TRD PID threshold values for MC simulations which give the same trigger efficiency in MC as in data. UE refers to underlying events.

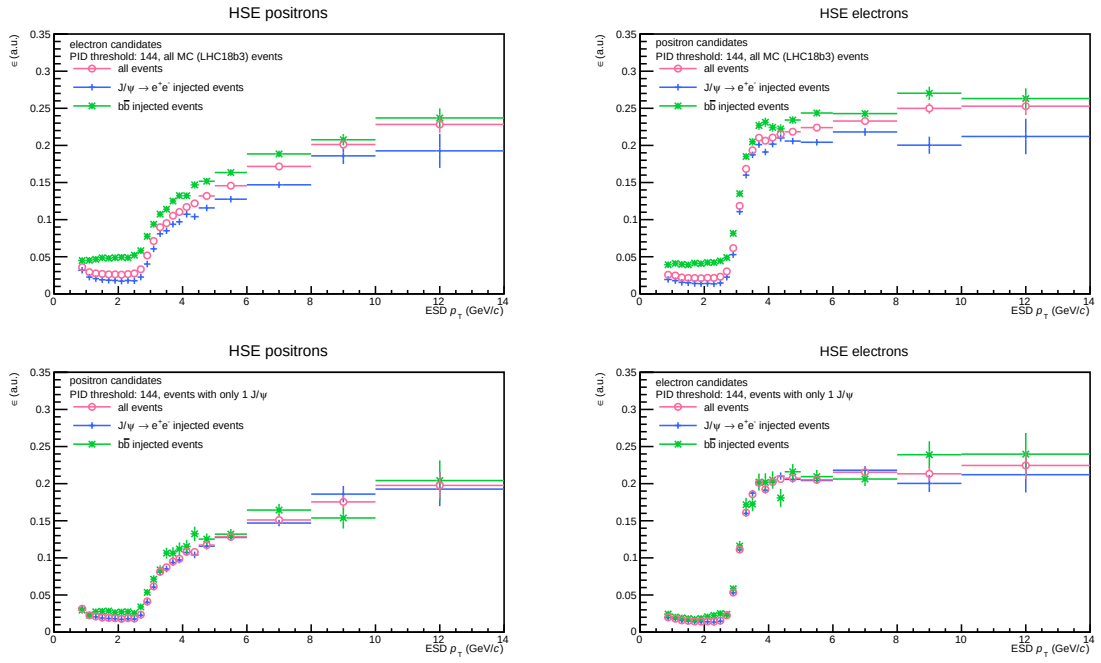

Figure 4.6: TRD trigger (HSE) efficiency as a function of reconstructed p_{T} in MC. Events were split into two subsets, the events with prompt J/ψ and events with beauty quark pair forced to decay to non-prompt J/ψ. Plots in the bottom row present the events having only one J/ψ inside, which is mainly effective for events with beauty quark pair forced to decay to non-prompt J/ψ only as the events with prompt J/ψ mostly carry only one J/ψ inside.

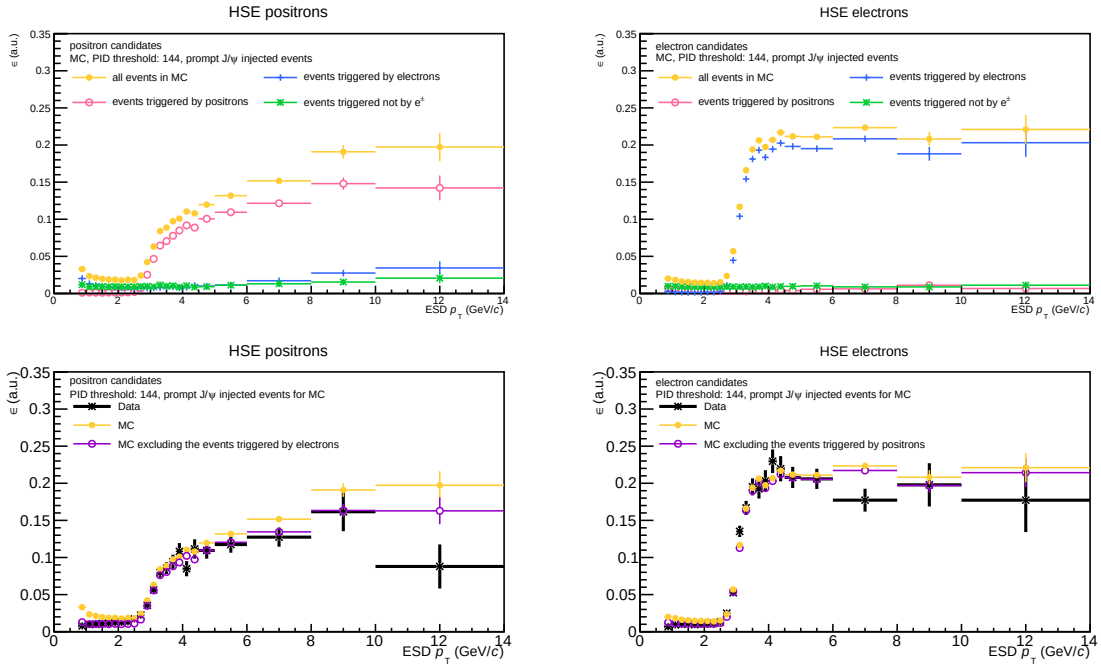

Figure 4.7: TRD trigger (HSE) efficiency as a function of the reconstructed p_{T} for the events with prompt J/ψ in MC. Events were divided into three categories.

Figure 4.8: Trigger efficiency for electrons and positrons for both TRD triggers (HQU and HSE) as a function of reconstructed ESD p_{T}. The black line represents the parameterized trigger efficiency in data and the various coloured lines show the trigger efficiency in MC with different TRD PID thresholds. The plots in the last column show a zoom in to the low p_{T} part, the underlying event contributions.

4.4 Calibration of impact parameter in Monte Carlo simulations

In this thesis work, the fraction of non-prompt J/ψ was obtained hugely relying on the displaced secondary vertex of beauty hadrons in the transverse plane. Therefore, it was important to ensure that the MC simulations realistically reproduce the spatial variables in the data sample. For this purpose, the transverse impact parameter, which is defined as the distance of the closest approach to the primary vertex in transverse plane ($d_{0,r\phi}$), of tracks in data and MC was compared. By its definition, the impact parameter of particles produced at the primary vertex should be 0. Nevertheless, due to the detector effects, including finite and limited resolution of machines and inefficiencies caused by damages could result in make non-zero impact parameters as well as worsen the resolution compared to the designed value. In addition, several effects of particles passing through the matter, such as multiple Coulomb scattering and electron Bremsstrahlung could degrade the resolution of the measured impact parameter as a function of $\beta\gamma$, resulting in a p_{T} dependence. Besides, the contribution of secondary particles also affects on the shape of the impact parameter distributions. The different abundance of the contribution of secondary particles in data and MC makes more complicated to disentangle multiple effects presented in the impact parameter distributions.

For a quantitative study, a sum of a Gaussian function, which is for describing the contributions of primary particles, and an exponential function, for the secondary particles populating the tails of the distributions, were introduced to parameterize the impact parameter distributions as presented in Equation 4.3 with four free parameters (p_i):

$$f(d_{0,r\phi}) = \frac{p_0}{\sqrt{2\pi}p_1} e^{-\frac{(d_{0,r\phi}-p_2)^2}{2p_1^2}} + \frac{1-p_0}{2p_3} e^{-\frac{|d_{0,r\phi}-p_2|}{p_3}}. \tag{4.3}$$

Since the quality of tracking, as well as the contribution of secondary particle, is highly dependent on a presence of hits in the SPD layers, the parameterization was performed for each possible SPD hit configuration of tracks, hits in both SPD layers, single hit only in the first layer and single hit only in the second layer. Figure 4.9 shows the resulting mean and width of the impact parameter distribution in data and MC as a function of p_{T}. In the MC, instead of all charged particles, only primary pions and electrons from prompt J/ψ were selected to study possible particle species differences in the impact parameter distributions. In order to suppress the effect from different p_{T} shapes, the parameterization was performed in small p_{T} ranges as indicated by points on the plots. As the charged hadrons in the data are dominated by the pions, there is no difference observed for charged hadrons and identified pions in data both for mean and resolution (width). On the other hand, a shift of the mean from zero is visible both in data and MC, but the deviation is shown in opposite direction and with different magnitude. Meanwhile, better (smaller) resolution of the impact parameters, the width of parameterziation, was observed in MC with respect to the data. Moreover, the resolution of primary pions clearly shows smaller values than the resolution of electrons from prompt J/ψ. Figure 4.10 shows the impact parameter distributions of electrons from prompt J/ψ for different p_{T} ranges. Subset of electrons, which are contributing close to J/ψ peak in the invariant mass distribution after pairing as J/ψ candidates,

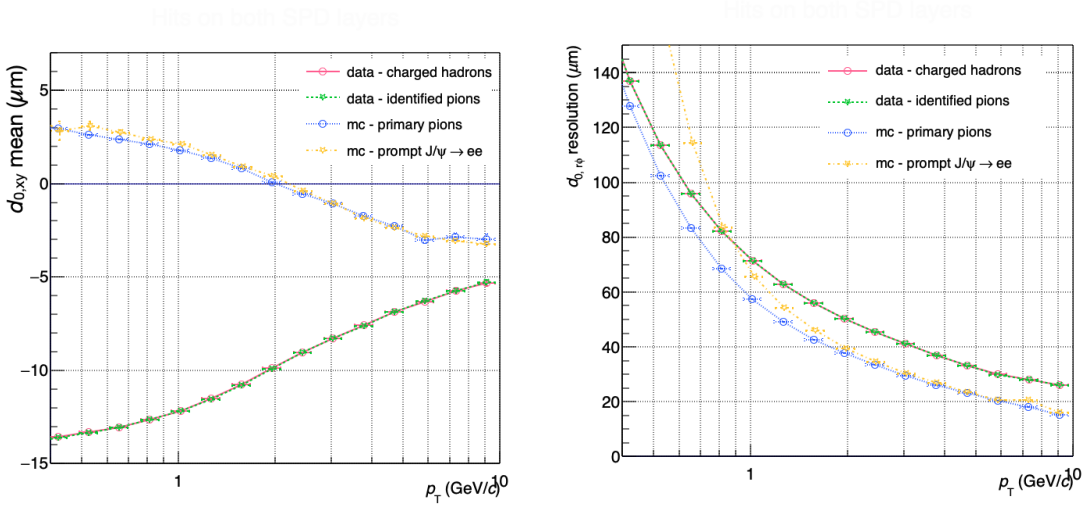

Figure 4.9: Mean (left) and resolution (right) of parameterized impact parameter distributions in data and MC as a function of p_{T} for the tracks having hits in the both SPD layers. For pion identification in data, the TPC $\mathrm{d}E/\mathrm{d}x$ signal was used. Primary pions in MC refers the pions directly from primary vertex of events or from strong decay of primary particles.

shows narrower width of the distributions indicating the energy loss mechanisms of electrons traverse the matter play role to broaden the impact parameter distributions which has clear particle species dependence.

Electrons from Dalitz decays of π^0 mesons were considered for further investigation as these could be used to identify primary electrons in data with high purity without introducing tight selection criteria which influence the impact parameters. The main background of invariant mass reconstructed with electron-positron pair for Dalitz decays of π^0 is the pair from photon conversion. A large fraction of the contribution from the conversion could be rejected using its characteristics, the small opening angle [212, 213]. The resulting mean and width of impact parameter distributions for electrons from Dalitz decays of π^0 in data and MC as a function of p_{T} is presented in Figure 4.11. The difference of width between data and MC is similar in magnitude as the difference shown in 4.9. Nevertheless, more quantitative studies could not be carried out, especially estimating the purity of the electrons in the results due to the lack of statistics.

Alternatively, the impact parameter of each track in the MC sample was corrected based on the discrepancies of pions in data and MC. The difference between electrons and pions which could be obtained from MC simulations was then propagated as the systematic uncertainty which is discussed in detail in Chapter 5. The shift of the mean ($< d_{0,r\phi}^{\mathrm{MC}} > - < d_{0,r\phi}^{\mathrm{data}} >$) and resolution difference ($\frac{\sigma_{\mathrm{data}}}{\sigma_{\mathrm{MC}}}$) of the impact parameter distributions in MC with respect to data is corrected for each track following as a function of p_{T}:

$$d_{0,r\phi}^{\mathrm{corr}}(p_{\mathrm{T}}) = d_{0,r\phi}^{\mathrm{MC,gen.}}(p_{\mathrm{T}}) + (d_{0,r\phi}^{\mathrm{MC,reco.}}(p_{\mathrm{T}}) - d_{0,r\phi}^{\mathrm{MC,gen.}}(p_{\mathrm{T}})) \times \frac{\sigma_{\mathrm{data}}(p_{\mathrm{T}})}{\sigma_{\mathrm{MC}}(p_{\mathrm{T}})} + < d_{0,r\phi}^{\mathrm{MC}} > (p_{\mathrm{T}}) - < d_{0,r\phi}^{\mathrm{data}} > (p_{\mathrm{T}}). \tag{4.4}$$

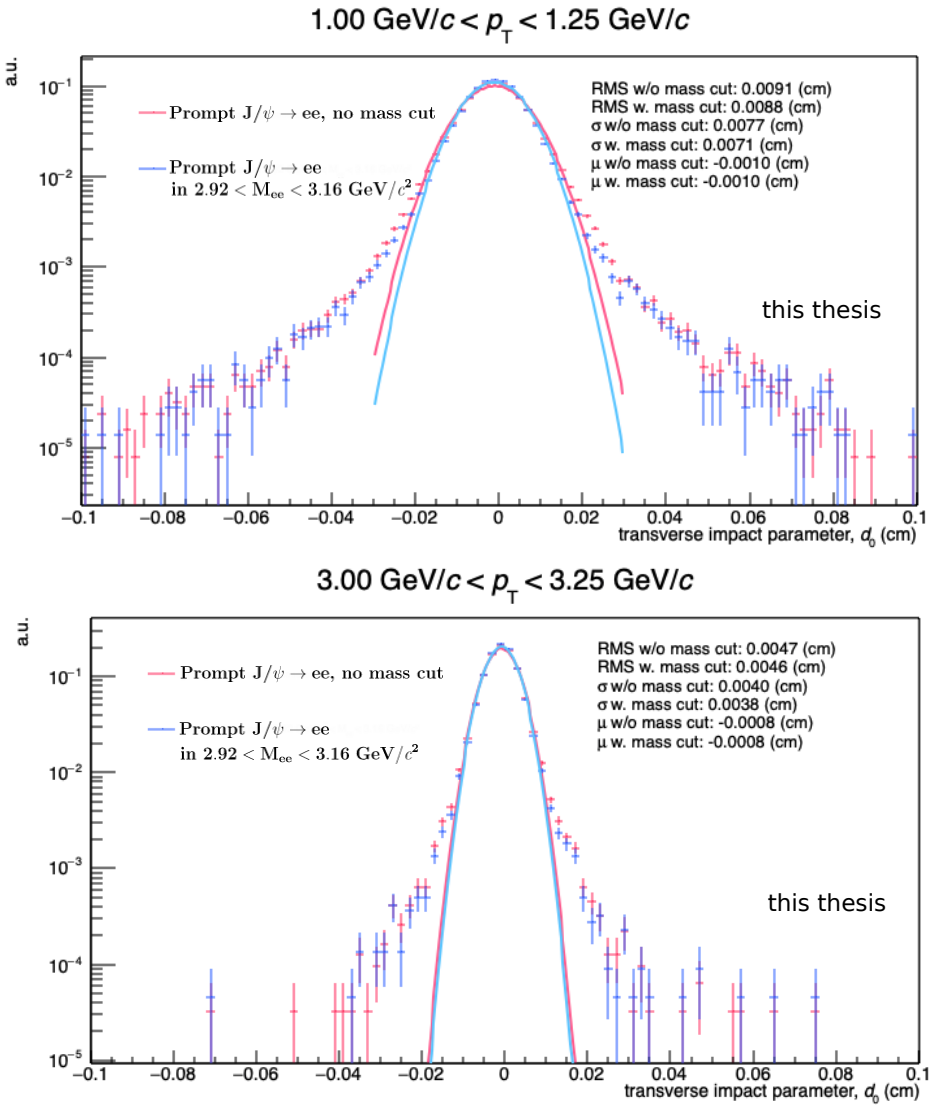

Figure 4.10: Impact parameter distributions of electrons from prompt J/ψ in MC for different p_T ranges. The electrons contributing to the invariant mass region close to the J/ψ peak (blue points) was separately drawn with the electrons in full range (pink points) for the comparison to see the effect of the energy loss mechanisms of electrons traversing the matter, such as multiple Coulomb scattering and Bremsstrahlung. Solid lines around the peak represent gaussian fit results for each distribution.

It was confirmed that the correction factors, $(< d^{MC}_{0,r\phi} > - < d^{data}_{0,r\phi} >)$ and $\frac{\sigma_{data}}{\sigma_{MC}}$ as a function of p_T have no dependence on data taking periods (p–Pb or Pb–p) and TPC conditions during data taking (some data was taken and reconstructed with partially working TPC) separately in data and MC as illustrated in the first and middle row of Figure 4.12. On the other hand, the resolution of the impact parameters showed a clear dependence on the azimuthal angle of tracks in both data and MC but in differently as presented in the last row of Figure 4.12 thus, the correction had to be made accordingly. Figure 4.13 show the mean and the resolution of impact parameter distributions respectively for data and MC sample as a function of p_T for tracks having hits in the both SPD layers. The correction following Equation 4.4 made the MC sample mimicking the data for both the mean and the resolution

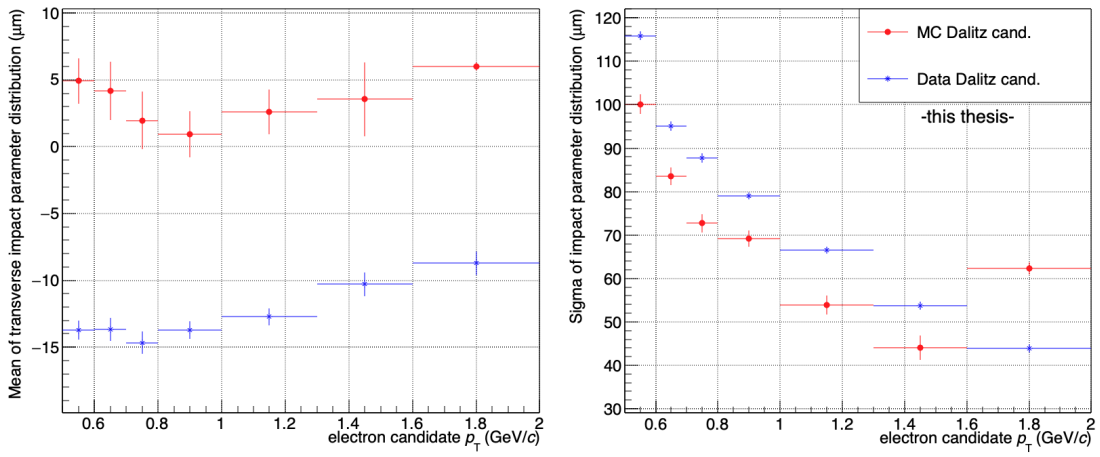

Figure 4.11: Mean and width of impact parameter distributions for electrons from Dalitz decays of π^0 in data and MC as a function of p_{T}.

of impact parameter. Impact of the correction on the pseudo-proper decay-length is presented in Figure 4.14, clearly broadening the distributions of the pseudo-proper decay-length distribution of prompt J/ψ (resolution function). The corrected MC sample was used not only for extracting the resolution function itself, but for obtaining all the pseudo-proper decay-length distributions used for this analysis.

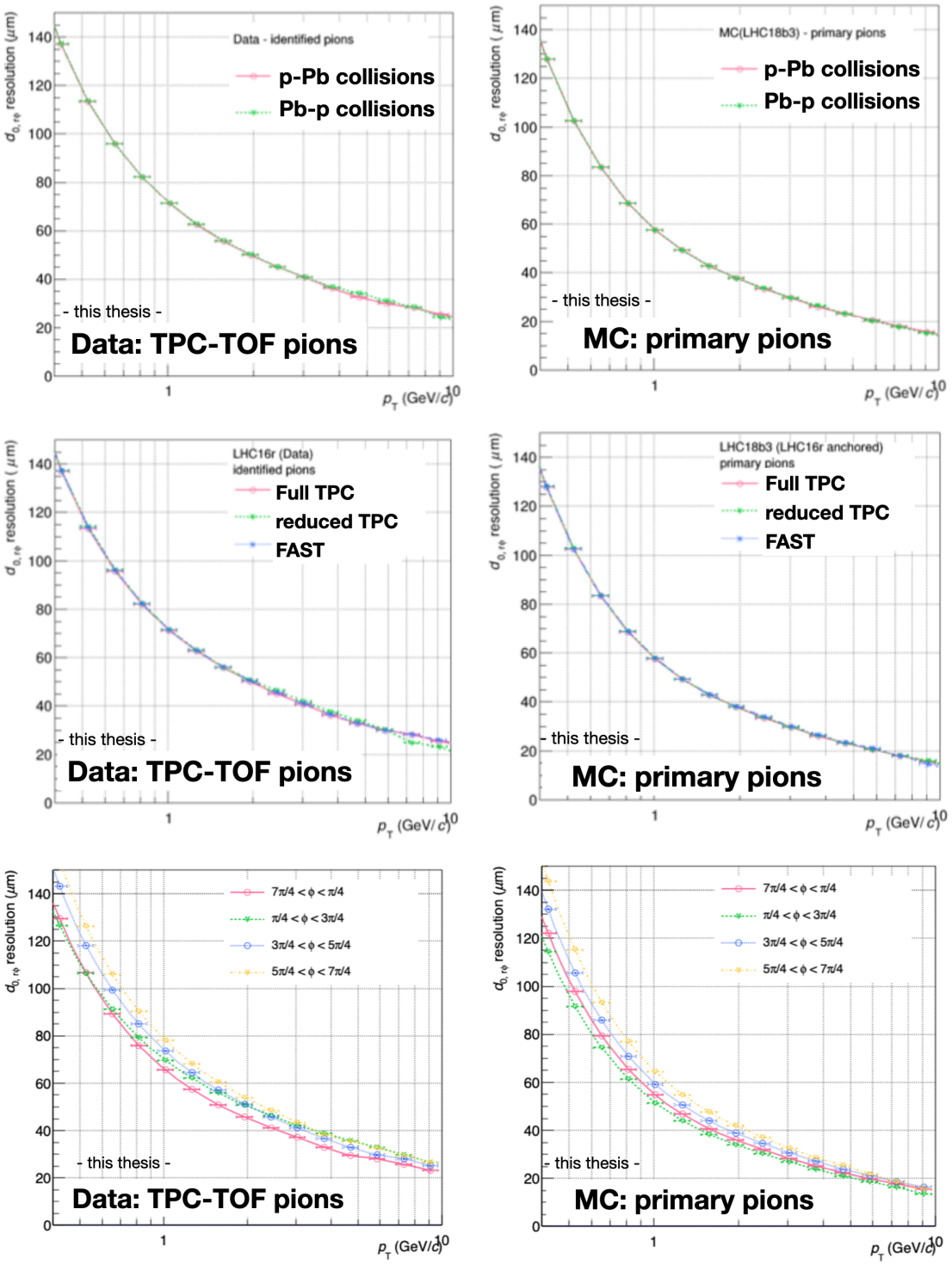

Figure 4.12: Resolution of transverse impact parameter distributions for the identified pions (using TPC and TOF signal) in data (left column) and for primary pions in the MC sample (right column) as a function of p_{T}. Plots on the first row show the resolution vs. p_{T} for each data taking period (p–Pb or Pb–p). Plots on the middle row show the resolution vs. p_{T} for data collected or reconstructed in different TPC conditions. Plots on the last row show the azimuthal angle dependent resolution of transverse impact parameter.

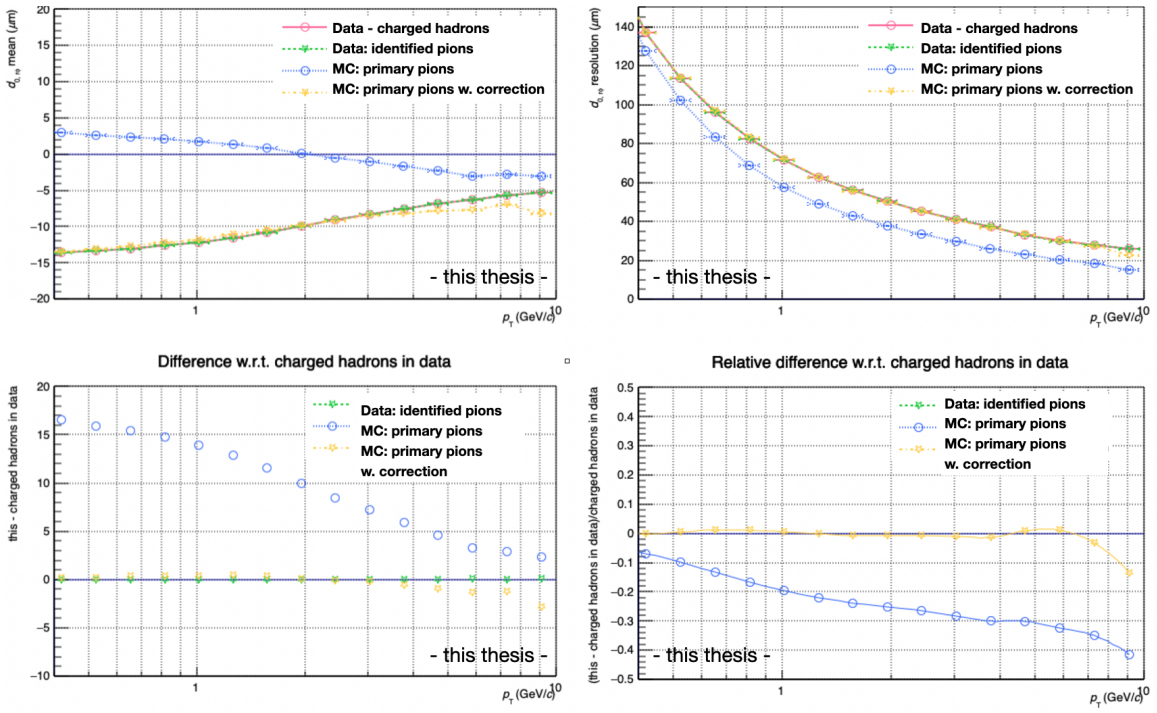

Figure 4.13: Mean (left column) and width (right column) of impact parameter distributions as a function of p_{T} for data and MC. The tracks with hits in the both SPD layers were used. Bottom panels are the relative difference of each distributions with respect to the charged hadrons in data.

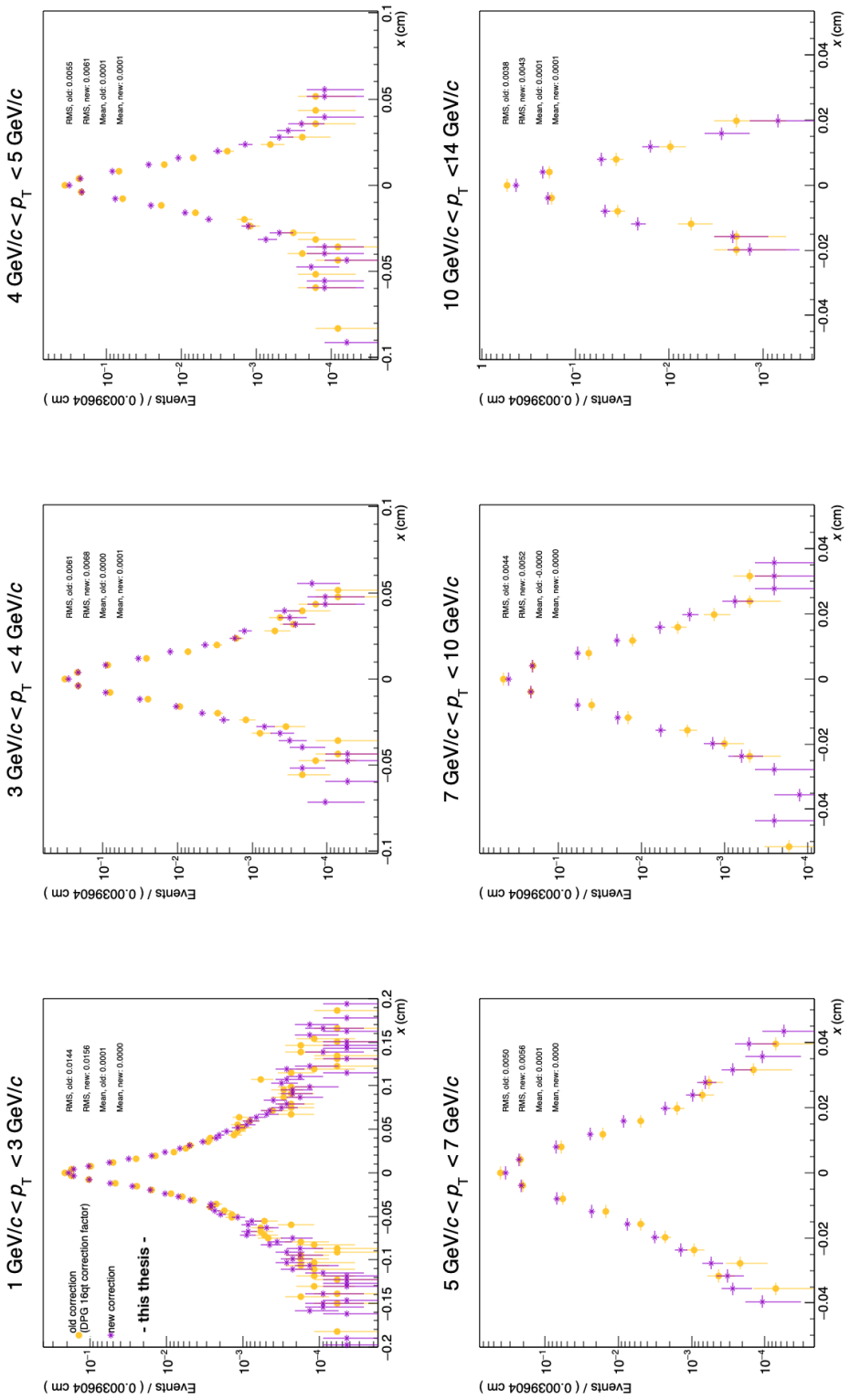

Figure 4.14: Pseudo-proper decay-length distributions of prompt J/ψ (resolution function) for different prompt J/ψ p_T ranges obtained with two different correction factors. The difference between old and new correction factors is about 10% for the impact parameter resolution. Widths of the resulting resolution functions show the difference, about 10%.

5 Measurement of non-prompt J/ψ fraction

The main observable of this thesis work is the fraction of non-prompt J/ψ among inclusive J/ψ production. The di-electron decay mode of J/ψ, which has the branching fraction of $5.971 \pm 0.032\%$ [15], was used for the reconstruction. The kinematic properties of the reconstructed electron and positron were propagated to reconstruct a pair, a J/ψ candidate. The reconstructed invariant mass ($m_{e^+e^-}$) and the pseudo-proper decay-length (x) of J/ψ candidates were used to statistically distinguish prompt J/ψ and non-prompt J/ψ.

While the invariant mass ($m_{e^+e^-}$) of the pairs composed of e^+ and e^- has strong separation power between inclusive J/ψ meson and background, the pseudo-proper decay-length (x) provides the further discrimination between prompt J/ψ and non-prompt J/ψ. The large $c\tau \approx 0.5 \times 10^{-3}$m of non-prompt J/ψ inherited from beauty-flavoured hadron leads the non-prompt J/ψ having longer decay length ($\vec{L}$), which is defined as the pointing vector between the primary vertex and the reconstructed J/ψ decay vertex. In addition, the projection of the decay length on J/ψ transverse momentum and assign a sign,

$$L_{xy}^{\mathrm{J}/\psi} = \vec{L} \cdot \frac{\vec{p}_{\mathrm{T}}^{\,\mathrm{J}/\psi}}{|\vec{p}_{\mathrm{T}}^{\,\mathrm{J}/\psi}|} \tag{5.1}$$

brings additional rejection power. As the non-prompt J/ψ and beauty hadron is strongly correlated based on the decay kinematics, non-prompt J/ψ tends to travel collinearly along the decay length vector ($\vec{L}$), resulting in positive $L_{xy}^{\mathrm{J}/\psi}$. In order to reduce the dependence on the J/ψ transverse momentum in the signed transverse decay length, the pseudo-proper decay-length (x) is used in this analysis defined as follows:

$$x = L_{xy}^{\mathrm{J}/\psi} \times \frac{M^{\mathrm{J}/\psi}}{p_{\mathrm{T}}^{\mathrm{J}/\psi}}, \tag{5.2}$$

where the $M_{\mathrm{J}/\psi}$ is the known mass of J/ψ meson [214]. The variable was named based on its connection to the proper decay length of the beauty hadron, which is expressed in

$$c\tau = \frac{L}{\beta\gamma} = L_{xy}^{\mathrm{B\ hadron}} \times \frac{M^{\mathrm{B\ hadron}}}{p_{\mathrm{T}}^{\mathrm{B\ hadron}}}. \tag{5.3}$$

Most of the contents in this chapter were taken from the ALICE internal notes which I contributed [205, 215]

5.1 Reconstruction of J/ψ candidate pair

The J/ψ candidates were reconstructed with electron and positron candidates fulfilling the selection criteria listed in Table 5.1.

category	selection criteria	note
kinematic acceptance	$p_{\mathrm{T,e}} > 1$ GeV/c $-0.84 < \eta_e < 0.84$	based on TRD acceptance
track quality	Reject kink ITS and TPC refit $70 < N_{\mathrm{TPC,\ cluster}} < 160$ $0 < \chi^2/N_{\mathrm{ITS,\ cluster}} < 36$ $0 < \chi^2/N_{\mathrm{TPC,\ cluster}} < 4$ $-1.0\ \mathrm{cm} < \mathrm{DCA_{XY}} < 1.0\ \mathrm{cm}$ $-3.0\ \mathrm{cm} < \mathrm{DCA_{Z}} < 3.0\ \mathrm{cm}$ At least one hit in one of two SPD layers	additional requirement applied for pairing
electron identification	$-3.0 < \mathrm{TPC\ n}_{\sigma_{\mathrm{e}}} < 3.0$ $3.5 < \mathrm{TPC\ n}_{\sigma_{\mathrm{proton}}}$ $3.5 < \mathrm{TPC\ n}_{\sigma_{\pi}}$	

Table 5.1: List of track selection criteria required in this analysis. See the text for the detailed description.

Only tracks having p_{T} larger than 1 GeV/c were used in this analysis, where to guarantee good tracking and particle identification performance. The range of η was required to be between -0.84 and 0.84 to avoid edge effects in the TRD. To ensure having reconstructed tracks with good quality, several requirements on track properties were applied. Restrictions on the track distance of the closest approach (DCA) in transverse plane and z-axis were introduced to remove secondary particles produced by decays of long-lived particles such as K^0_s and Λ and electrons from photon conversion in the detector material.

As the signal extraction in this analysis strongly relied on the geometrical observable, the pseudo-proper decay-length, it was crucial to select the tracks with good spatial resolution. For this purpose, at least 1 hit in either of two layers of the SPD, the innermost silicon detector, was required for all tracks. In other words, tracks having hits in both layers, hit in the first layer only or hit in the second layer only could be used for reconstructing J/ψ candidates. With this requirements, there are six possible combinations of pairs depending on SPD hits of daughter tracks. For instance, the pairs with both daughter tracks having hits in both SPD layers, with one daughter track having hit in the first layer and the other having hit in the second layer and so on. Figure 5.1 shows the number of J/ψ candidates for each combinations in the data sample. Except for the pairs with both daughter tracks having hits in both SPD layers and with one daughter track having hits in both layer and the other having hit in the second layer, the absolute number of J/ψ candidates from the other combinations is small and their contribution around the J/ψ invariant mass region is not significant. Similar qualitative estimation was repeated with changing p_{T} range of J/ψ candidates. The resulting trend was found to be almost p_{T}

independent in the data sample used for this analysis. Thus, only pairs reconstructed with both tracks with hits in both SPD layers and one track with hits in both SPD layers and the other having a hit in the second layer were used for further analysis, the signal extraction.

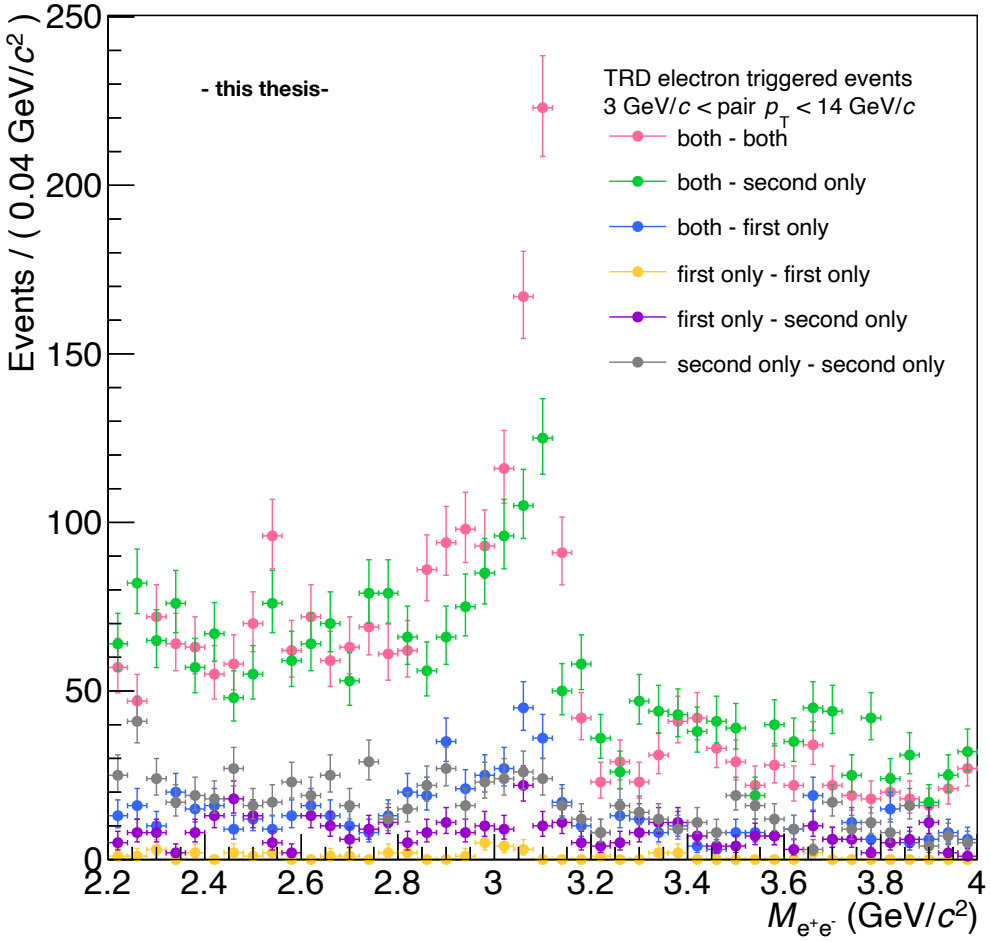

Figure 5.1: Invariant mass distribution of J/ψ candidates in $3 < p_{\mathrm{T}} < 14$ GeV/c in the TRD-triggered events, categorized according to the SPD hit configuration of the daughter tracks. Both-both (shown in pink) refers to pairs reconstructed with both daughters (an electron and a positron) having hits in both SPD layers. Both-second only (shown in green) represents the pairs reconstructed with one daughter (either an electron or a positron) with hits in both SPD layers and the other daughter having a hit only in the second SPD layer. The others are defined in an analogous way.

The electron identification was performed using the TPC signal, the specific energy loss of the ionization in the TPC gas. Figure 5.2 shows the TPC n_{σ_e} distribution as a function of p_{T} in data (left) and MC (right) for tracks fulfilling PID the requirements used in this analysis. The PID performance in data is qualitatively well reproduced in MC, showing no visible remaining hadron contamination. In addition, the mean and the width of the TPC n_{σ_e} distribution projected in small momentum ranges are the same in data and MC and thus the PID efficiency could be directly extracted from the MC without further correction on the MC simulations.

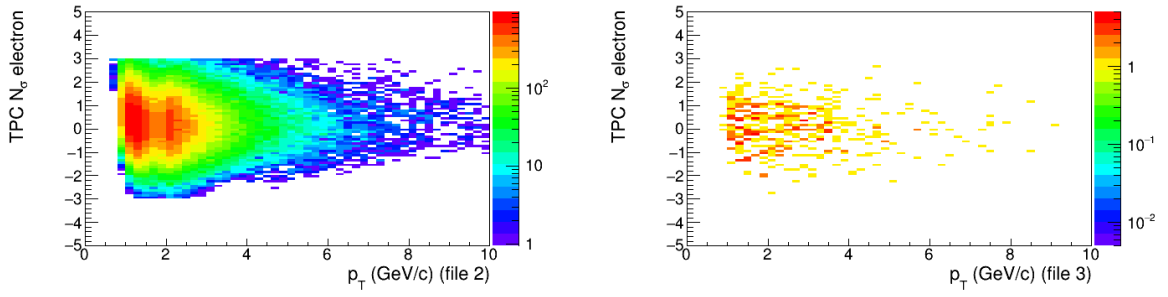

Figure 5.2: TPC n_{σ_e} as a function of p_T in data (left) and MC (right) for tracks fulfilling PID requirements listed in Table 5.1 from TRD-electron triggered events.

5.2 Extraction of non-prompt J/ψ fraction

The main observable of this analysis is the fraction of non-prompt J/ψ with respect to inclusive J/ψ f_B. $f_B = \frac{N_{h_B \to J/\psi}}{N_{\text{inclusive } J/\psi}}$ It is estimated on a statistical basis. The pairs satisfying the aforementioned selection criteria consist of prompt J/ψ, non-prompt J/ψ and background. The fraction of non-prompt J/ψ is obtained by using a two-dimensional extended unbinned likelihood fit of the invariant mass ($m_{e^+e^-}$) and the pseudo-proper decay-length (x), with the following likelihood function $F(x, m_{e^+e^-})$:

$$F(x, m_{e^+e^-}) = c_{\text{prompt } J/\psi} \cdot P_{\text{prompt } J/\psi}(m_{e^+e^-}, x) + c_{h_B \to J/\psi} \cdot P_{h_B \to J/\psi}(m_{e^+e^-}, x) + c_{\text{bkg.}} \cdot P_{\text{bkg.}}(m_{e^+e^-}, x) \tag{5.4}$$

where indices i stand for the particle species, prompt J/ψ, non-prompt J/ψ and background (bkg.), c_i is the fraction of the particle species i, and $P_i(m_{e^+e^-}, x)$ represents the two-dimensional probability density function (PDF) of each components i defined as a function of $m_{e^+e^-}$ and x. Assuming that there is no strong correlation between the invariant mass and the pseudo-proper decay-length, $P_i(m_{e^+e^-}, x)$ can be expressed as the product of the probability density distribution in $m_{e^+e^-}$ (M_i) and the probability density distribution in x (X_i). Since the decay kinematics of J/ψ into di-electrons are identical for prompt and non-prompt J/ψ, Equation 5.4 can be written as follows:

$$\begin{aligned} F(x, m_{e^+e^-}) = f_{J/\psi} \cdot M_{J/\psi}(m_{e^+e^-}) \cdot \left[f'_B \cdot X_{h_B \to J/\psi}(x) + (1 - f'_B) \cdot X_{\text{prompt } J/\psi}(x) \right] \\ + \left(1 - f_{J/\psi}\right) \cdot X_{\text{bkg}}(x) \cdot M_{\text{bkg}}(m_{e^+e^-}) \end{aligned} \tag{5.5}$$

where $f_{J/\psi}$ represents the inclusive J/ψ fraction of pair candidates and f'_B is the non-prompt J/ψ fraction of inclusive J/ψ. In total, five probability density functions of each components in $m_{e^+e^-}$ ($M_{J/\psi}$, M_{bkg}) and x ($X_{\text{prompt } J/\psi}$, $X_{h_B \to J/\psi}$, X_{bkg}) were required for the two-dimensional likelihood fit as illustrated in Figure 5.3, which shows the maximum likelihood fit projected over the invariant mass and pseudo-proper decay length distributions of J/ψ candidates in $4 < p_T < 5$ GeV/c from the data sample. It should be noted that f'_B, the non-prompt J/ψ fraction of inclusive J/ψ obtained from the fit, includes the effects of geometrical acceptance and inefficiencies from requiring the aforementioned selection criteria. The final non-prompt J/ψ fraction, f_B, was then obtained by applying the correction factor described in Section 5.3. Based on the likelihood function in Equation 5.5, an unbinned extended

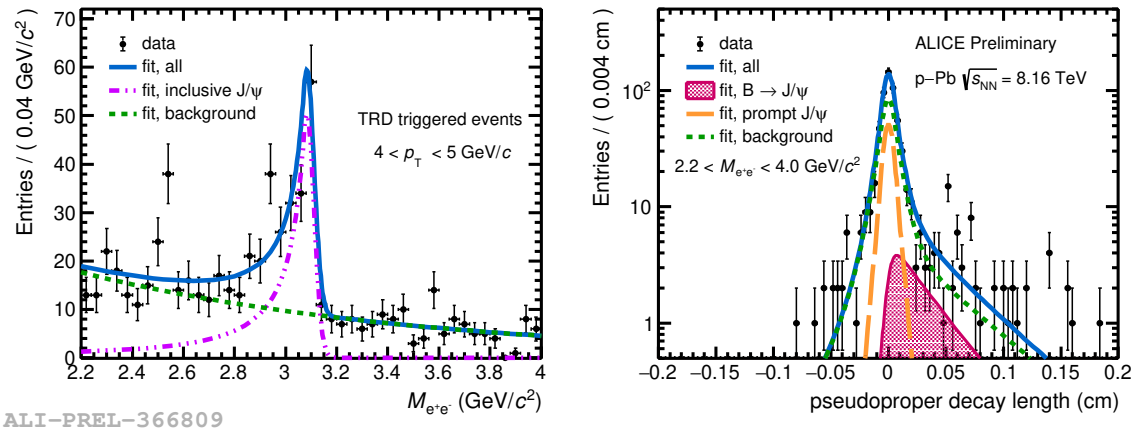

Figure 5.3: Maximum likelihood fit projected over the invariant mass (left) and pseudo-proper decay length (right) distributions of J/ψ candidates in $4 < p_{\mathrm{T}} < 5$ GeV/c from the data sample.

maximum likelihood fit was performed to obtain f'_B by maximizing

$$\ln \mathcal{L} = \sum_{i=1}^{N} \ln F(x^i, m^i_{e^+e^-}) - N, \tag{5.6}$$

where the N is the number of J/ψ candidates in the data sample. Details on the five PDFs used for constructing the likelihood function are described in following sub-sections.

5.2.1 Signal invariant mass distribution

The invariant mass distribution of the inclusive J/ψ ($M_{\mathrm{J}/\psi}$) described in Equation 5.5 was evaluated based on the MC simulation. First, the invariant mass distribution of $\mathrm{e^+e^-}$ were obtained from reconstructed tracks of electrons and positrons decayed from the MC truth inclusive J/ψ. In order to suppress possible fluctuation due to the statistical limitation, a functional form known as "Crystal Ball function" [216] was introduced as follows,

$$f(m; m_0, \sigma, \alpha, n) = \begin{cases} \exp\left(-\frac{1}{2} \cdot \left[\frac{m-m_0}{\sigma}\right]^2\right), & \text{for } \left|\frac{m-m_0}{\sigma}\right| < |\alpha| \\ A \cdot (B + \left|\frac{m-m_0}{\sigma}\right|)^{-n}, & \text{for } \left|\frac{m-m_0}{\sigma}\right| \geq |\alpha|, \end{cases} \tag{5.7}$$

where

$$\begin{aligned} A &= \left(\frac{n}{|\alpha|}\right)^n \cdot \exp\left(-\frac{|\alpha|^2}{2}\right), \\ B &= \frac{n}{|\alpha|} - |\alpha|\,. \end{aligned} \tag{5.8}$$

The function consists of two terms, Gaussian function with width of σ for describing a symmetric resolution smearing along the J/ψ mass peak around m_0, and additional exponential term which effectively works in the left tail of the distribution, outside certain cut value α for the internal Bremsstrahlung effect

on the left side tail. The left of Figure 5.4 shows an example of the parameterization for J/ψ in momentum interval $4 < p_{\mathrm{T}} < 6\ \mathrm{GeV}/c$. Four free parameters, m_0, σ, n and α were determined for each p_{T} interval as presented in the right of Figure 5.4. The width of the resolution, which can be seen in the right tail of the distributions, tends to get larger for higher p_{T} as the momentum resolution of the tracks increases as a function of p_{T}.

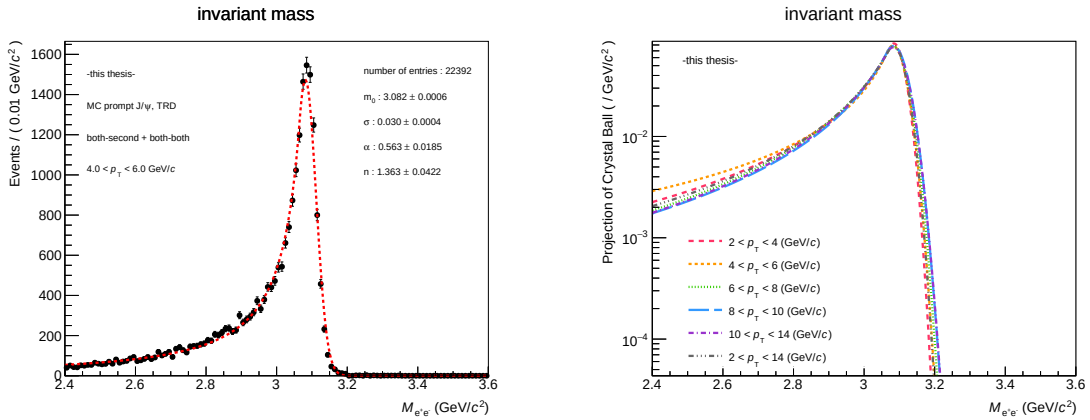

Figure 5.4: (Left) Invariant mass distribution of prompt J/ψ in MC sample. The same track and pair selection criteria were required as for the data. Line indicates the parameterized distribution with Crystal Ball function for the signal extraction. (Right) Parameterized invariant mass distributions of J/ψ for each p_{T} interval studied in this analysis.

A similar parameterization was also performed for the data as illustrated in Figure 5.5. The invariant

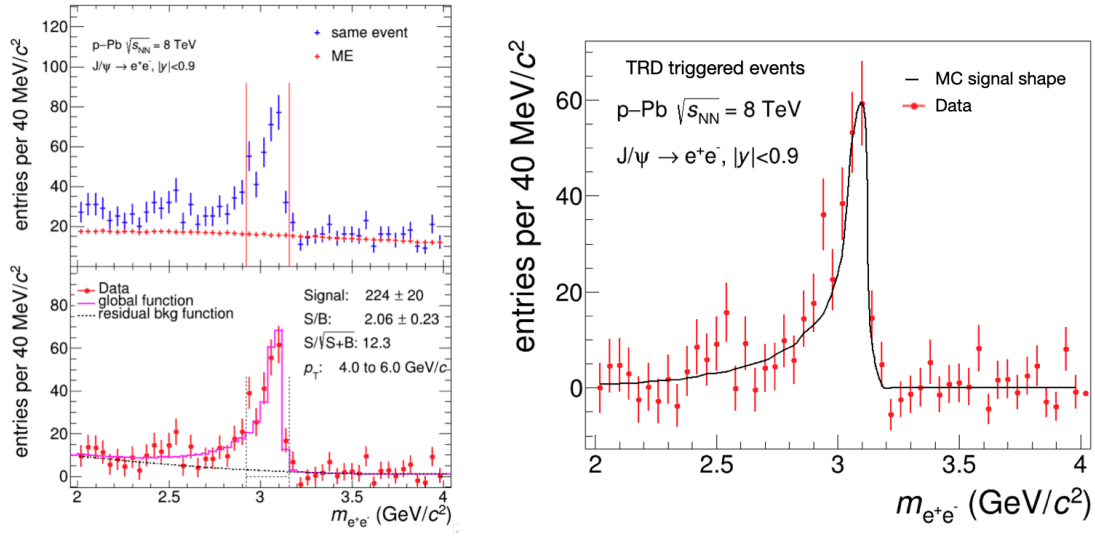

Figure 5.5: (Left) Invariant mass distribution of electron-positron candidates in data for pairs $4 < p_{\mathrm{T}} < 6\ \mathrm{GeV}/c$. The uncorrelated background was estimated by event mixing technique and subtracted. Residual background was described by second order polynomial function, presented as a dashed line. (Right) Background subtracted invariant mass distribution together with J/ψ signal shape from the MC simulation.

mass distribution of electron-positron candidates in data consists of signal (inclusive J/ψ), combinatorial background and correlated background. The uncorrelated background component was estimated

by the event mixing technique, pairing daughter tracks from different events which are fully uncorrelated. After subtracting the uncorrelated background component, the residual (correlated) background was parameterized with a functional form, resulting in the signal as shown in the left panel of Figure 5.5, and subtracted. The resulting signal distribution in data is well described by the MC signal shape shown in the right panel of Figure 5.5, proving that the above described parameterization of Crystal Ball function from the MC sample is reliable to apply for the data sample. The parameterization defined in Equation 5.7 was also performed for the signal distribution in data for each p_{T} interval and compared with those in MC sample as shown in Figure 5.6. In should be noted that the fit result from the experimental data is not for the signal extraction due to the limited of statistics and less knowledge of the residual background. Thus, the uncertainty of the parameterized distributions in data was not estimated in this study and the parameterized distributions in data were only used for the comparison with those from the MC sample, not directly for the signal extraction. Further, the MC sample was split into the QED radiative decays, with an additional photon as a decay product, and non-radiative decays of J/ψ. While the resolution effect along the J/ψ invariant mass peak is predominantly determined by the detector geometry which can be precisely described in the MC simulation, the internal Bremsstrahlung process affecting on the tail of the distribution is more difficult to be simulated. Consequently, the invariant mass distributions of radiative decays and non-radiative decays of J/ψ were taken to investigate the impact of the energy loss on the distributions. In other words, J/ψ experiencing the internal Bremsstrahlung process was probed by radiative decays of J/ψ. As shown in Figure 5.6, parameterized invariant mass distributions in data and MC are compatible with each other, especially agree within the extreme variations of the distributions obtained from purely radiative J/ψ decays and non-radiative J/ψ decays. From this study, the parameterized invariant mass distributions of radiative decays and non-radiative decays of J/ψ in MC were taken as possible extreme variations of the signal shape and used for the estimation of the systematic uncertainty arising from the description for the signal invariant mass distributions.

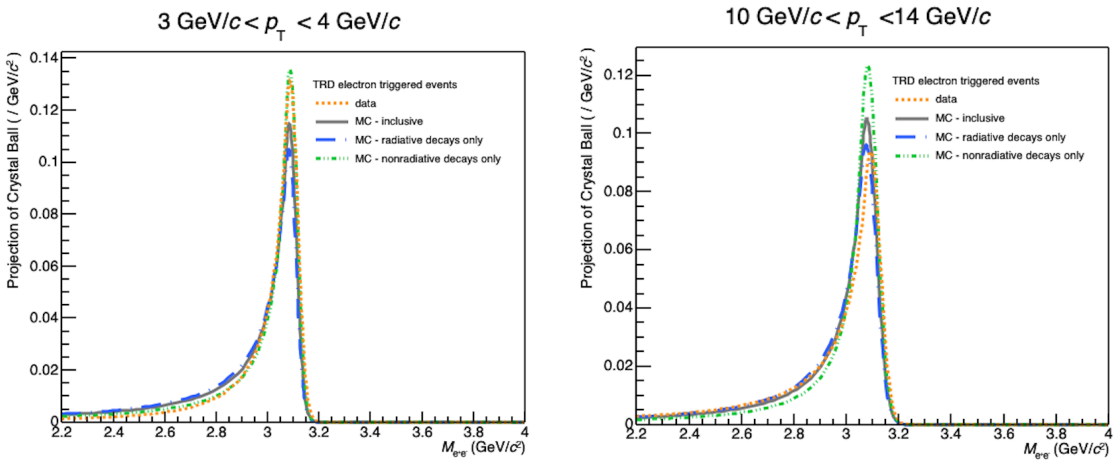

Figure 5.6: Parameterized invariant mass distributions of prompt J/ψ in MC sample for different p_{T} interval, split into radiative and non-radiative decay modes. Parameterized invariant mass distributions in data was obtained by subtracting background using event mixing method described in the text.

5.2.2 Background invariant mass distribution

Once the invariant mass distribution of the $\mathrm{J}/\psi \rightarrow \mathrm{e}^{+}\mathrm{e}^{-}$ candidates is determined, the background component is directly accessible in the invariant mass distribution of pair candidates in data as seen in Figure 5.5. The background PDF of the invariant mass was obtained by fitting the invariant mass distribution of pair candidates in data with the signal invariant mass distribution from MC simulation and a model of functional form. Since the background has contributions from a variety of complex processes without a simple parametric description, modelling based on underlying physics was not applicable in this case. Instead, a simple analytical function which reasonably describes the shape presented in the side-band region, exponential function, was introduced as shown in Figure 5.7, assuming there is no peculiar behavior of the background shape in the range overlapped with signal. In order to estimate the possible bias due to the modelling, the background PDFs were obtained with the first order and the second polynomials, instead of exponential function. The background PDFs obtained from like-sign pairs, i.e. electron-electron and positron-positron pairs were also used for the estimation of systematic uncertainty from the description of background invariant mass distribution.

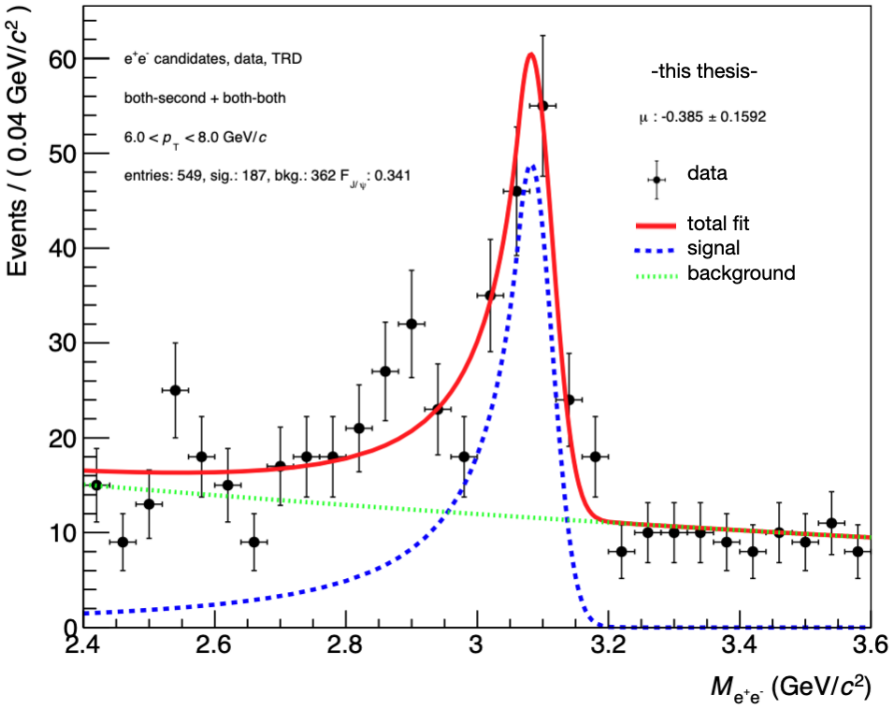

Figure 5.7: Invariant mass distributions of data forp_{T} interval $6 < p_{\mathrm{T}} < 8\ \mathrm{GeV}/c$. The signal ($\mathrm{J}/\psi$) and background component are described by the parameterized distribution from MC discussed in the previous section and an exponential function, respectively.

5.2.3 Prompt J/ψ pseudo-proper decay-length distribution

The J/ψ meson decays to a di-electron pair via the annihilation of the c and $\bar{c}$ quarks with a full width of 92.9 keV [15] and corresponding $c\tau \approx 0.2 \times 10^{-11}$ cm. Consequently, the decay vertex of prompt J/ψ cannot be distinguished from the the primary vertex, resulting in a true pseudo-proper decay length of

essentially 0. The measured pseudo-proper decay length distribution of prompt J/ψ however is affected by the primary vertex and tracking resolution arising from the finite precision of the detector as well as the energy loss of a particle passing through the material, which modifies the momentum and trajectory of a track. This is the reason why the prompt J/ψ pseudo-proper decay-length distribution is also called the resolution function in similar analyses. The pseudo-proper decay-length distribution of prompt J/ψ in the MC sample was described by the functional form first introduced by the CDF collaboration [214] as follows:

$$R(x) = w_1 \cdot G_1(x; \mu_1, \rho_1) + w_2 \cdot G_2(x; \mu_2, \rho_2) + w_3 \cdot f(x; \alpha, \lambda) \tag{5.9}$$

where the w_i are the weights for each contribution i and G_i are Gaussian functions for describing the detector effects smeared into tracking and primary vertex resolutions. The term f is the symmetric power law term for describing the effect originating from the energy loss of track passing through the material, i.e. multiple scattering and Bremsstrahlung:

$$f(m; \alpha, \lambda) = \begin{cases} \frac{\lambda-1}{2\alpha\lambda} & |x| < \alpha \\ \frac{\lambda-1}{2\alpha\lambda} \alpha \, |x|^{-\lambda} & |x| > \alpha, \end{cases} \tag{5.10}$$

where a constant step α was introduced to stabilize the fit and effectively describe the tail of the distribution. Figure 5.8 present the prompt J/ψ pseudo-proper decay-length distributions and parameterized PDFs for p_T interval $2 < p_T < 4\,\mathrm{GeV}/c$ (left) and $10 < p_T < 14\,\mathrm{GeV}/c$ (right) obtained from the impact parameter calibrated MC sample discussed in Chapter 4.4. The exponential tails disappears and the width of the Gaussians becomes narrow for the distribution in the interval $10 < p_T < 14\,\mathrm{GeV}/c$ due to a smaller impact of electron energy loss process and better tracking resolution, respectively at high p_T. As discussed, the resolution effects in data were propagated into MC sample via the calibration.

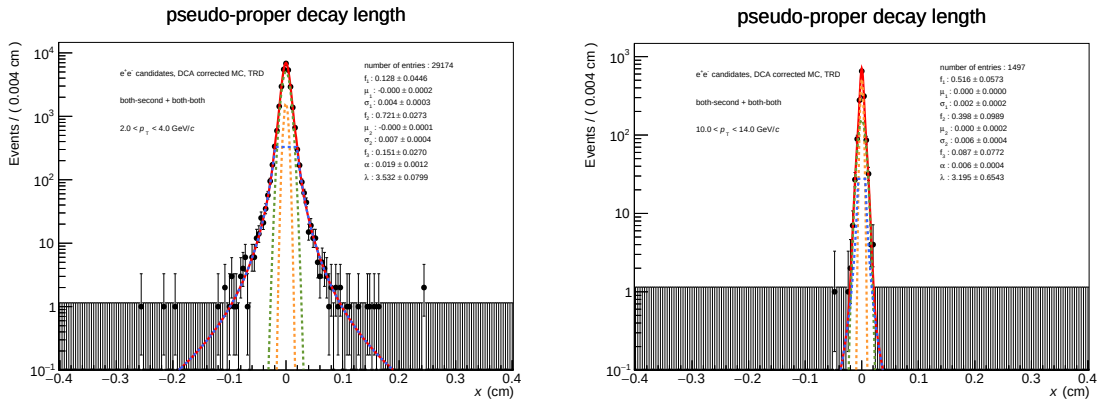

Figure 5.8: Prompt J/ψ pseudo-proper decay-length distributions for the p_T interval $2 < p_T < 4\,\mathrm{GeV}/c$ (left) and $10 < p_T < 14\,\mathrm{GeV}/c$ (right). The data points were obtained from MC simulations, calibrated mimicking the detector response in data as described in Section 4.4. Solid lines show the parameterized functions described in the text.

There is, however, the possible modification due to the energy loss of electrons traversing the detector material, which is shown as the impact parameter resolution difference between electrons from prompt

J/ψ and primary pions in the MC sample (see Figure 4.9). This effect investigated using MC simulations was propagated as part of systematic uncertainty. In order to quantify the impact, two resolution functions for systematic variation were made by worsening the resolution of electrons by the difference in pions and electrons under the assumption that the effect is double as large in data and improving the resolution of electrons to make it similar to the resolution of pions assuming that the effect is not in data.

5.2.4 Non-prompt J/ψ pseudo-proper decay-length distribution

Based on the resolution function described in the previous subsection, the pseudo-proper decay-length distribution of non-prompt J/ψ could be obtained using the kinematic distribution of non-prompt J/ψ from MC ($\mathcal{X}_B(x)$) without the full detector simulation:

$$X_{\mathrm{h_B}\to \mathrm{J}/\psi}(x) = \mathcal{X}_B(x') \otimes R(x - x'), \tag{5.11}$$

the convolution of the $\mathcal{X}_B(x)$ and the resolution $R(x)$ as illustrated in the left panel of Figure 5.9. On the right panel of Figure 5.9, the $X_{\mathrm{h_B}\to \mathrm{J}/\psi}(x)$ is presented for different p_{T} intervals. Due to the wider decay angle between the beauty hadron and the non-prompt J/ψ as well as worse resolution, non negligible contribution is presented in negative x range for low p_{T} intervals.

Equation 5.11 allows the distribution $X_{\mathrm{h_B}\to \mathrm{J}/\psi}(x)$ to be constructed without suffering from statistical limitations of the MC sample by avoiding detector simulation which causes the expensive computation. In addition, this notation allows to disentangle the contributions affecting the shape of the non-prompt J/ψ pseudo-proper decay-length distribution. Therefore, the dependence of non-prompt J/ψ pseudo-proper decay-length could be studied focusing on kinematics of beauty hadrons implemented in the MC sample. The kinematic distribution of non-prompt J/ψ relies on the composition of beauty mesons and baryons with different kinematic distributions and lifetime as well as decay kinematics of beauty hadrons. In order to consider the realistic composition of beauty mesons and baryons with different kinematic distributions, the beauty hadron fractions measured by the LHCb collaboration at forward rapidity ($2 < \eta < 5$) in pp collisions at $\sqrt{s}$ = 13 TeV [217] were considered. While a strong p_{T} dependence was observed in measured Λ_b^0 to $(B^- + B^0)$ ratio, no significant dependence on pseudorapidity was found. The MC simulation was calibrated to match the p_{T} dependent relative fraction of beauty hadrons measured by the LHCb collaboration by a reweighting procedure. In the MC simulation, the decay kinematics of beauty hadrons was governed by the EvtGen, which is dedicated for simulating the decays of heavy flavour particles [209]. In order to estimate the impact of the decay kinematics on the final f_{B}, $\mathcal{X}_B(x)$ was alternatively obtained using PYTHIA [81] decayer instead and the difference in the final result was interpreted as the systematic uncertainty due to the uncertainty in the decay description.

5.2.5 Background pseudo-proper decay-length distribution

The background sources can be divided into three classes based on their origin. First, correlated and uncorrelated background associated with primary particles would contribute as symmetric term around

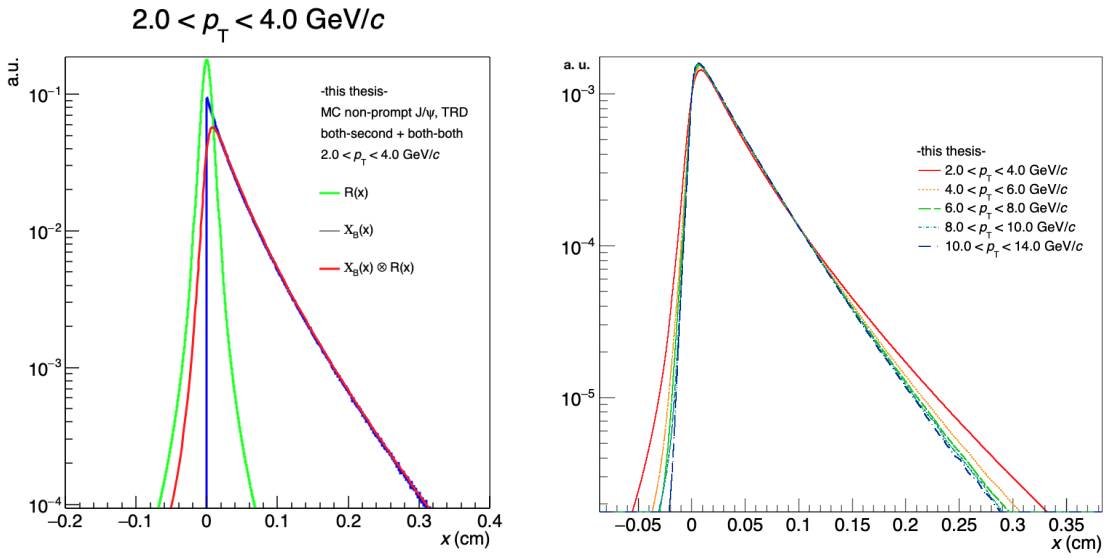

Figure 5.9: (Left) Kinematic distributions of non-prompt J/ψ in MC sample ($\mathcal{X}_B(x)$) for each p_T interval used in this analysis. (Right) Non-prompt J/ψ pseudo-proper decay-length distributions as a result of convolution of the kinematic distribution and the resolution function.

x = 0 because their pseudo-proper decay-length is mainly governed by resolution effects as for prompt J/ψ. Correlated background associated with secondary particles with a long lifetime (i.e. charm and beauty-flavour hadrons) would be similar to non-prompt J/ψ cases having a positive tail in the pseudo-proper decay-length distribution but with a different slope. Lastly, uncorrelated background associated with secondary particles would form both negative and positive tails in the pseudo-proper decay-length distribution. Under this classification, the following functional form was used for parameterization inspired by the model introduced by the CDF collaboration [214]:

$$X_{\mathrm{bkg}}(x) = [\frac{f_+}{\lambda_+}e^{-\frac{x'}{\lambda_+}} \cdot \theta(x') + \frac{f_-}{\lambda_-}e^{\frac{x'}{\lambda_-}} \cdot \theta(-x') + \frac{1-f_+-f_-}{2\lambda_{sym}}e^{\frac{x'}{\lambda_{sym}}}] \otimes R(x-x'), \tag{5.12}$$

where $\theta(x)$ is a step function and $R(x-x')$ is the resolution function. The λ_i in each term indicates a different slope of the exponential function reflecting the various composition of background sources. The corresponding coefficient f_i stands for the weights of each contribution and the sum of f_i is set to 1.

In the right of Figure 5.10, the parameterized background pseudo-proper decay-length distributions are presented for different invariant mass windows were presented, showing discrepancy between each other. The discrepancy reflects the invariant mass dependence of the background composition among three classes defined above. The impact of this discrepancy was not negligible in the signal extraction done via the likelihood fit, thus, the invariant mass dependent pseudo-proper decay-length distribution had to be introduced. As illustrated in the left of Figure 5.10, the background was split into three regions of invariant mass, left side band (LS), right side band (RS) and under signal (US). Unlike the LS and RS regions, where the background could be directly accessed from data, the US region could

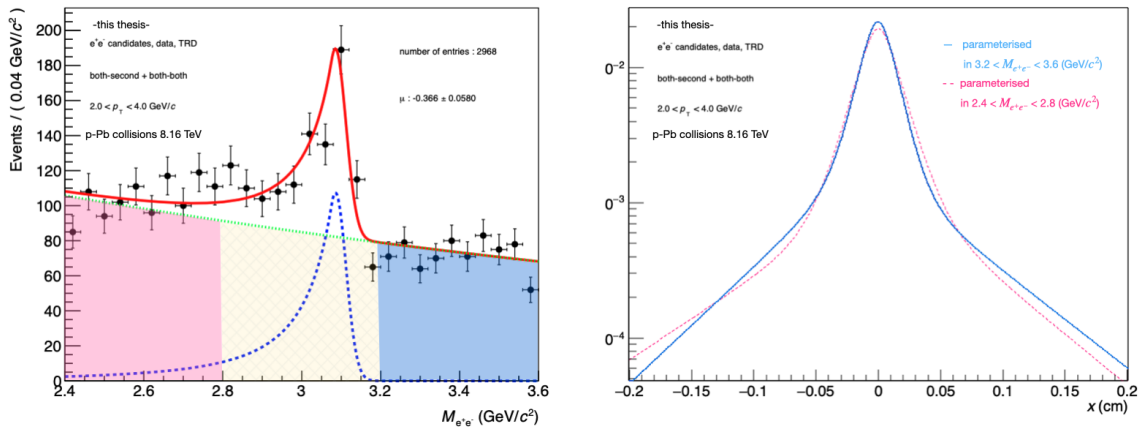

Figure 5.10: (Left) Invariant mass distribution of J/ψ candidates in data in $2 < p_T < 4$ GeV/c showing three invariant mass regions defined and used in this analysis shown as distinguishable filled areas. (Right) Parameterized background pseudo-proper decay-length distributions for the data sample in $2 < p_T < 4$ GeV/c for LS (2.4 GeV/$c^2 \leq M_{e^+e^-} \leq 2.8$ GeV/c^2)and RS(3.2 GeV/$c^2 \leq M_{e^+e^-} \leq 3.6$ GeV/c^2) regions separately.

not be directly accessed due to the presence of the J/ψ signal. Therefore, the background pseudo-proper decay-length distribution in the US region was obtained from an interpolation from the LS and RS regions assuming that the different background combinations changes smoothly in invariant mass. The resulting pseudo-proper decay-length distribution in the US region can, thus, be written as a linear combination of those in LS and RS region. In other words,

$$X_{bkg}(x, M_{e^+e^-}) = \begin{cases} X_{LS}(x), \text{ for } 2.4 \text{ GeV}/c^2 \leq M_{e^+e^-} \leq 2.8 \text{ GeV}/c^2 \\ X_{US}(x), \text{ for } 2.8 \text{ GeV}/c^2 \leq M_{e^+e^-} \leq 3.2 \text{ GeV}/c^2 \\ X_{RS}(x), \text{ for } 3.2 \text{ GeV}/c^2 \leq M_{e^+e^-} \leq 3.6 \text{ GeV}/c^2, \end{cases} \tag{5.13}$$

with

$$X_{US}(x) = cX'_{LS}(x) + (1-c)X'_{RS}(x), \;\; 0 \leq c \leq 1, \tag{5.14}$$

where the coefficient c, which describes relative fraction of the LS (RS) shape in the interpolation, was determined from full likelihood function scan on c while fixing all other PDFs. The c was chosen as the value which gives the smallest log-likelihood value. In order to better understand invariant mass dependence of pseudo-proper decay-length distributions, the TRD-triggered events collected in pp collisions at $\sqrt{s}$=13 TeV, which have about factor 4 larger data sample, was used for further investigation. In Figure 5.11, the pseudo-proper decay-length distributions are shown for different side band regions. While the distributions become narrower as the ranges get closer to the J/ψ signal range in the LS region, the contribution of right tail in the distribution changes depending on the distance to J/ψ signal range in the RS region. As the pseudo-proper decay-length distributions of background highly rely on the underlying events and abundance of different particle species, the distributions obtained from the data of pp collisions were not directly applicable for describing p-Pb data. Nevertheless, the study with the pp data sample clearly indicates that pseudo-proper decay-length distributions depend on the

invariant mass. Based on this result, instead of the full side band ranges (X_{LS}, X_{RS}), a narrow range

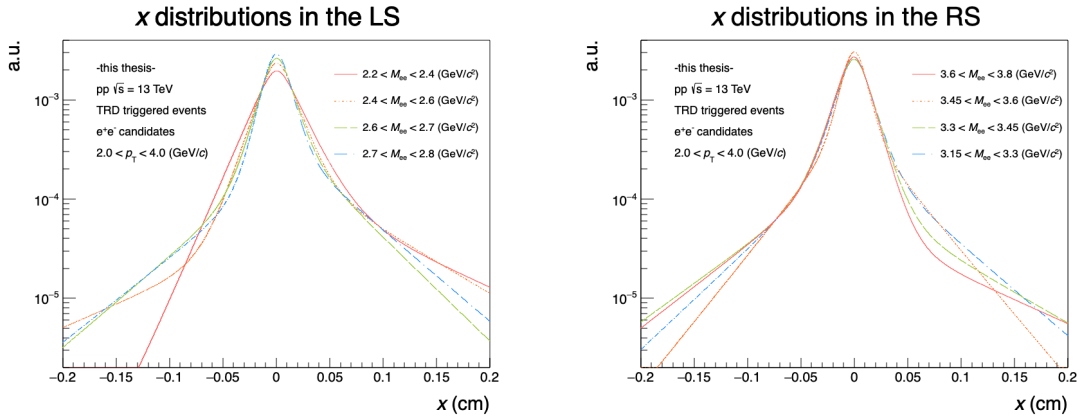

Figure 5.11: Pseudo-proper decay-length distributions of background in the data sample collected in pp $\sqrt{s} = 13$ TeV for e^+e^- candidates in $2 < p_T < 4\,\mathrm{GeV}/c$. The e^+e^- pairs were obtained with same event and track selection criteria used for in p–Pb data. Pseudo-proper decay-length distributions are shown for different side band regions.

of the invariant mass (X'_{LS}, X'_{RS}) close to the US region was used for obtaining the pseudo-proper decay-length distributions for the interpolation. So, for each p_T interval, four different distributions from different invariant mass regions were used to construct the full pseudo-proper decay-length distributions of backgrounds.

Apart from the invariant mass dependence of the pseudo-proper decay-length discussed above, the four of distributions X_{LS}, X_{RS}, X'_{LS} and X'_{RS} can be influenced by several sources. Given the limited statistics of background, the parameterization of pseudo-proper decay-length distribution can be affected by statistical fluctuations. In addition, some fraction of the J/ψ presented in the side-band region can disturb precise estimation of the pseudo-proper decay-length distribution for background. In order to propagate these sources of systematic uncertainty, the four of the distributions, X_{LS}, X_{RS}, X'_{LS} and X'_{RS}, were varied by changing the corresponding invariant mass ranges.

5.2.6 Fit results

The results of the extended unbinned maximum likelihood fit defined in Equation 5.6 in each p_T interval, projected on the invariant mass and pseudo-proper decay-length are presented in Fig. 5.3. The minimization of Equation 5.6 was performed by MINUIT [218] using the RooFit [219] framework. The resulting parameters and the their errors from fit are reported in Table 5.2. The errors were obtained by finding the points where $\Delta \ln L = 0.5$ via MINOS and taken as statistical uncertainty.

5.3 Acceptance and efficiency correction

The raw non-prompt J/ψ fraction f'_B obtained from the likelihood fit was corrected in each p_T interval based on the following formula assuming no strong rapidity dependence of acceptance times efficiency

p_{T} interval	raw non-prompt J/ψ fraction (f'_{B})
2 GeV/c < p_{T} < 14 GeV/c	0.1989 ± 0.027
2 GeV/c < p_{T} < 4 GeV/c	0.1226 ± 0.046
4 GeV/c < p_{T} < 6 GeV/c	0.2198 ± 0.042
6 GeV/c < p_{T} < 8 GeV/c	0.2799 ± 0.052
8 GeV/c < p_{T} < 10 GeV/c	0.3309 ± 0.086
10 GeV/c < p_{T} < 14 GeV/c	0.3339 ± 0.1064

Table 5.2: Raw non-prompt J/ψ fraction (f'_B) from the maximum likelihood fit for each p_{T} interval. The error of parameter obtained from fit is taken as statistical uncertainty.

in the given kinematic range,

$$f_B = \left(1 + \frac{1 - f'_B}{f'_B} \cdot \frac{\langle A \times \epsilon \rangle_{h_B \to \mathrm{J}/\psi}}{\langle A \times \epsilon \rangle_{\text{prompt J}/\psi}}\right)^{-1}, \tag{5.15}$$

where $\langle A \times \epsilon \rangle$ represents the mean acceptance times efficiency in the given p_{T} interval,

$$< A \times \epsilon >= \frac{\int_{p_{\mathrm{T}},min}^{p_{\mathrm{T}},max} A \times \epsilon(p_{\mathrm{T}}) \frac{\mathrm{d}N}{\mathrm{d}p_{\mathrm{T}}}}{\int_{p_{\mathrm{T}},min}^{p_{\mathrm{T}},max} \frac{\mathrm{d}N}{\mathrm{d}p_{\mathrm{T}}}}. \tag{5.16}$$

The correction factor as a function of p_{T}, $(A \times \epsilon(p_{\mathrm{T}}))$, for prompt and non-prompt J/ψ was calculated based on MC simulations. As discussed in Chapter 4, prompt J/ψ was generated based on measured inclusive J/ψ production in p-Pb collisions at forward rapidity $\sqrt{s_{\mathrm{NN}}}$ = 8.16 TeV [208] and non-prompt J/ψ was generated by PYTHIA [81] produced $b\bar{b}$ pairs decaying into J/ψ via EvtGen [209] and detector response was simulated via GEANT3 [211]. For the correction procedure, the p_{T} differential yields for prompt J/ψ and non-prompt J/ψ are important ingredients not only as an integrand of Equation 5.16, but also for estimating the p_{T} differential acceptance and efficiency $(A \times \epsilon(p_{\mathrm{T}}))$. Figure 5.12 shows the p_{T} differential yields for prompt J/ψ and non-prompt J/ψ obtained in different ways. For the comparisons, the p_{T} differential yields from experimental measurements were considered, prompt J/ψ and non-prompt J/ψ production measured in p–Pb collisions at $\sqrt{s_{\mathrm{NN}}}$ = 8.16 TeV, specifically at $1.5 < y < 2.0$ by the LHCb collaboration [220], and ALICE measurement in p–Pb collisions at $\sqrt{s_{\mathrm{NN}}}$ = 5.02 in same kinematic range [221]. Since the collision energy of the ALICE measurements and rapidity range of the LHCb measurements do not perfectly match this analysis, the combination of two measurements was additionally considered. Taking inclusive J/ψ spectrum from the ALICE collaboration $\frac{\mathrm{d}N_{\mathrm{J}/\psi}^{\mathrm{ALICE5TeV}}}{\mathrm{d}p_{\mathrm{T}}}$ and non-prompt J/ψ fraction ($f_{\mathrm{B}}^{\mathrm{LHCb8TeV}}$) from LHCb measurements, prompt and non-prompt J/ψ spectrum were estimated by $\frac{\mathrm{d}N_{\mathrm{J}/\psi}^{\mathrm{ALICE5TeV}}}{\mathrm{d}p_{\mathrm{T}}} \times (1 - f_{\mathrm{B}}^{\mathrm{LHCb8TeV}})$ and $\frac{\mathrm{d}N_{\mathrm{J}/\psi}^{\mathrm{ALICE5TeV}}}{\mathrm{d}p_{\mathrm{T}}} \times f_{\mathrm{B}}^{\mathrm{LHCb8TeV}}$, respectively. The statistical and systematic uncertainties of all measurements were quadratically added and propagated as part of inputs in this analysis. Next, the following functional form was used to parameterise p_{T} spectra with three free parameters, C_0, p_0 and n,

$$f(p_{\mathrm{T}}) = C_0 \frac{p_{\mathrm{T}}}{(1 + (p_{\mathrm{T}}/p_0)^2)^n}. \tag{5.17}$$

p_{T} (GeV/c)	full MC simulation (%)	ALICE 5 TeV (%)	ALICE + LHCb (%)
2 - 4	5.3	3.0	0.0
4 - 6	4.9	1.6	0.0
6 - 8	3.4	1.0	0.2
8 - 10	2.5	0.8	0.3
10 - 14	2.0	0.5	0.3
2 - 14	17.9	6.7	0.1

Table 5.3: The deviation of corrected non-prompt J/ψ fraction with correction factors obtained from different p_{T} spectra, from the one corrected based on the LHCb measurement in % for each p_{T} interval.

The corresponding p_{T} spectra of prompt J/ψ and non-prompt J/ψ are presented in Figure 5.12. The impact of p_{T} spectra on acceptance times efficiency was studied as shown Figure 5.13, obtained by reweighting the p_{T} shape in the full MC simulation. The impact of the differences is quantified by calculating the correction factors for each case and comparing the corrected non-prompt J/ψ fractions. Table 5.3 shows the deviation of corrected non-prompt J/ψ fraction with correction factors obtained from different p_{T} spectra from the one with the correction factor obtained from LHCb measurement in % for each p_{T} interval. Since the shape of p_{T} spectra change rapidly at low p_{T}, the deviation is large for low p_{T} interval ($2 < p_{\mathrm{T}} < 4$ GeV/c) than higher p_{T} ranges. The largest deviation is shown for the wide p_{T} interval ($2 < p_{\mathrm{T}} < 14$ GeV/c) as the effect is accumulated over large p_{T} interval. Overall, large deviation is shown for the results corrected with the full MC simulation, which indicates the limitation of the non-prompt J/ψ generation process implemented in the the full MC simulation. For this reason, the parameterized LHCb p_{T} spectra were used for central point determination as an one of the experimental measurements, and the difference between the corrected results obtained from the ALICE measurements were propagated as a systematic uncertainty.

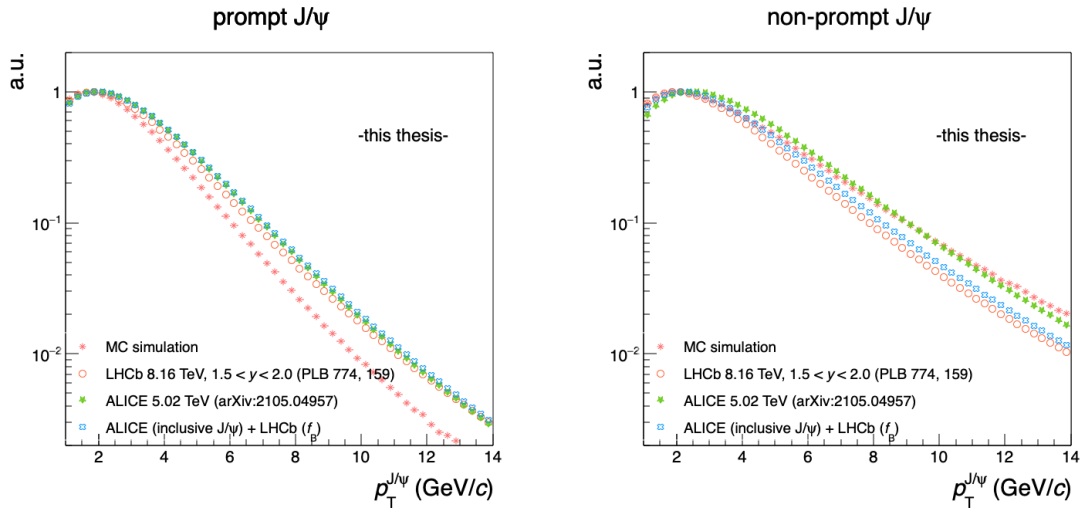

Figure 5.12: p_{T} differential yields for prompt J/ψ and non-prompt J/ψ, normalized to the maximum of each distributions for shape comparison. See the detail in the text.

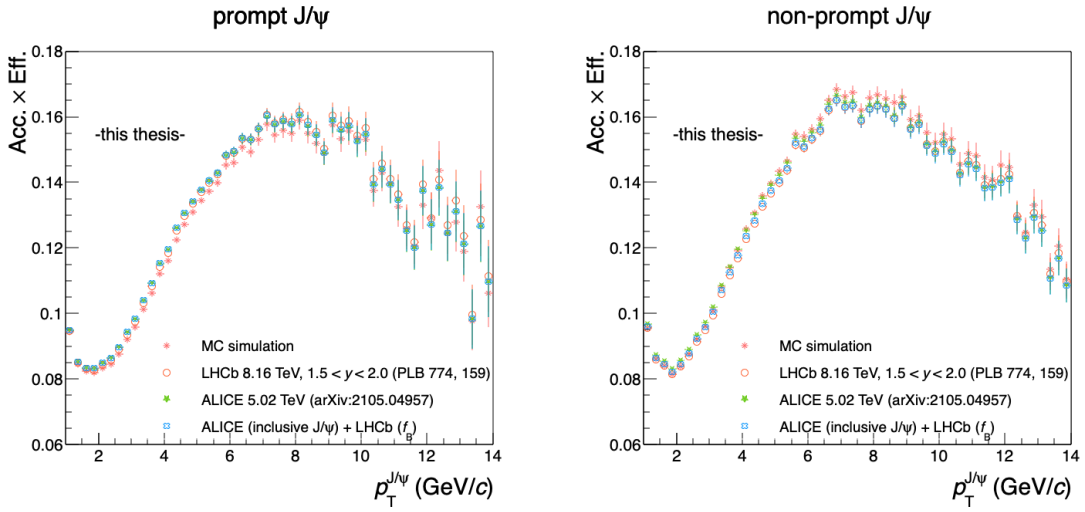

Figure 5.13: (Upper row) Acceptance and efficiency as a function of J/ψ p_{T} for prompt J/ψ and non-prompt J/ψ using different p_{T} shapes. (Bottom row) Acceptance and efficiency including TRD trigger efficiency as a function of J/ψ p_{T} for prompt J/ψ and non-prompt J/ψ using different p_{T} shapes.

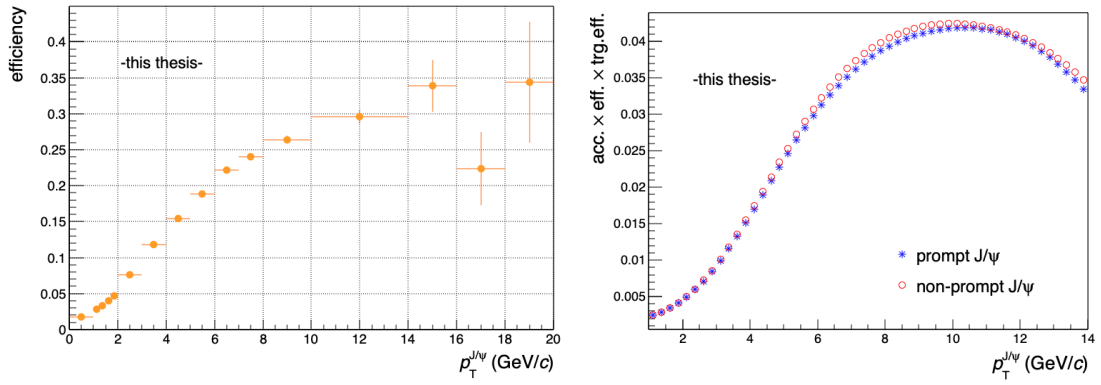

Figure 5.14: TRD trigger efficiency.

5.4 Estimation of systematic uncertainties

The possible biases in the correction procedure and the modelling of the templates used in the likelihood fit were quantitatively estimated and propagated to the final systematic uncertainty.

Although the J/ψ invariant mass distribution obtained from the parameterization of the full MC simulation fairly agrees with the parameterized data in overall invariant mass range as shown in Figure 5.6, a clear discrepancy between the distributions is visible mainly in the tail. Consequently, the uncertainty in the distribution has to be propagated to the uncertainty on the yield. The tail shape of the distribution is mostly determined by the specifics of $\mathrm{e}^{+}\mathrm{e}^{-}$ pairs experiencing Bremsstrahlung as well as a contribution from radiative decays. Assuming that Bremsstrahlung and radiative decays affect the invariant mass distribution in a similar way, the invariant mass distribution from the full MC simulation was split into the distribution of pure QED radiative decays J/ψ ($\mathrm{J}/\psi \rightarrow e^{+}+e^{-}+\gamma$) and of non-radiative J/ψ. The likelihood fit was repeated with these two extreme shapes, then, the standard deviation of uniform PDF,

$\frac{\Delta(\text{radiative,non-radiative})}{\sqrt{12}}$, was taken for final systematic uncertainty for the invariant mass distribution of J/ψ. As summarized in Table 5.4, the uncertainty for the invariant mass distribution of J/ψ is about 2%, but gets larger for the lowest and the highest p_{T} interval where the significance of J/ψ ($\frac{N_{\mathrm{J}/\psi}}{\sqrt{N_{\mathrm{J}/\psi}+N_{bkg.}}}$) is smaller than other intervals.

With the limited statistics of the data, the precise shape of the background distribution cannot be constrained much. The model assumption can thus introduce a bias. In order to take into account the limitation, the modelling of the invariant mass distribution of the background was varied into two directions. First, the exponential functional was replaced to the first order polynomial and the second order polynomial functions. In addition, the parameterization was repeated for the invariant mass distribution of like-sign pairs, i.e. calculated from electron-electron and positron-positron pairs. The likelihood fit was repeated with three alternative templates and the standard deviation of the residuals with respect to the central point was calculated as the final systematic uncertainty for the invariant mass distribution of the background, resulting in about 1.5% at in the lowest p_{T} interval and less than 1% for the rest of the p_{T} intervals. In the p_{T} range $8 < p_{\mathrm{T}} < 10$ GeV/c, this estimate yields a much higher estimate of 2.4% compared to the others. This is likely due to the effect of statistical fluctuations.

The pseudo-proper decay-length distribution of prompt J/ψ is purely determined by resolution effects, which were corrected by calibrating the MC sample to resemble the data. The possible bias in the correction procedure was explored for the systematic uncertainty of the pseudo-proper decay-length distribution of prompt J/ψ. The DCA correction was made based on pions instead of electrons due to the difficulty of selecting pure primary electrons in data. The contribution of Bremsstrahlung was found to be significant at low p_{T} as discussed in Chapter 5.2. As there is no straightforward way to check the Bremsstrahlung effect directly in data, two resolution functions for systematic variation were made by worsening and improving the impact parameter resolution by the difference between pions and electrons determined from the MC simulation. Worsening the impact parameter resolution was a test for the assumption that the Bremsstrahlung effect is double in data with respect to MC sample and improving was for the assumption that the Bremsstrahlung effect does not exist in data. The corresponding raw f'_B from the likelihood fit was obtained, and the standard deviation of the variations was propagated to final systematic uncertainty on pseudo-proper decay-length distribution of prompt J/ψ. The final systematic uncertainty is 3.4% for $2 < p_{\mathrm{T}} < 4$ GeV/c and becomes smaller, less than 1% in higher p_{T}. The larger uncertainty at low p_{T} is understandable, considering the rapid change of the resolution as well as worse resolution in low p_{T} intervals.

The MC simulation for beauty production was made with PYTHIA which gives compatible p_{T} spectra of beauty hadrons with the FONLL prediction [79], which describes the measurements of beauty production fairly well in pp collisions [222, 223, 224]. For this reason, no additional study for p_{T} shape dependence was made. The impact of decay kinematics on $\mathcal{X}_B(x)$, however, was studied with two event generators, EvtGen and PYTHIA. The absolute difference between the results obtained with EvtGen and PYTHIA was taken as the systematic uncertainty of pseudo-proper decay-length distribution of non-prompt J/ψ, resulting in 6.4% for the p_{T} interval $2 < p_{\mathrm{T}} < 4$ GeV/c and 1-2% for the rest of p_{T}

intervals used in this analysis.

The estimated pseudo-proper decay-length distribution of the background changes depending on how three regions in invariant mass, left side band (LS), right side band (RS) and under signal (US) are split. Therefore, the systematic uncertainty of the background pseudo-proper decay-length distribution was estimated based on several variations in ranges of LS and RS, as well as regions for interpolation. However, the change of the distribution could not only arise from physics origins but also due to the statistical fluctuation as data suffered from limited statistics. Two variations for each four regions were separately made, resulting in eight different pseudo-proper decay-length distributions of the background for the estimation of systematic uncertainty. The likelihood fit was repeated with the eight alternative pseudo-proper decay-length distributions of the background and the standard deviation of the residuals with respect to the central point was propagated as the final systematic uncertainty. About 3 $\sim$ 4% at in low p_{T} interval and around 2% for the interval of $p_{\mathrm{T}} >$ 6 GeV/c.

As discussed in the section for the acceptance times efficiency correction, two sets of experimental measurements were available for estimating p_{T} spectra of prompt and non-prompt J/ψ. One of the measurements, the LHCb p_{T} spectra, was used for central point determination and the difference between the corrected results obtained from the ALICE measurements was propagated as a systematic uncertainty. While the acceptance times efficiency was separately calculated for prompt J/ψ and non-prompt J/ψ with the full MC sample, the TRD trigger efficiency was obtained from an MC sample containing only events with prompt J/ψ due to the unrealistic non-prompt J/ψ abundance in MC sample as discussed in Chapter 4. To consider a possible trigger efficiency difference of non-prompt J/ψ events due to the semileptonic decay mode of beauty hadrons to electron, a dedicated MC simulation was used. Events with $b\bar{b}$ pair were generated via PYTHIA. For the half of the simulated events, hadrons from beauty quarks were forced to decay into J/ψ via EvtGen and finally into electron-positron pairs via PHOTOS. At the same time, the hadrons containing anti beauty quarks were required to decay following inclusive decay modes defined in EvtGen. For the rest of the simulated events, hadrons from beauty quarks were asked to decay according to the decay table in the EvtGen and hadrons from anti beauty quarks were forced to be non-prompt J/ψ. In this way, a realistic p_{T} dependent fraction of semileptonic decays electrons and positrons, as well as the correlation between electrons (positrons) from semileptonic decays and non-prompt J/ψ decays, could be implemented in the MC simulations. Then, the trigger selection was made using single electron trigger efficiency obtained from the data which was shown in Figure 4.3. The resulting TRD trigger efficiency as a function of J/ψ is presented in Figure 5.15. The events containing the semileptonic decays electrons have slightly larger TRD trigger efficiency as a function of J/ψ transverse momentum. In addition, as there is no strong correlation between electrons (positrons) from semileptonic decays and non-prompt J/ψ in their kinematics, the efficiency difference is almost flat in J/ψ p_{T} shown in the right panel of Figure 5.15. As the maximum of efficiency difference is less than 3% at p_{T} = 2 GeV/c gets negligible in the higher p_{T}, no additional systematic uncertainty was assigned for this effect.

The systematic uncertainty of each sources were added quadratically and summarized in Table 5.4.

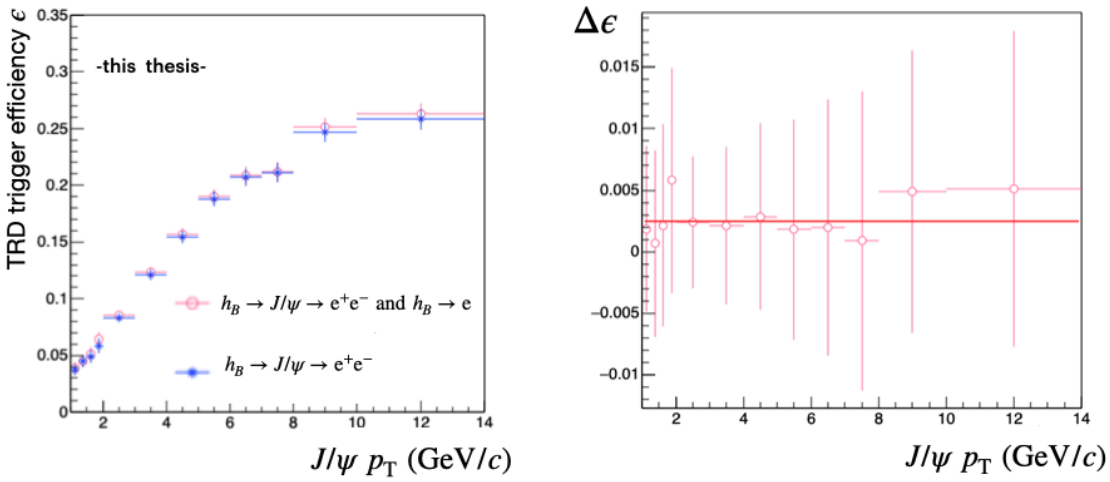

Figure 5.15: TRD trigger efficiency for J/ψ estimated from fast simulation considering the contribution of electrons from s(left) and the efficiency difference between prompt J/ψ and non-prompt J/ψ (right).

p_T (GeV/c)	Signal extraction					Correction	Total (%)
	$M_{ee,J/\psi}$	$M_{ee,bkg.}$	$x_{promptJ/\psi}$	$x_{non-promptJ/\psi}$	$x_{bkg.}$	p_T shape	
2 - 14	2.1	0.6	1.3	3.8	3.8	6.7	9.0
2 - 4	2.6	1.5	3.4	6.4	3.3	3.0	9.0
4 - 6	1.9	0.6	1.0	1.1	3.7	1.6	4.7
6 - 8	0.6	0.1	0.5	1.7	2.0	1.0	2.9
8 - 10	2.2	2.4	0.4	2.2	1.6	0.8	4.3
10 - 14	4.8	0.1	0.4	0.5	2.1	0.5	5.3

Table 5.4: Summary of systematic uncertainty in % for each p_T interval used in this thesis work. individual uncertainties were quadratically added for total systematic uncertainty for given p_T.

6 Measurements of prompt and non-prompt J/ψ production in p–Pb collisions at $\sqrt{s_{NN}}$ = 8.16 TeV

As discussed in the previous chapter, the fraction of non-prompt J/ψ, the relative contribution of non-prompt J/ψ among inclusive J/ψ, was extracted from e^+e^- pairs in the TRD-electron triggered events, based on a statistical approach. By combining the fraction of non-prompt J/ψ (f_B) and inclusive J/ψ production cross section measured in the same kinematic region at the same collision system ($\sigma_{\text{inclusive } J/\psi}$), the prompt J/ψ and non-prompt J/ψ cross sections can be separately determined as follows,

$$\begin{aligned} \sigma_{\text{prompt } J/\psi} &= (1 - f_B) \times \sigma_{\text{inclusive } J/\psi}, \\ \sigma_{\text{non-prompt } J/\psi} &= f_B \times \sigma_{\text{inclusive } J/\psi}. \end{aligned} \tag{6.1}$$

In order to quantify the possible modification of the prompt J/ψ and non-prompt J/ψ production in p–Pb collisions induced by cold-nuclear-matter effects, the corresponding physical observables in pp collisions at $\sqrt{s}$ = 8.16 TeV were required for the comparison. Finally, the nuclear modification factor of prompt J/ψ and non-prompt J/ψ in p–Pb collisions at $\sqrt{s_{NN}}$ = 8.16 TeV were obtained at midrapidity (-1.37 $< y_{J/\psi} <$ 0.43) for the p_T interval $2 < p_T < 14$ GeV/c, and compared with previous measurements, as well as theoretical model predictions.

6.1 Non-prompt J/ψ fraction

The fraction of non-prompt J/ψ (f_B) at midrapidity (-1.37 $< y_{J/\psi} <$ 0.43) in p–Pb collisions at $\sqrt{s_{NN}}$ = 8.16 TeV is presented as a function of the J/ψ transverse momentum (p_T) in the both panels of Figure 6.1. As discussed in previous chapter, the fraction of non-prompt J/ψ from two-dimensional likelihood fit (f'_B) was corrected for the acceptance × efficiency following Equation 5.15. The each data point is placed at the centre of the given p_T interval, which is shown as a horizontal line along the x-axis. For each point, the statistical and systematic uncertainties of f_B were quadratically added and shown as a vertical line. The fraction of non-prompt J/ψ (f_B) is about 0.12 at the lowest p_T interval, $2 < p_T < 4$ GeV/c, and increase as a function of J/ψ p_T, reaching 0.33 at the highest p_T interval, $10 < p_T < 14$ GeV/c. In the left panel of Figure 6.1, the f_B measured at midrapidity in p–Pb collisions at $\sqrt{s_{NN}}$ = 8.16 TeV is presented together with previous ALICE [228] and ATLAS [225] measurements at midrapidity in p–Pb collisions at $\sqrt{s_{NN}}$ = 5.02 TeV. Like the measurement of this thesis work, the data point is located at the centre of the given p_T interval, and the quadratic sum of the statistical and systematic uncertainties is presented as a vertical line. The previous measurements at midrapidity in

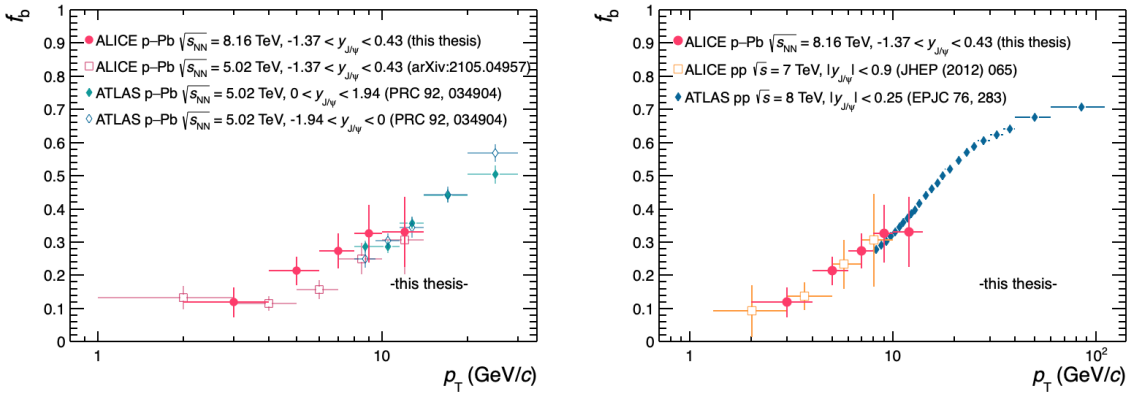

Figure 6.1: The fraction of non-prompt J/ψ as a function of p_T at midrapidity (-1.37 < $y_{J/\psi}$ < 0.43) in p–Pb collisions at $\sqrt{s_{NN}}$ = 8.16 TeV, in comparison with previous measurements in p–Pb collisions at $\sqrt{s_{NN}}$ = 5.02 TeV by the ALICE collaboration [221] and by the ATLAS collaboration [225] (left) and in pp collisions at $\sqrt{s}$ = 7 TeV by the ALICE collaboration [226] and at $\sqrt{s}$ = 8 TeV by the ATLAS collaboration [227] (right). Note that the rapidity intervals of some measurements are slightly different.

p–Pb collisions at $\sqrt{s_{NN}}$ = 5.02 TeV show the increasing trend in J/ψ transverse momentum, similar to what was observed in the measurement at $\sqrt{s_{NN}}$ = 8.16 TeV. At intermediate-p_T interval, $4 < p_T < 10$ GeV/c, there is a hint of slightly higher non-prompt J/ψ fraction measured at $\sqrt{s_{NN}}$ = 8.16 TeV with respect to the one measured at $\sqrt{s_{NN}}$ = 5.02 TeV. The significance is indeterminable under the current measurement precision. However, it is notable that there is a hint of an increase of the non-prompt J/ψ fraction with increasing collision energy observed in pp collisions [108]. A similar comparison with the measurements in pp collisions at similar collision energies can be found in the right panel of Figure 6.1. The measured fraction on non-prompt J/ψ in p–Pb collisions is compatible with the low- and intermediate-p_T interval, $2 < p_T < 10$ GeV/c result in pp collisions from the ALICE collaboration [226] and high-p_T interval $p_T > 8$ GeV/c measured by the ATLAS collaboration [227]. The agreement of the results from pp collisions and p–Pb collisions indicates that the possible production modification induced by the presence of nuclei (CNM) does not change the relative fraction of non-prompt J/ψ under the present measurement precision. In order to see the individual production modification of prompt and non-prompt J/ψ in p–Pb collisions, the resulting non-prompt J/ψ fraction was combined with the measurement of inclusive J/ψ production for further investigation.

6.2 Production cross sections of prompt J/ψ and non-prompt J/ψ

The prompt J/ψ and non-prompt J/ψ production cross sections can be derived from the measurement of the non-prompt J/ψ fraction $f_B$as shown in Equation 6.1. Similarly, the p_T-differential production cross section of prompt J/ψ ($\frac{d\sigma_{\text{prompt J}/\psi}}{dp_T dy}$) and non-prompt J/ψ ($\frac{d\sigma_{\text{non-prompt J}/\psi}}{dp_T dy}$) can be written as

$$\begin{aligned} \frac{d\sigma_{\text{prompt J}/\psi}}{dp_T dy} &= (1 - f_B(p_T)) \times \frac{d\sigma_{\text{inclusive J}/\psi}}{dp_T dy}, \\ \frac{d\sigma_{\text{non-prompt J}/\psi}}{dp_T dy} &= f_B(p_T) \times \frac{d\sigma_{\text{inclusive J}/\psi}}{dp_T dy}. \end{aligned} \tag{6.2}$$

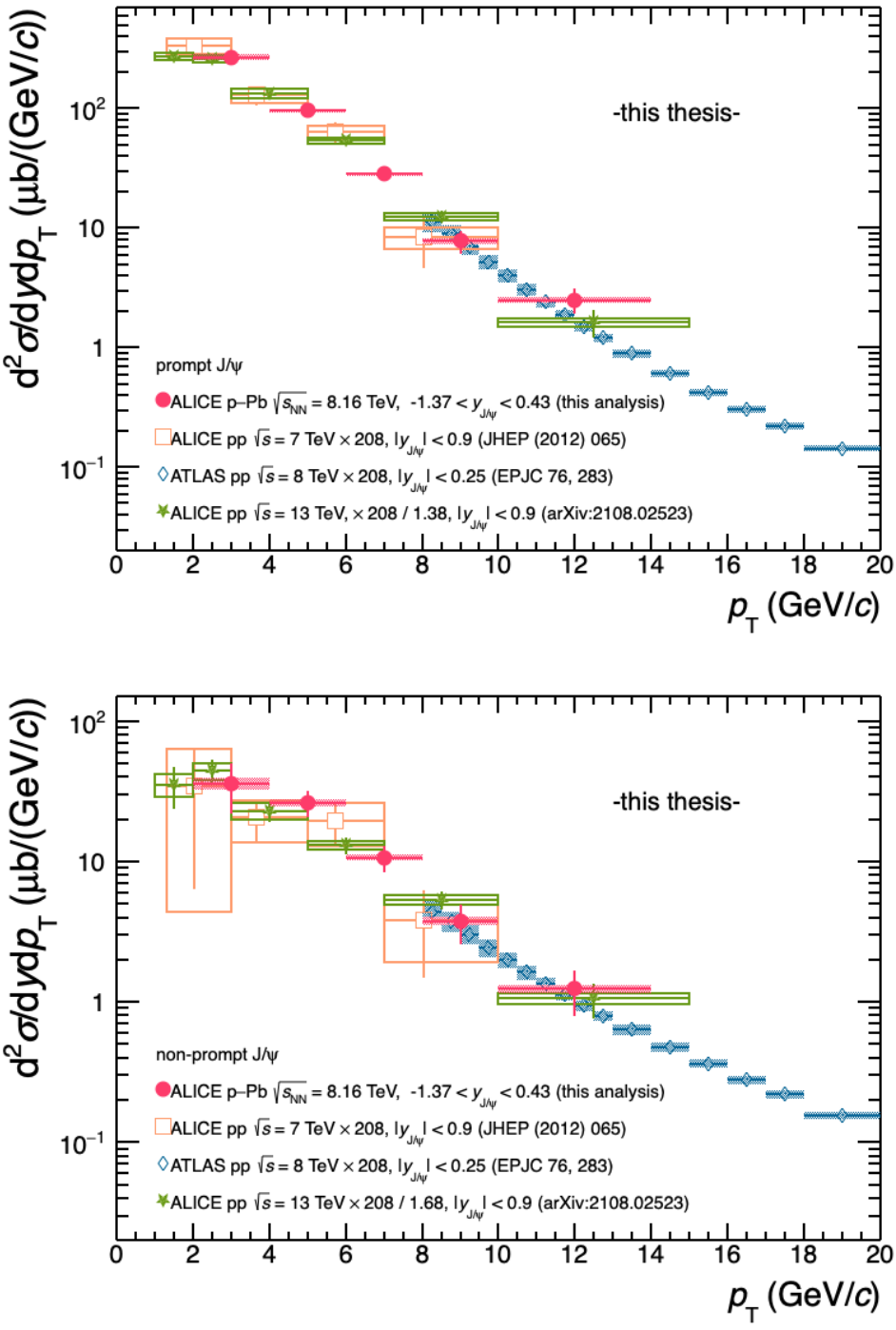

Figure 6.2: The double-differential cross section of prompt J/ψ (upper) and of non-prompt J/ψ (bottom). The data points are placed at the centre of the given p_T intervals. The horizontal error bars indicate the bin widths. The vertical error bars and boxes represent the statistical and the systematic uncertainties, respectively. The global uncertainty of 2% (including branching ratio, TRD trigger normalization and luminosity) is not shown. The measurements in pp collisions were scaled by the mass number of the Pb ion, A = 208. The double-differential cross sections of prompt J/ψ and of non-prompt J/ψ from the ATLAS collaboration [227] were scaled by inverse of the branching ratio of $J/\psi \rightarrow \mu\mu$, which is 0.0593 [15]. For $\sqrt{s}$ = 13 TeV, additional scale factors ($\frac{\sigma^{13TeV}}{\sigma^{8TeV}}$) were applied for collision energy difference.

The inclusive J/ψ production cross section measured in p–Pb collisions at $\sqrt{s_{NN}}$ = 8.16 TeV at same kinematic region [205] was used for the results presented in this chapter. The Figure 6.2 presents the p_T-differential cross section of prompt J/ψ in the upper panel and of non-prompt J/ψ in the bottom panel. The statistical (systematic) uncertainty of the measured f_B and inclusive J/ψ production cross section were propagated as statistical (systematic) uncertainty of the prompt and non-prompt J/ψ cross section, shown as a vertical line (a filled square box). It is clearly seen that the prompt J/ψ and non-prompt J/ψ production cross sections are dominated by statistical uncertainties. The results were compared with the same measurements in pp collisions at similar collision energies, scaled by the mass number of the Pb ion, A = 208. For the cross sections measured at $\sqrt{s}$ = 13 TeV, an additional scale factor was applied to compensate for the collision energy difference. The scale factors for prompt J/ψ and non-prompt J/ψ were obtained from their cross section ratio ($\frac{\sigma^{13TeV}}{\sigma^{8TeV}}$) measured by the LHCb collaboration [229, 230]. The ratios measured in the rapidity interval $2 < y < 2.5$, integrated over p_T, $\frac{\sigma^{13TeV}}{\sigma^{8TeV}}|_{\text{prompt } J/\psi}$ = 1.38 and $\frac{\sigma^{13TeV}}{\sigma^{8TeV}}|_{\text{non-prompt } J/\psi}$ = 1.68 were taken for the scaling. Since the correction was introduced only for qualitative comparisons, the uncertainties of the scale factors were ignored. As illustrated in Figure 6.2, the double-differential cross section of prompt J/ψ and non-prompt J/ψ measured in p–Pb collisions at $\sqrt{s_{NN}}$ = 8.16 TeV is well inline with the results measured at the similar collision energies in pp collisions as a function of p_T. The results provide the hint that there is no strong modification of prompt J/ψ and non-prompt J/ψ production in p–Pb collisions.

The measured double-differential cross section of prompt J/ψ and of non-prompt J/ψ at midrapidity, as well as the LHCb measurements at forward and backward rapidity [220], were compared with theoretical calculations including nPDF effect [231, 232] as presented in Figure 6.3. The solid bands along the measurements show the calculation from Duwentäster et al. [220]. In the calculations, prompt and non-prompt J/ψ production is calculated based on the collinear factorization [147] and the CNM effects are included by the nCTEC15 [59] based PDF set, the so-called nCTEQ15HQ [231, 232]. The nCTEQ15HQ was obtained from the nCTEQ15 parameterization, but the next-to-leading order uncertainties are further constrained by the most of all heavy-flavour and quarkonium production measurements in p–Pb collisions available at the LHC. The calculation well describe the double-differential cross section of prompt J/ψ and of non-prompt J/ψ measured at different rapidity regions simultaneously above p_T > 3 GeV/c.

The integrated cross section of the inclusive J/ψ in the p_T interval $2 < p_T < 14$ GeV/c is measured as $\sigma_{\text{inclusive } J/\psi}$ = 1739.63 ± 131.75 (stat.) ± 60.63 (syst.) μb [205]. And, the non-prompt J/ψ fraction in the p_T interval $2 < p_T < 14$ GeV/c is f_B= 0.175± 0.028 (stat.) ± 0.016 (syst.). Using Equation 6.1, the total cross section of prompt J/ψ ($\sigma_{\text{prompt } J/\psi}$) and non-prompt J/ψ ($\sigma_{\text{non-prompt } J/\psi}$ in visible region, $2 < p_T < 14$ GeV/c and -1.37 < y < 0.43, were obtained,

$$\begin{aligned} \sigma_{\text{prompt } J/\psi} &= 1435.19 \pm 119.11\ (\text{stat.}) \pm 57.24\ (\text{syst.})\ \mu b, \\ \sigma_{\text{non-prompt } J/\psi} &= 304.44 \pm 53.89\ (\text{stat.}) \pm 29.79\ (\text{syst.})\ \mu b. \end{aligned} \tag{6.3}$$

In order to extrapolate the production cross sections down to p_T > 0, the extrapolation factor was defined

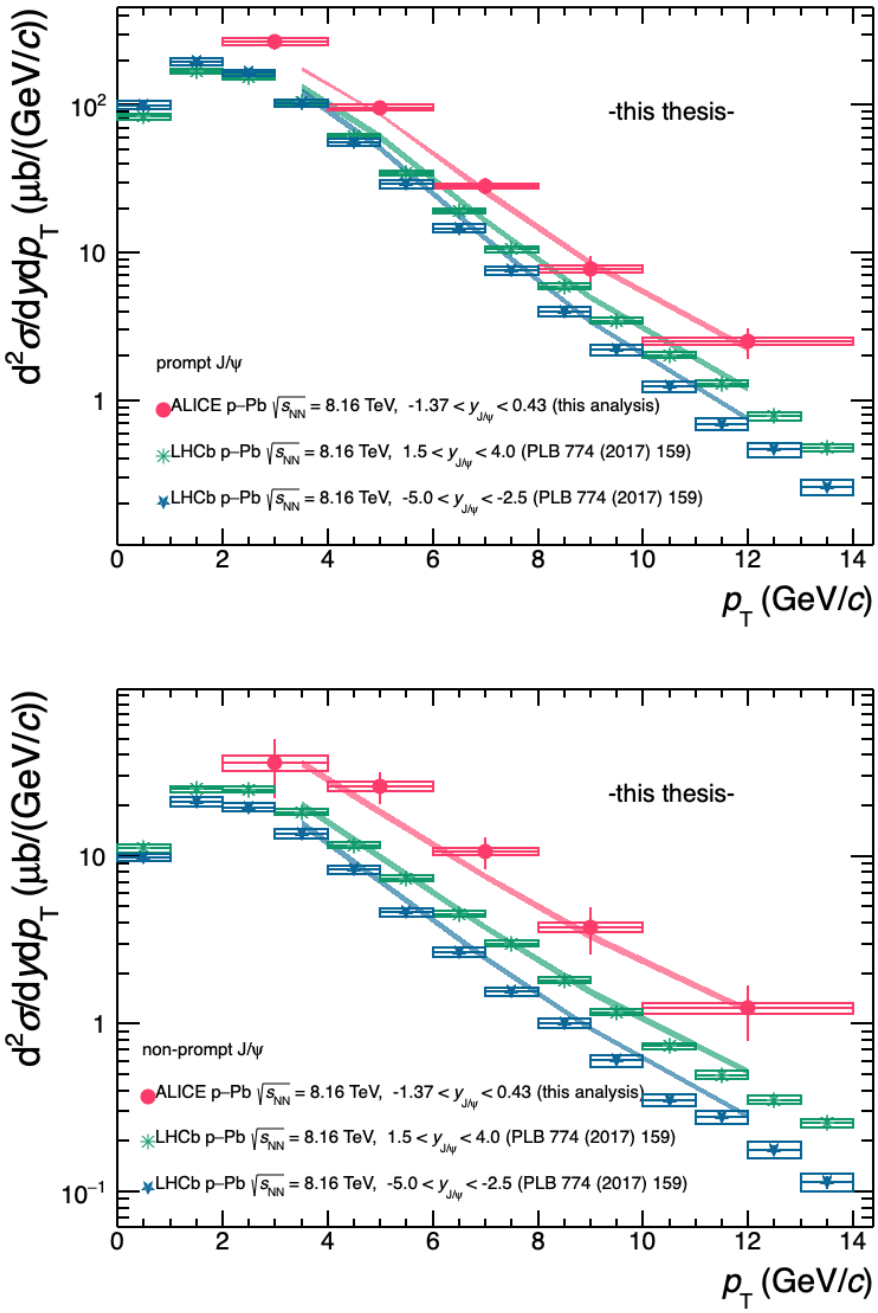

Figure 6.3: The double-differential cross section of prompt J/ψ (upper) and of non-prompt J/ψ (bottom). The data points are placed at the centre of the given p_T intervals. The horizontal error bars indicate the bin widths. The vertical error bars and boxes represent the statistical and the systematic uncertainties, respectively. The measurements by the LHCb collaboration at forward and backward rapidity are presented [220]. Solid bands along the measurements show the model calculation including nPDF effect [231, 232].

as a ratio of the cross section for J/ψ $p_T > 0$ and -1.37 < y < 0.43 to that in the visible region, for inclusive

J/ψ ($\alpha_{\text{inclusive } J/\psi}$) and non-prompt J/ψ ($\alpha_{\text{non-prompt } J/\psi}$),

$$\begin{aligned}
\alpha_{\text{inclusive } J/\psi} &= \frac{\int_{p_T=0}^{p_T=14\text{GeV}/c} \frac{d\sigma_{\text{inclusive } J/\psi}}{dp_T dy} \cdot dp_T}{\int_{p_T=2\text{GeV}/c}^{p_T=14\text{GeV}/c} \frac{d\sigma_{\text{inclusive } J/\psi}}{dp_T dy} \cdot dp_T}, \\
\alpha_{\text{non-prompt } J/\psi} &= \frac{\int_{p_T=0}^{p_T=14\text{GeV}/c} \frac{d\sigma_{\text{non-prompt } J/\psi}}{dp_T dy} \cdot dp_T}{\int_{p_T=2\text{GeV}/c}^{p_T=14\text{GeV}/c} \frac{d\sigma_{\text{non-prompt } J/\psi}}{dp_T dy} \cdot dp_T}.
\end{aligned} \tag{6.4}$$

Previous LHCb measurements of prompt and non-prompt J/ψ production [220], as well as the measurements of inclusive J/ψ production by the ALICE collaboration [233] show no strong collision energy dependence in the shape of the p_T-different cross sections of prompt and non-prompt J/ψ. Based on the fact, by assuming that there is no strong collision energy dependence of the kinematic distributions, the $\alpha_{\text{inclusive } J/\psi}$ was calculated from the inclusive J/ψ production cross section measured in p–Pb collisions at $\sqrt{s_{\text{NN}}}$ = 5.02 TeV [228] following Equation 6.4. Statistical and systematic uncertainties were propagated separately under the assumption that there is no correlation, which yield conservative estimation. The resulting $\alpha_{\text{inclusive } J/\psi}$ is $\alpha_{\text{inclusive } J/\psi} = 1.51 \pm 0.040\,(\text{stat.}) \pm 0.102\,(\text{syst.})$. As the measurements of non-prompt J/ψ production in p–Pb collisions at $\sqrt{s_{\text{NN}}}$ = 5.02 TeV at midrapidity [228] show small CNM effects without strong p_T dependence, the input cross section $d\sigma_{\text{non-prompt } J/\psi}$ for Equation 6.4 was taken from the FONLL prediction [79]. The FONLL calculation includes the uncertainties from the factorization and renormalization scales, μ_F and μ_R, estimated by varying the beauty-quark mass within $4.5 < m_b < 5.0$ GeV/c^2 as well as the uncertainties of the parton distribution functions. In this thesis work, the $\alpha_{\text{non-prompt } J/\psi}$ obtained for $\sqrt{s}$ = 5 TeV is used, $\alpha_{\text{non-prompt } J/\psi} = 1.559^{+0.048}_{-0.099}$ [108]. Then, the extrapolation factors, $\alpha_{\text{inclusive } J/\psi}$ and $\alpha_{\text{non-prompt } J/\psi}$, were applied to the cross sections obtained in the visible region, resulting

$$\begin{aligned}
\sigma^{\text{ext.}}_{\text{inclusive } J/\psi} &= 2630.89 \pm 211.25\,(\text{stat.}) \pm 200.07\,(\text{syst.})\ \mu\text{b} \\
\sigma^{\text{ext.}}_{\text{non-prompt } J/\psi} &= 474.61 \pm 84.02\,(\text{stat.}) \pm 46.44\,(\text{syst.})^{+14.61}_{-30.14}\,(\text{extr.})\ \mu b. \\
\sigma^{\text{ext.}}_{\text{prompt } J/\psi} &= \sigma^{\text{ext.}}_{\text{inclusive } J/\psi} - \sigma^{\text{ext.}}_{\text{non-prompt } J/\psi} \\
&= 2156.27 \pm 193.29\,(\text{stat.}) \pm 197.86\,(\text{syst.})^{+14.61}_{-30.14}\,(\text{extr.})\ \mu b.
\end{aligned} \tag{6.5}$$

From this calculation, prompt J/ψ and of non-prompt J/ψ cross section per unit of rapidity at midrapidity was obtained and could be compared with the LHCb measurements at forward and backward rapidity [220] as shown in Figure 6.4. The measurement in this thesis covers the kinematic region which is not reached by the LHCb experiment.

6.3 pp reference

In order to calculate the nuclear modification factor (R_{pPb}) of prompt J/ψ and non-prompt J/ψ, the corresponding measurements in pp collisions are required. Due to the absence of relevant measurements in pp collisions at the same collision energy in the matching kinematic range, the pp reference for this

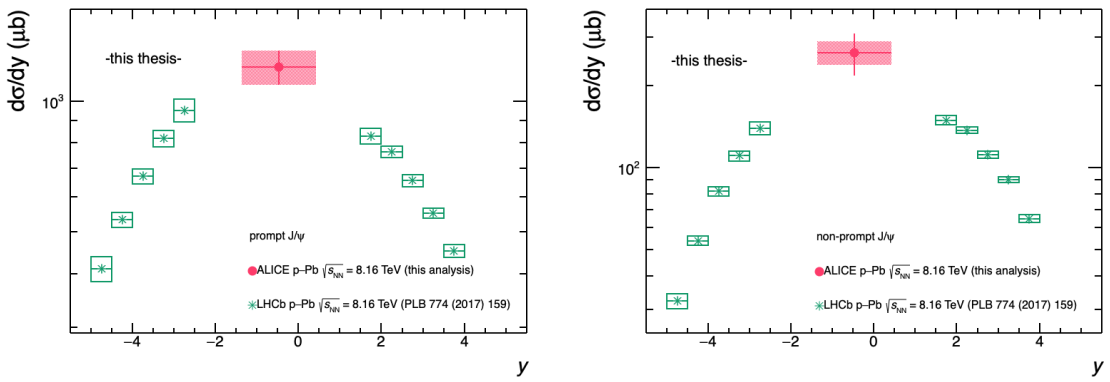

Figure 6.4: The prompt J/ψ (left) and of non-prompt J/ψ (right) cross section per unit of rapidity at midrapidity obtained in this work and in the forward and backward rapidity regions by the LHCb collaboration [220]. The data points are placed at the centre of the given rapidity intervals. The horizontal error bars indicate the bin widths. The vertical error bars and boxes represent the statistical and the systematic uncertainties, respectively.

thesis work was obtained from the interpolation of several existing measurements. The following formulas were used for calculating the nuclear modification factor of prompt J/ψ ($R_{\rm pPb}^{\text{prompt J}/\psi}$) and non-prompt J/ψ ($R_{\rm pPb}^{\text{non-prompt J}/\psi}$) as a function of $p_{\rm T}$,

$$\begin{aligned} R_{\rm pPb}^{\text{prompt J}/\psi}(p_{\rm T}) &= \frac{1 - f_{\rm B}^{\rm p-Pb}(p_{\rm T})}{1 - f_{\rm B}^{\rm pp}(p_{\rm T})} \times R_{\rm pPb}^{\text{inclusive J}/\psi}(p_{\rm T}), \\ R_{\rm pPb}^{\text{non-prompt J}/\psi}(p_{\rm T}) &= \frac{f_{\rm B}^{\rm p-Pb}(p_{\rm T})}{f_{\rm B}^{\rm pp}(p_{\rm T})} \times R_{\rm pPb}^{\text{inclusive J}/\psi}(p_{\rm T}), \end{aligned} \tag{6.6}$$

where the $f_{\rm B}^{\rm pp}$ and $f_{\rm B}^{\rm pp}$ represent the fraction of non-prompt J/ψ in pp collisions and p-Pb collisions, respectively. For the $p_{\rm T}$-integrated nuclear modification factor of prompt J/ψ ($R_{\rm pPb}^{\text{prompt J}/\psi}$) and non-prompt J/ψ ($R_{\rm pPb}^{\text{non-prompt J}/\psi}$), the total cross sections obtained in Equation 6.5 were used as follows,

$$\begin{aligned} R_{\rm pPb}^{\text{prompt J}/\psi} &= \frac{1}{A}\frac{\sigma_{\text{prompt J}/\psi}^{\text{ext.,p-Pb}}}{\sigma_{\text{prompt J}/\psi}^{\text{ext.,pp}}}, \\ R_{\rm pPb}^{\text{non-prompt J}/\psi} &= \frac{1}{A}\frac{\sigma_{\text{non-prompt J}/\psi}^{\text{ext.,p-Pb}}}{\sigma_{\text{non-prompt J}/\psi}^{\text{ext.,pp}}}, \end{aligned} \tag{6.7}$$

where the A is the atomic mass number. Therefore, $f_{\rm B}^{\rm pp}(p_{\rm T})$, $\sigma_{\text{prompt J}/\psi}^{\text{ext.,pp}}$ and $\sigma_{\text{non-prompt J}/\psi}^{\text{ext.,pp}}$ were estimated.

Table 6.1 shows the list of the existing measurements at midrapidity used for estimating $f_{\rm B}^{\rm pp}(p_{\rm T})$. First, the fractions of non-prompt J/ψ as a function of $p_{\rm T}$ was sorted and merged upon their collision energies. Assuming that the production cross section of non-prompt J/ψ is well described by the FONLL [79], the fraction of non-prompt J/ψ as a function of $p_{\rm T}$ for each collision energy was parameterized with the ratio of the $p_{\rm T}$ shape obtained from FONLL [79] for describing the non-prompt J/ψ, and the universal function

centre-of-mass energy	experiments
1.96 TeV	CDF [214]
5.02 TeV	ALICE [108], CMS [234]
7 TeV	ALICE [226], ATLAS [227], CMS [235]
8 TeV	ATLAS [227]
13 TeV	ALICE [108]

Table 6.1: List of measurements of the non-prompt J/ψ fraction in pp collisions at midrapidity used for estimating pp reference for this thesis work.

introduced in Equation 5.17 for describing the inclusive J/ψ, as illustrated in the left panel of Figure 6.5. The statistical and systematic uncertainty of each measurement was added quadratically and considered in the fitting procedure. The right panel of Figure 6.5 shows the results of the parameterization

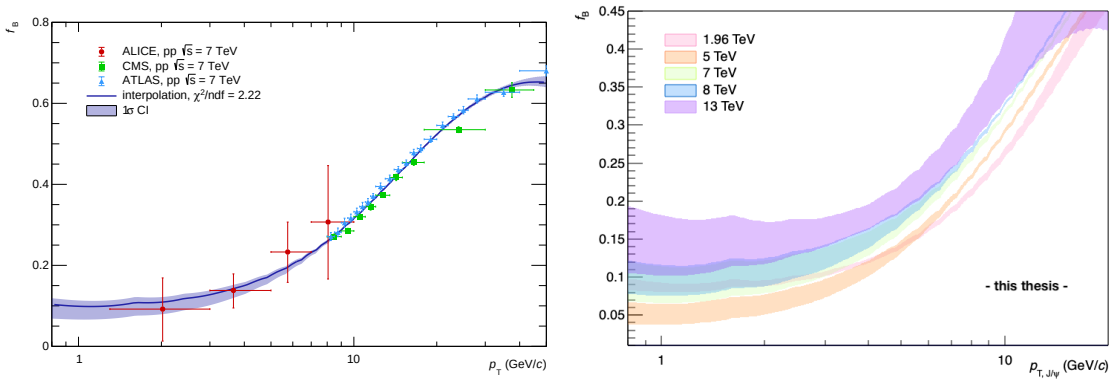

Figure 6.5: (Left) The fraction of non-prompt J/ψ as a function of p_T at midrapidity in pp collisions at $\sqrt{s}$ = 7 TeV measured at ALICE [226], ATLAS [227] and CMS [235] with the fit result represented as a line with the uncertainty band (1σ). (Right) The non-prompt J/ψ fraction fit results for each collision energies.

done for each collision energy. The band represents the fit result in 68% confidence level (1 σ effect). Then, the fractions of non-prompt J/ψ was expressed as a function of $\sqrt{s}$ for each p_T. For example, the left panel of Figure 6.6 shows the $f_B$as a function of collision energy for p_T = 7.84 GeV/c. Since there is no clear model for the collision energy dependence of the non-prompt J/ψ fraction, three different hypotheses, linear, exponential and power-law, were introduced for the interpolation of non-prompt J/ψ fraction to $\sqrt{s}$ = 8.16 TeV. Further, the uncertainty from the parameterization for each collision energy was propagated by repeating the interpolation procedure with the upper limit and lower limit of the fit results. As a result, nine types of the non-prompt J/ψ fraction in pp collisions at $\sqrt{s}$ = 8.16 TeV were obtained as shown in the right panel of Figure 6.6. In comparison to the large difference in $f_B^{pp}(p_T)$ from the variation to the upper (lower) limit of the fit error, the deviation of $f_B^{pp}(p_T)$ derived upon different hypotheses is small, and thus negligible. Then, the mean of $f_B^{pp}(p_T)$ ($< f_B^{pp} >$) was estimated for each p_T interval used in this analysis, $< f_B^{pp} >= \int_{p_T,\text{min.}}^{p_T,\text{max.}} f_B^{pp}(p_T)\, dp_T$.

The total production cross sections of prompt and non-prompt J/ψ measured by the ALICE collaboration in pp collisions at $\sqrt{s}$ = 5.02, 7, and 13 TeV [108, 226] were used for the estimation of $\sigma^{\text{ext.,pp}}_{\text{prompt } J/\psi}$ and

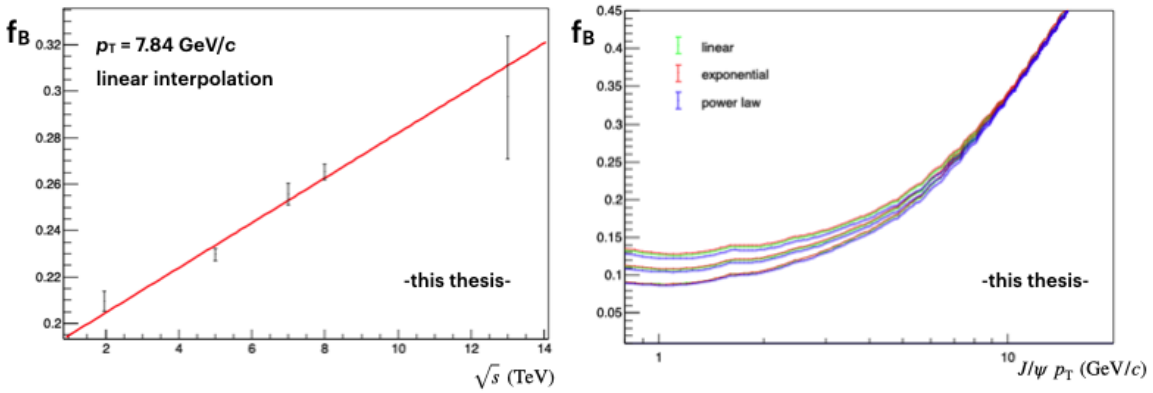

Figure 6.6: (Left) An example of the interpolation of the non-prompt J/ψ fraction to $\sqrt{s}$ = 8.16 TeV based on the previous measurements. (Right) The interpolation of the non-prompt J/ψ fraction based on the different collision energy dependence hypotheses and FONLL uncertainty. Linear, exponential and power law were considered for describing the collision energy dependence. See text for full description.

$\sigma^{\mathrm{ext.,pp}}_{\mathrm{non-prompt\ J}/\psi}$. The measured cross sections were parameterized upon three different hypotheses, linear, exponential and power-law shape along the $\sqrt{s}$ for interpolating at $\sqrt{s}$ = 8.16 TeV. To propagate the uncertainties of each measurement used for the interpolation, a Gaussian distribution having a central point as a mean and statistical (systematic) uncertainty as a width was constructed. The interpolation procedure was repeated many times with different pseudo data set, created based on the distribution.

6.4 R_{pPb} of prompt J/ψ and non-prompt J/ψ

Based on Equation 6.6, the nuclear modification factor of prompt J/ψ in p–Pb collisions ($R^{\mathrm{prompt\ J}/\psi}_{\mathrm{pPb}}$) at $\sqrt{s_{\mathrm{NN}}}$ = 8.16 TeV at $-1.37 < y < 0.43$ is measured as a function of p_{T} and presented in Figure 6.7. The systematic (statistical) uncertainties of the $f_{\mathrm{B}}$and inclusive J/ψ are added and propagated as the systematic (statistical) uncertainty of $R^{\mathrm{prompt\ J}/\psi}_{\mathrm{pPb}}$. $R^{\mathrm{prompt\ J}/\psi}_{\mathrm{pPb}}$ is consistent with unity in the measured kinematic range, constant with p_{T}. The results are compared with previous measurements in p–Pb collisions at $\sqrt{s_{\mathrm{NN}}}$ = 5.02 TeV at midrapidity, the ALICE measurement at $-1.37 < y < 0.43$, ATLAS at $-1.37 < y < 0.43$ and CMS result at $-1.37 < y < 0.43$. All measurements including this thesis result are compatible with each other, showing $R^{\mathrm{prompt\ J}/\psi}_{\mathrm{pPb}} \approx 1$, except for the low p_{T} point ($1 < p_{\mathrm{T}} < 3\ \mathrm{GeV}/c$) of the ALICE measurement at $\sqrt{s_{\mathrm{NN}}}$ = 5.02 TeV, which is 2.53 σ away from 1.

The measured $R^{\mathrm{prompt\ J}/\psi}_{\mathrm{pPb}}$ is compared with theoretical calculations including different CNM effects for the prompt J/ψ production as shown in Figure 6.8. The calculations from Lansberg et al. [147, 236] and from Duwentäster et al. [231, 232] describe the prompt J/ψ production with the framework of NRQCD factorization. In both calculations, the CNM effects are demonstrated by the set of the nPDF. The original EPPS16 [58] and nCTEQ15 [59] parametrization were further constrained by existing measurements of heavy-flavour production in p–Pb collisions at the LHC [236]. The calculations from Lansberg et al. applied so-called Bayesian reweighting approach, employing LHCb measurements of J/ψ [220, 239] as a constraint for the computations. The calculations of Duwentäster et al. include

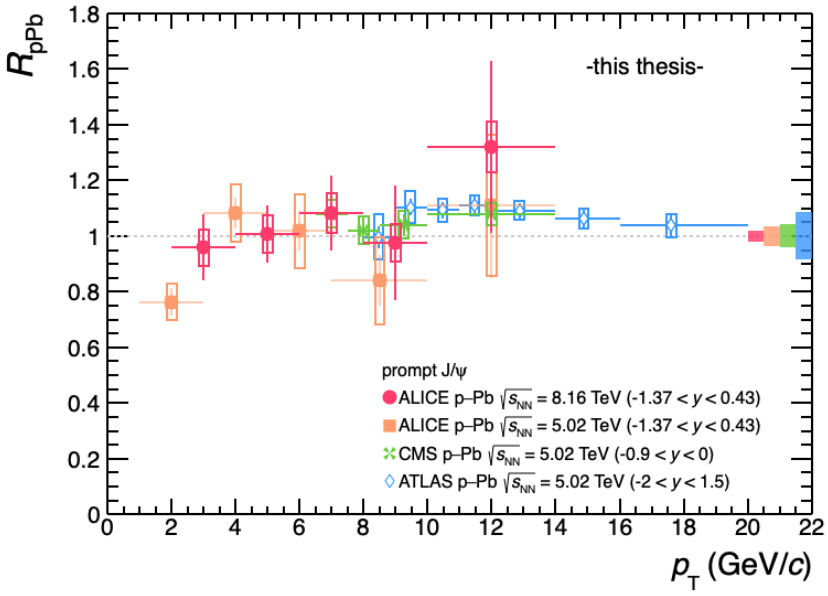

Figure 6.7: Nuclear modification factor of prompt J/ψ as a function of p_{T} at midrapidity. The results are shown in comparison with previous ALICE [221], ATLAS [109] and CMS [110] measurements at $\sqrt{s_{\mathrm{NN}}}$ = 5.02 TeV. Statistical uncertainties are represented by vertical error bars. Systematic uncertainties are shown by open boxes. Filled boxes at $R_{\mathrm{pPb}} = 1$ indicate normalization uncertainties of this thesis, ALICE, CMS and ATLAS measurements from the left. Note that the rapidity intervals of some measurements are slightly different.

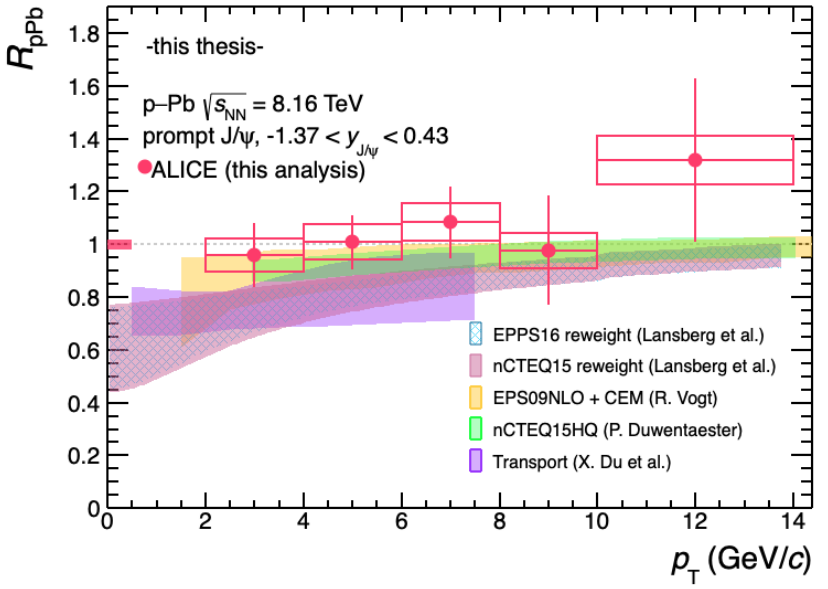

Figure 6.8: Nuclear modification factor of prompt J/ψ at midrapidity at $\sqrt{s_{\mathrm{NN}}}$ = 8.16 TeV as a function of p_{T}. A filled box at $R_{\mathrm{pPb}} = 1$ shows global uncertainty of the TRD normalization and the luminosity. The calculations including different cold nuclear matter effects [147, 231, 236, 237, 238] are shown as well. The calculations from Landsberg et al. were obtained for the measurements at $\sqrt{s_{\mathrm{NN}}}$ = 5.02 TeV.

much more results of open heavy-flavour and quarkonium production measurements in p–Pb collisions

at the LHC, leading to a huge reduction of the uncertainties in the nPDF. The calculation of R. Vogt predicts the prompt J/ψ production using colour evaporation model considering the effects of nPDF using the EPS09NLO set [240]. All models including shadowing effects through the sets of nPDF predict a mild p_{T} dependent suppression of $R_{\mathrm{pPb}}^{\mathrm{prompt\ J}/\psi}$ concentrated for low p_{T}. At the same time, all models describe the measured data within the large uncertainties of models and the data. The model labelled as transport from X. Du et al. [238] has a different picture of the prompt J/ψ production in p–Pb collisions, though the size of the effect is similar to the other models. In the transport model, the production modification in p–Pb collisions is induced from the interaction of $c\bar{c}$ pairs with the thermal medium created in the collision, on top of the shadowing effect. The transport model shows good agreement with data within uncertainties. From the measurement and comparisons with theories, the CNM effects of prompt J/ψ in p–Pb collisions is small at midrapidity for $2 < p_{\mathrm{T}} < 14$ GeV/c.

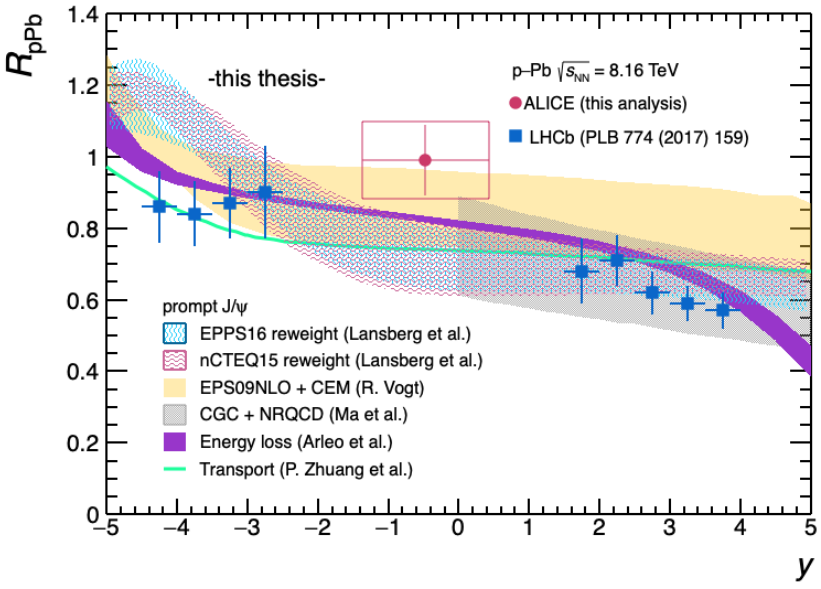

Figure 6.9: Nuclear modification factor of prompt J/ψ as a function of rapidity. Results are shown in comparison with LHCb measurements at forward ($1.5 < y < 4.0$) and backward rapidity ($-5.0 < y < -2.5$). The values are integrated over $0 < p_{\mathrm{T}} < 14$ GeV/c) [220]. The models including different cold nuclear matter effects are also shown [147, 236, 241, 242, 243]

Figure 6.9 shows the $R_{\mathrm{pPb}}^{\mathrm{prompt\ J}/\psi}$ as a function of rapidity. The $R_{\mathrm{pPb}}^{\mathrm{prompt\ J}/\psi}$ was estimated by Equation 6.7, using the extrapolated cross section down to zero transverse momentum reported in Equation 6.5. The measurement in this thesis provides the perfect complement to the LHCb measurements, accessing the kinematic region which is not covered by the LHCb experiment. The statistical and systematic uncertainties of LHCb measurements were quadratically added and presented as vertical lines.The models including shadowing effects via nPDF sets [147, 236] show good agreement with data at forward rapidity and a slightly worse description at midrapidity and backward rapidity. Calculations from CGC approach coupled with the NRQCD description for prompt J/ψ production [242] reproduce the data in forward rapidity corresponding to their domain. It also describes the decreasing trend from midrapidity to the forward region as visible in the data. The model of Arleo et al., including the effects of parton

coherent energy loss [241], as well the transport model [243] give a fairly good description for the trend of the measured $R_{\rm pPb}^{\rm prompt\ J/\psi}$ as a function of rapidity. In the most of model predictions, the $R_{\rm pPb}^{\rm prompt\ J/\psi}$ at midrapidity is inline with the LHCb measurements. Due to the limited precision of the data, the quantitative comparison for discriminating models is not yet possible.

The nuclear modification factor of non-prompt J/ψ in p–Pb collisions ($R_{\rm pPb}^{\rm non-prompt\ J/\psi}$) at $\sqrt{s_{\rm NN}}$ = 8.16 TeV at midrapidity was obtained as a function of $p_{\rm T}$ and is presented in Figure 6.10 using Equation 6.6. The hint of enhancement shown in the intermediate-$p_{\rm T}$ ($4 < p_{\rm T} < 8$ GeV/c) is not significant as the $R_{\rm pPb}^{\rm non-prompt\ J/\psi}$ is only 1.12 σ away from 1 in the $p_{\rm T}$ interval $4 < p_{\rm T} < 6$ GeV/c and 1.19 σ away in $6 < p_{\rm T} < 8$ GeV/c considering the statistical and systematic uncertainties of the measurement. Likewise, considering the uncertainties, the tendency of the $R_{\rm pPb}^{\rm non-prompt\ J/\psi} < 1$ visible for the previous ALICE measurement at $\sqrt{s_{\rm NN}}$ = 5.02 TeV is not significant. Overall, all measurements of $R_{\rm pPb}^{\rm non-prompt\ J/\psi}$ at midrapidity are consistent with unity over $1 < p_{\rm T} < 20$ GeV/c.

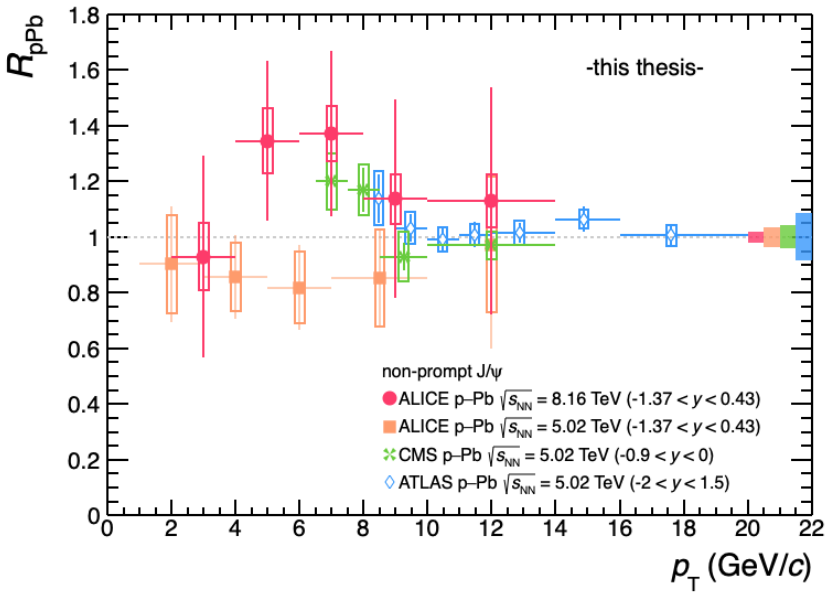

Figure 6.10: Nuclear modification factor of non-prompt J/ψ as a function of $p_{\rm T}$ at midrapidity. The results are shown in comparison with previous ALICE [221], ATLAS [109] and CMS [110] measurements at $\sqrt{s_{\rm NN}}$ = 5.02 TeV. Statistical uncertainties are represented by vertical error bars, while systematic uncertainties are shown by open boxes. Filled boxes at $R_{\rm pPb} = 1$ indicate normalization uncertainties of this thesis, ALICE, CMS and ATLAS measurements from the left. Note that the rapidity intervals of some measurements are slightly different.

The measured $R_{\rm pPb}^{\rm non-prompt\ J/\psi}$ as a function of $p_{\rm T}$ are compared with model predictions including CNM effects induced from nPDF. The calculations from Landsberg et al. and Duwentäster et al. describe the open beauty-hadron production under the collinear factorization [147]. As for the prompt J/ψ, the different sets of nPDFs were adopted to demonstrated the shadowing effects on non-prompt J/ψ production. The calculation based on EPPS16 coupled with the FONLL beauty quark production [228] is also presented in the same plot. As the modification is governed by input nPDF, the trend of EPPS16+FONLL is similar to the calculations from Lansberg et al., consistent with the measurement as well. The tendency

of the models, showing small modification of non-prompt J/ψ production in p-Pb collisions without a strong p_{T} dependence, are consistent with the measurement.

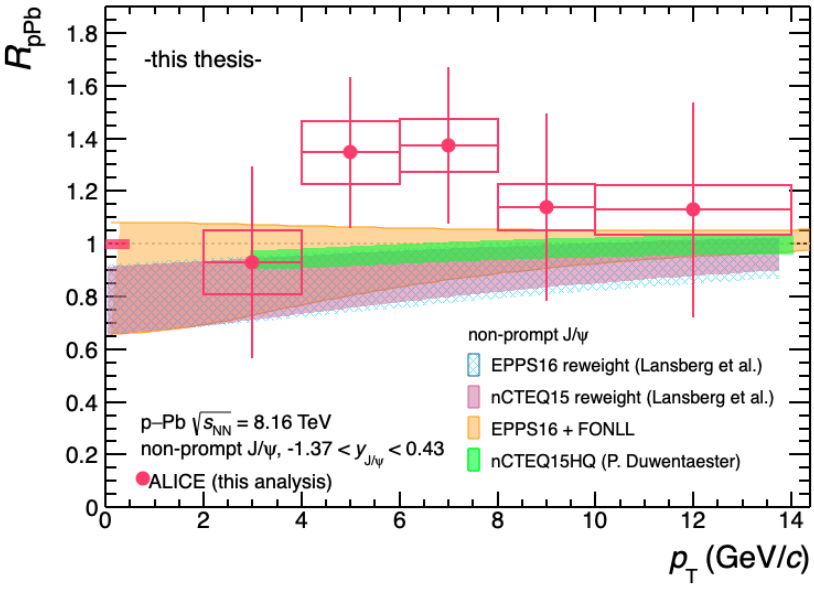

Figure 6.11: Nuclear modification factor of non-prompt J/ψ at midrapidity at $\sqrt{s_{\mathrm{NN}}}$ = 8.16 TeV as a function of p_{T}. A filled box at $R_{\mathrm{pPb}} = 1$ shows global uncertainty of the TRD normalization and the luminosity. The calculations including different sets of nPDF are shown together [58, 59, 147, 231, 232, 236, 244]. The calculations, except for the nCTEQ15HQ, were obtained for the measurements at $\sqrt{s_{\mathrm{NN}}}$ = 5.02 TeV.

The nuclear modification factor of non-prompt J/ψ, $R_{\mathrm{pPb}}^{\mathrm{non-prompt\ J}/\psi}$, is shown as a function of rapidity in Figure 6.12 together with the LHCb measurement [220]. Rapidity dependent modification was observed in the data, showing negligible modification in backward rapidity and midrapidity and weak suppression at forward rapidity. The models including shadowing effects via different sets of nPDF reproduce the trend observed in the measurements well. Both measurements and theoretical calculations indicate a less pronounced rapidity dependent modification of non-prompt J/ψ with respect to prompt J/ψ.

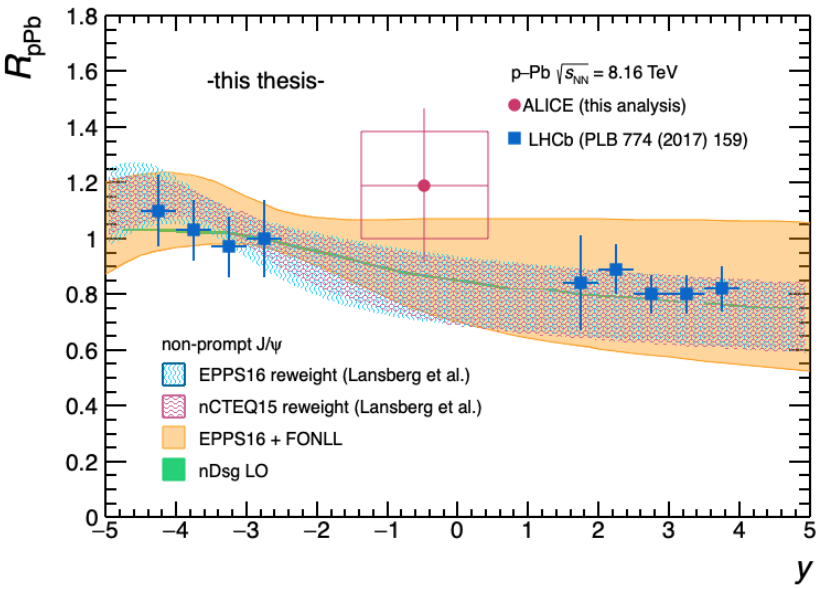

Figure 6.12: Nuclear modification factor of non-prompt J/ψ as a function of rapidity. Results are shown in comparison with LHCb measurements at forward and backward rapidity (integrated over $0 < p_{\mathrm{T}} < 14$ GeV$/c$) [220]. The models including different nPDF are shown together, nDsg LO [245], nCTEQ15 [59] and EPPS16 [58] parameterization (including a reweighted computation from [236]). FONLL [79, 244] computations employing the EPPS16 is superimposed on the plot as well. All theoretical predictions were calculated for $\sqrt{s_{\mathrm{NN}}} = 5.02$ TeV.

7 Conclusions and outlook

In this thesis work, the measurement of prompt J/ψ and non-prompt J/ψ production in p–Pb collisions at $\sqrt{s_{\mathrm{NN}}}$ = 8.16 TeV at midrapidity in the J/ψ transverse momentum interval, $2 < p_{\mathrm{T}} < 14$ GeV/c, was presented. About 50 million TRD-electron triggered events collected in ALICE were used for this thesis work, corresponding to the integrated luminosity of $694.8 \pm 13.3\mu$b. The TRD-electron trigger performance was studied and implemented in the MC sample to obtain the trigger efficiency of J/ψ for the first time in ALICE. The J/ψ mesons were reconstructed in the dielectron channel. The fraction of non-prompt J/ψ mesons, originating from weak decays of beauty hadrons, was measured on a statistical basis via a two-dimensional likelihood fit to the invariant mass and pseudo-proper decay length distributions of J/ψ candidates. Based on the fraction of non-prompt J/ψ and inclusive J/ψ production cross section measured in the same kinematic region at the same collision system [205], the p_{T}- and $y-$ differential cross sections of prompt J/ψ and non-prompt J/ψ were obtained. Since the corresponding measurement in pp collisions at $\sqrt{s}$ = 8.16 TeV does not exist, the pp reference at $\sqrt{s}$ = 8.16 TeV was obtained using the existing prompt and non-prompt J/ψ production measurements in pp collisions at various collision energies.

The measured nuclear modification factor of prompt J/ψ and non-prompt J/ψ, the ratio of the production cross section in p–Pb collisions to that measured in pp collisions scaled by the mass number of the Pb ion, A = 208, was compared with previous measurements and theoretical predictions, including different cold-nuclear-matter effects. At midrapidity, the nuclear modification factor of prompt J/ψ at $\sqrt{s_{\mathrm{NN}}}$ = 8.16 TeV is compatible with unity for p_{T} > 2 GeV/c, showing good agreement with the measurements at $\sqrt{s_{\mathrm{NN}}}$ = 5.02 TeV. Theoretical models including nuclear shadowing with different sets of nPDFs and possible final state effects describe the overall trend of the measurement. Nevertheless, the models show a mild degree of suppression mainly at low p_{T}. The nuclear modification factor of non-prompt J/ψ at $\sqrt{s_{\mathrm{NN}}}$ = 8.16 TeV is close to unity within uncertainties and compatible with the measurements at lower collision energies. Like prompt J/ψ result, theoretical calculations, including different sets of the nPDFs, qualitatively reproduce the measurements. The measurements and comparisons with theoretical calculation suggest a small impact of cold-nuclear-matter (CNM) effects for charm and beauty quarks in the measured kinematic region. Consequently, the strong modifications of prompt J/ψ and open-beauty hadron production in Pb-Pb collisions in comparison to the pp measurements are due to effects of the QGP medium formed in Pb-Pb collisions [129, 152].

The next step towards a better understanding of the physics mechanisms behind the CNM effects would be to quantify the possible modification in the measurements with high precision and discriminate between the models, including different scenarios. In this thesis work, the measurements were limited

by the lack of the available data sample, as reflected in the large statistical uncertainty, the dominant source of the total uncertainty. Further, the limited data sample restricted the construction of the model templates for the two-dimensional likelihood fit. As illustrated in Chapter 5, some of the templates used for the signal extraction were estimated based on the experimental data directly. For example, the pseudo-proper decay length distribution of background was obtained from the sideband region of the invariant mass distribution. The correlation between invariant mass and pseudo-proper decay length of background candidates could be further investigated with a larger data sample for a better description, which would help reduce systematic uncertainty for this measurement. In addition, the pp reference, obtained from the interpolation of multiple measurements due to the absence of a pp reference measured at $\sqrt{s}$ = 8.16 TeV, introduces sizable uncertainties for the measurements in this work. Therefore, it is essential to have precise measurements both in pp collisions and in p–Pb collisions at the same collision energy in the same kinematic region.

During the second Long Shutdown (LS2) starting from 2019, significant upgrades have been successfully implemented both in the ALICE detector and the LHC accelerator chain. After the successful pilot beam campaign in October 2021, Run 3 of the LHC will start in early 2022. The upgrade of the ALICE TPC with Gas Electron Multiplier (GEM) foils for amplification will provide the continuous read-out mode, improving the read-out rate significantly [246]. Consequently, a much larger data sample is expected to be collected in Run 3 in all collision systems. Further, the new ITS, seven layers of Monolithic Active Pixel Sensors (MAPS), will improve the spatial resolution by a factor of 2 - 3 and extend the tracking capabilities to lower p_{T}, down to $\sim$ 200 MeV/c [247]. This is beneficial for the measurements of prompt J/ψ and non-prompt J/ψ production in twofold. First, the discriminating power of the pseudo-proper decay length distributions will be improved with a narrower resolution function. Also, the measurements can be extended down to lower p_{T}, where the CNM effects are expected to be more significant. In addition, the lower material budget of the new ITS will enhance the statistical significance of dielectron analyses by reducing the number of electrons from photon conversions, which produce a large combinatorial background. The upgrades will provide accessibility to new observables, complementing this thesis work, such as fully reconstructed beauty hadrons and excited charmonium states production. While the initial-state effects of the CNM effects for the heavy-quark pair production are expected to affect all different final quarkonium states similarly, the final-state effects, leading to a break-up of the quarkonium resonances, such as larger multiplicity in p–Pb collisions with respect to that in pp collisions, would impact differently for the excited states due to the different binding energies. For example, the comparison of the prompt J/ψ production with the ψ(2S) meson production from the low p_{T} at midrapidity at LHC energies in p–Pb collisions, as well as the P-wave states of charmonium χ_c would be complementary for studying possible final-state effects from the CNM at midrapidity.

On the theory side, the main limitation for this thesis work was the uncertainties of the nPDF sets. Several approaches exist to better constraint the nPDF, especially low x where the gluon density distribution becomes dominant. As presented in Chapter 6, theoretical developments for constraining the gluon density inside the Pb nuclei based on the experimental measurements of inclusive heavy-flavour production in pPb collisions at the LHC has started, showing promising improvements [232, 236]. There

are new ideas to disentangle shadowing from other possible CNM effects in an alternative direction. For example, the disentanglement of shadowing effects from coherent energy loss using the Drell-Yan process has been studied [248]. It is also crucial to better understand the production mechanism in hadronic collisions. In open-heavy flavour production, phenomenologically adopted fragmentation universality should be revisited based on recent measurements of heavy-flavour fragmentation at the LHC [73, 92]. For the quarkonium sector, the simultaneous description of production cross section and polarization remains a challenge [114, 119].

In conclusion, the cold nuclear matter effects for charm and beauty quarks were studied by the measurement of prompt J/ψ and non-prompt J/ψ production in p–Pb collisions at $\sqrt{s_{NN}}$ = 8.16 TeV at midrapidity. The measurements and comparisons with theoretical calculation suggest a small impact of CNM effects for charm and beauty quarks in the measured kinematic region. Improved precision measurements are expected in the upcoming LHC run 3 data taking period. With further theoretical developments, new measurements will allow one to quantitatively estimate CNM effects for charm and beauty quarks and disentangle possible different physics mechanisms behind CNM effects.

Bibliography

[1] L. M. Brown and R. T. Weidner, *physics in encyclopedia britannica*, June, 2021. https://www.britannica.com/science/physics-science.

[2] E. Rutherford, *LXXIX. The scattering of α and β particles by matter and the structure of the atom*, *The London, Edinburgh, and Dublin Philosophical Magazine and Journal of Science* **21** (1911) 669.

[3] J. Chadwick, *Possible Existence of a Neutron*, *Nature* **129** (1932) 312.

[4] H. Yukawa, *On the Interaction of Elementary Particles I*, *Proc. Phys. Math. Soc. Jap.* **17** (1935) 48.

[5] C. M. G. Lattes, G. P. S. OCCHIALINIDR., and C. F. POWELLDR., *Observations on the Tracks of Slow Mesons in Photographic Emulsions*, *Nature* **160** (1947) 453.

[6] G. D. ROCHESTER and C. C. BUTLER, *Evidence for the Existence of New Unstable Elementary Particles*, *Nature* **160** (1947) 855.

[7] V. D. Hopper and S. Biswas, *Evidence Concerning the Existence of the New Unstable Elementary Neutral Particle*, *Phys. Rev.* **80** (1950) 1099.

[8] M. Gell-Mann, *Isotopic Spin and New Unstable Particles*, *Phys. Rev.* **92** (1953) 833.

[9] T. Nakano and K. Nishijima, *Charge Independence for V-particles*, *Progress of Theoretical Physics* **10** (1953) 581.

[10] M. Gell-Mann and Y. Ne'eman, *The Eightfold way: a review with a collection of reprints*, New York : W.A. Benjamin (1964).

[11] W. Heisenberg, *Über den Bau der Atomkerne. I*, *Zeitschrift für Physik* **77** (1932) 1.

[12] V. E. Barnes et al., *Observation of a Hyperon with Strangeness Minus Three*, *Phys. Rev. Lett.* **12** (1964) 204.

[13] M. Gell-Mann, *A Schematic Model of Baryons and Mesons*, *Phys. Lett.* **8** (1964) 214.

[14] G. Zweig, *An SU(3) model for strong interaction symmetry and its breaking. Version 2*, in *DEVELOPMENTS IN THE QUARK THEORY OF HADRONS. VOL. 1. 1964 - 1978*, pp. 22–101 (1964), https://inspirehep.net/literature/4674.

[15] **Particle Data Group** Collaboration, *Review of Particle Physics*, *PTEP* **2020** (2020) 083C01.

[16] W. Pauli, *The Connection Between Spin and Statistics*, *Phys. Rev.* **58** (1940) 716.

[17] O. W. Greenberg, *Spin and Unitary-Spin Independence in a Paraquark Model of Baryons and Mesons*, *Phys. Rev. Lett.* **13** (1964) 598.

[18] M. Y. Han and Y. Nambu, *Three-Triplet Model with Double* $\mathrm{SU}(3)$ *Symmetry*, *Phys. Rev.* **139** (1965) B1006.

[19] J. I. Friedman and H. W. Kendall, *Deep Inelastic Electron Scattering*, *Ann. Rev. Nucl. Sci.* **22** (1972) 203.

[20] J. D. Bjorken, *Asymptotic Sum Rules at Infinite Momentum*, *Phys. Rev.* **179** (1969) 1547.

[21] J. J. Aubert et al., *Experimental Observation of a Heavy Particle* J, *Phys. Rev. Lett.* **33** (1974) 1404.

[22] J. E. Augustin et al., *Discovery of a Narrow Resonance in* e^+e^- *Annihilation*, *Phys. Rev. Lett.* **33** (1974) 1406.

[23] G. 't Hooft and M. Veltman, *Regularization and renormalization of gauge fields*, *Nucl. Phys. B* **44** (1972) 189.

[24] H. Fritzsch and M. Gell-Mann, *Current algebra: Quarks and what else?*, *eConf* **C720906V2** (1972) 135 [hep-ph/0208010].

[25] H. Fritzsch, M. Gell-Mann, and H. Leutwyler, *Advantages of the color octet gluon picture*, *Phys. Lett. B* **47** (1973) 365.

[26] R. K. Ellis, W. J. Stirling, and B. R. Webber, *QCD and Collider physics*, Cambridge Univ. Press (2004).

[27] A. Deur, S. J. Brodsky, and G. F. de Teramond, *The QCD Running Coupling*, *Nucl. Phys.* **90** (2016) 1.

[28] D. J. Gross and F. Wilczek, *Ultraviolet Behavior of Nonabelian Gauge Theories*, *Phys. Rev. Lett.* **30** (1973) 1343.

[29] H. D. Politzer, *Reliable Perturbative Results for Strong Interactions?*, *Phys. Rev. Lett.* **30** (1973) 1346.

[30] **Particle Data Group** Collaboration, *Review of Particle Physics*, *PTEP* **2020** (2020) 083C01.

[31] J. R. Ellis, M. K. Gaillard, and G. G. Ross, *Search for gluons in* e^+ e^- *annihilation*, *Nucl. Phys. B* **111** (1976) 253.

[32] **TASSO** Collaboration, *Evidence for Planar Events in e+ e- Annihilation at High-Energies*, *Phys. Lett. B* **86** (1979) 243.

[33] K. G. Wilson, *Confinement of quarks*, *Phys. Rev. D* **10** (1974) 2445.

[34] J. C. Collins and M. J. Perry, *Superdense Matter: Neutrons or Asymptotically Free Quarks?*, *Phys. Rev. Lett.* **34** (1975) 1353.

[35] N. Cabibbo and G. Parisi, *Exponential Hadronic Spectrum and Quark Liberation*, *Phys. Lett. B* **59** (1975) 67.

[36] R. Hagedorn, *Statistical thermodynamics of strong interactions at high energies*, *Nuovo Cimento, Suppl.* **3** (1965) 147.

[37] E. Shuryak, *Quark-gluon plasma and hadronic production of leptons, photons and psions*, *Phys. Lett. B* **78** (1978) 150.

[38] J. Kogut et al., *Deconfinement and Chiral Symmetry Restoration at Finite Temperatures in SU(2) and SU(3) Gauge Theories*, *Phys. Rev. Lett.* **50** (1983) 393.

[39] **HotQCD** Collaboration, *Chiral crossover in QCD at zero and non-zero chemical potentials*, *Phys. Lett. B* **795** (2019) 15 [1812.08235].

[40] B. Betz, *Jet Propagation and Mach-Cone Formation in (3+1)-dimensional Ideal Hydrodynamics*, Doctoral thesis, Johann Wolfgang Goethe-Universitat in Frankfurt am Main, 10, 2009.

[41] S. Chin, *Transition to hot quark matter in relativistic heavy-ion collision*, *Phys. Lett. B* **78** (1978) 552.

[42] E. V. Shuryak, *Quantum Chromodynamics and the Theory of Superdense Matter*, *Phys. Rept.* **61** (1980) 71.

[43] J. D. Bjorken, *Highly relativistic nucleus-nucleus collisions: The central rapidity region*, *Phys. Rev. D* **27** (1983) 140.

[44] M. Kliemant, R. Sahoo, T. Schuster, and R. Stock, *Global Properties of Nucleus-Nucleus Collisions*, *Lect. Notes Phys.* **785** (2010) 23 [0809.2482].

[45] U. W. Heinz and M. Jacob, *Evidence for a new state of matter: An Assessment of the results from the CERN lead beam program*, nucl-th/0002042.

[46] **NA50** Collaboration, *Anomalous J/ψ suppression in Pb - Pb interactions at 158 GeV/c per nucleon*, *Phys. Lett. B* **410** (1997) 337.

[47] T. Matsui and H. Satz, *J/ψ Suppression by Quark-Gluon Plasma Formation*, *Phys. Lett. B* **178** (1986) 416.

[48] **WA97** Collaboration, *Strangeness enhancement at mid-rapidity in Pb-Pb collisions at 158 GeV/c*, *J. Phys. G* **25** (1999) 181.

[49] **STAR** Collaboration, *Evidence from $d + \mathrm{Au}$ Measurements for Final-State Suppression of High-p_T Hadrons in $\mathrm{Au} + \mathrm{Au}$ Collisions at RHIC*, *Phys. Rev. Lett.* **91** (2003) 072304.

[50] **PHENIX** Collaboration, *Suppression Pattern of Neutral Pions at High Transverse Momentum in* $\mathrm{Au} + \mathrm{Au}$ *Collisions at* $\sqrt{s_{NN}} = 200$ GeV *and Constraints on Medium Transport Coefficients*, *Phys. Rev. Lett.* **101** (2008) 232301.

[51] J. D. Bjorken, *Energy Loss of Energetic Partons in Quark - Gluon Plasma: Possible Extinction of High* p_T *Jets in Hadron - Hadron Collisions*, Aug, 1982. FERMILAB-PUB-82-59-THY, https://cds.cern.ch/record/141477.

[52] U. Heinz and R. Snellings, *Collective Flow and Viscosity in Relativistic Heavy-Ion Collisions*, *Ann. Rev. Nucl. Part. Sci.* **63** (2013) 123 [https://doi.org/10.1146/annurev-nucl-102212-170540].

[53] E. Shuryak, *Physics of Strongly coupled Quark-Gluon Plasma*, *Prog. Part. Nucl. Phys.* **62** (2009) 48 [0807.3033].

[54] R. Averbeck, J. W. Harris, and B. Schenke, *Heavy-Ion Physics at the LHC*, in *The Large Hadron Collider: Harvest of Run 1*, T. Schörner-Sadenius, ed., (Cham), pp. 355–420, Springer International Publishing (2015).

[55] H. Paukkunen, *Nuclear PDFs in the beginning of the LHC era*, *Nucl. Phys. A* **926** (2014) 24.

[56] V. Emel'yanov, A. Khodinov, S. R. Klein, and R. Vogt, *The Effect of shadowing on initial conditions, transverse energy and hard probes in ultrarelativistic heavy ion collisions*, *Phys. Rev. C* **61** (2000) 044904 [hep-ph/9909427].

[57] D. F. Geesaman, K. Saito, and A. W. Thomas, *The Nuclear EMC Effect*, *Ann. Rev. Nucl. Part. Sci.* **45** (1995) 337 [https://doi.org/10.1146/annurev.ns.45.120195.002005].

[58] K. J. Eskola, P. Paakkinen, H. Paukkunen, and C. A. Salgado, *EPPS16: Nuclear parton distributions with LHC data*, *Eur. Phys. J. C* **77** (2017) 163 [1612.05741].

[59] K. Kovarik et al., *nCTEQ15 - Global analysis of nuclear parton distributions with uncertainties in the CTEQ framework*, *Phys. Rev. D* **93** (2016) 085037 [1509.00792].

[60] G. Graziani, *Results on heavy ion physics at LHCb*, *Journal of Physics: Conference Series* **1271** (2019) 012008.

[61] **CMS** Collaboration, *Observation of long-range, near-side angular correlations in proton-proton collisions at the LHC*, *JHEP* **2010** (2010) 91.

[62] **CMS** Collaboration, *Measurement of long-range near-side two-particle angular correlations in pp collisions at* $\sqrt{s}$ *= 13 TeV*, *Phys. Rev. Lett.* **116** (2016) 172302 [1510.03068].

[63] **CMS** Collaboration, *Multiplicity and transverse momentum dependence of two- and four-particle correlations in pPb and PbPb collisions*, *Phys. Lett. B* **724** (2013) 213.

[64] S. H. Lim et al., *Examination of flow and nonflow factorization methods in small collision systems*, *Phys. Rev. C* **100** (2019) 024908.

[65] J. L. Nagle and W. A. Zajc, *Small System Collectivity in Relativistic Hadronic and Nuclear Collisions*, *Ann. Rev. Nucl. Part. Sci.* **68** (2018) 211 [1801.03477].

[66] B. Schenke, C. Shen, and P. Tribedy, *Running the gamut of high energy nuclear collisions*, *Phys. Rev. C* **102** (2020) 044905.

[67] X. Dong and V. Greco, *Heavy quark production and properties of Quark–Gluon Plasma*, *Prog. Part. Nucl. Phys.* **104** (2019) 97.

[68] J. C. Collins, D. E. Soper, and G. F. Sterman, *Heavy Particle Production in High-Energy Hadron Collisions*, *Nucl. Phys. B* **263** (1986) 37.

[69] H. Fujii, F. Gelis, and R. Venugopalan, *Quark pair production in high energy pA collisions: General features*, *Nucl. Phys. A* **780** (2006) 146.

[70] F. Arleo and S. Peigné, *Heavy-quarkonium suppression in p-A collisions from parton energy loss in cold QCD matter*, *JHEP* **2013** (2013) 122.

[71] R. Vogt, *Cold Nuclear Matter Effects on J/ψ and Υ Production at the LHC*, *Phys. Rev. C* **81** (2010) 044903 [1003.3497].

[72] E. G. Ferreiro, *Excited charmonium suppression in proton-nucleus collisions as a consequence of comovers*, *Phys. Lett. B* **749** (2015) 98 [1411.0549].

[73] **ALICE** Collaboration, *Charm-quark fragmentation fractions and production cross section at midrapidity in pp collisions at the LHC*, *Phys. Rev. D* **105** (2022) L011103 [2105.06335].

[74] **ALICE** Collaboration, *Measurement of beauty and charm production in pp collisions at $\sqrt{s}$ = 5.02 TeV via non-prompt and prompt D mesons*, *JHEP* **05** (2021) 220 [2102.13601].

[75] J.-P. Lansberg, *New Observables in Inclusive Production of Quarkonia*, *Phys. Rept.* **889** (2020) 1 [1903.09185].

[76] J. C. Collins, D. E. Soper, and G. F. Sterman, *Factorization of Hard Processes in QCD*, *Adv. Ser. Direct. High Energy Phys.* **5** (1989) 1 [hep-ph/0409313].

[77] M. L. Mangano, *Two lectures on heavy quark production in hadronic collisions*, *Proc. Int. Sch. Phys. Fermi* **137** (1998) 95 [hep-ph/9711337].

[78] A. Kusina et al., *Hybrid scheme for heavy flavors: Merging the fixed flavor number scheme and variable flavor number scheme*, *Phys. Rev. D* **88** (2013) 074032 [1306.6553].

[79] M. Cacciari, M. Greco, and P. Nason, *The P(T) spectrum in heavy flavor hadroproduction*, *JHEP* **05** (1998) 007.

[80] B. A. Kniehl, G. Kramer, I. Schienbein, and H. Spiesberger, *Inclusive $D^{*\pm}$ production in $p\bar{p}$ collisions with massive charm quarks*, *Phys. Rev. D* **71** (2005) 014018 [hep-ph/0410289].

[81] T. Sjostrand, S. Mrenna, and P. Z. Skands, *PYTHIA 6.4 Physics and Manual*, *JHEP* **05** (2006) 026.

[82] M. Bahr et al., *Herwig++ Physics and Manual*, *Eur. Phys. J. C* **58** (2008) 639 [0803.0883].

[83] T. Sjostrand, *Jet Fragmentation of Nearby Partons*, *Nucl. Phys. B* **248** (1984) 469.

[84] B. Andersson, G. Gustafson, G. Ingelman, and T. Sjostrand, *Parton Fragmentation and String Dynamics*, *Phys. Rept.* **97** (1983) 31.

[85] A. Kupco, *Cluster hadronization in HERWIG 5.9*, in *Workshop on Monte Carlo Generators for HERA Physics (Plenary Starting Meeting)*, pp. 292–300, 4, 1998 [hep-ph/9906412].

[86] **CMS** Collaboration, *Measurement of the total and differential inclusive B^+ hadron cross sections in pp collisions at $\sqrt{s}$ = 13 TeV*, *Phys. Lett. B* **771** (2017) 435 [1609.00873].

[87] **ATLAS** Collaboration, *Measurement of the inclusive and dijet cross-sections of b^- jets in pp collisions at $\sqrt{s} = 7$ TeV with the ATLAS detector*, *Eur. Phys. J. C* **71** (2011) 1846 [1109.6833].

[88] **ALICE** Collaboration, *Measurement of electrons from beauty hadron decays in pp collisions at $\sqrt{s}$ = 7 TeV*, *Phys. Lett. B* **721** (2013) 13.

[89] **ALICE** Collaboration, *Corrigendum to "Measurement of electrons from beauty hadron decays in pp collisions at $\sqrt{s}$ = 7 TeV" [Phys. Lett. B 721 (1-3) (2013) 13-23] and "Beauty production in pp collisions at $\sqrt{s}$ = 2.76 TeV measured via semi-electronic decays" [Phys. Lett. B 738 (2014) 97-108]*, *Phys. Lett. B* **763** (2016) 507.

[90] **LHCb** Collaboration, *Measurement of J/ψ production cross-sections in pp collisions at $\sqrt{s}$ = 5 TeV*, *JHEP* **11** (2021) 181 [2109.00220].

[91] **LHCb** Collaboration, *Measurement of b-hadron production fractions in 7 TeV pp collisions*, *Phys. Rev. D* **85** (2012) 032008 [1111.2357].

[92] **LHCb** Collaboration, *Measurement of b hadron fractions in 13 TeV pp collisions*, *Phys. Rev. D* **100** (2019) 031102 [1902.06794].

[93] G. Eichmann et al., *Four-Quark States from Functional Methods*, *Few-Body Systems* **61** (2020) 38.

[94] J. J. Aubert et al., *Experimental Observation of a Heavy Particle J*, *Phys. Rev. Lett.* **33** (1974) 1404.

[95] J. E. Augustin et al., *Discovery of a Narrow Resonance in e^+e^- Annihilation*, *Phys. Rev. Lett.* **33** (1974) 1406.

[96] S. Okubo, *ϕ-meson and unitary symmetry model*, *Phys. Lett.* **5** (1963) 165.

[97] G. Zweig, *An SU(3) model for strong interaction symmetry and its breaking. Version 2*, in *DEVELOPMENTS IN THE QUARK THEORY OF HADRONS. VOL. 1. 1964 - 1978*, D. B. Lichtenberg and S. P. Rosen, eds., pp. 22–101 (1964).

[98] J. Iizuka, *A Systematics and Phenomenology of Meson Family**, *Progress of Theoretical Physics Supplement* **37-38** (1966) 21.

[99] E. Eichten et al., *Spectrum of Charmed Quark-Antiquark Bound States*, *Phys. Rev. Lett.* **34** (1975) 369.

[100] E. Eichten et al., *Erratum: Spectrum of Charmed Quark-Antiquark Bound States.*, *Phys. Rev. Lett.* **36** (1976) 1276.

[101] R. Baier and R. Ruckl, *Hadronic Production of J/ψ and Υ: Transverse Momentum Distributions*, *Phys. Lett. B* **102** (1981) 364.

[102] H. Fritzsch, *Producing heavy quark flavors in hadronic collisions — A test of quantum chromodynamics*, *Phys. Lett. B* **67** (1977) 217.

[103] F. Halzen, *CVC for gluons and hadroproduction of quark flavours*, *Phys. Lett. B* **69** (1977) 105.

[104] J. F. Amundson, O. J. P. Eboli, E. M. Gregores, and F. Halzen, *Colorless states in perturbative QCD: Charmonium and rapidity gaps*, *Phys. Lett. B* **372** (1996) 127 [hep-ph/9512248].

[105] **Quarkonium Working Group** Collaboration, *Heavy quarkonium physics*, hep-ph/0412158.

[106] G. T. Bodwin, E. Braaten, and G. P. Lepage, *Rigorous QCD analysis of inclusive annihilation and production of heavy quarkonium*, *Phys. Rev. D* **51** (1995) 1125 [hep-ph/9407339].

[107] **LHCb** Collaboration, *Measurement of the relative rate of prompt χ_{c0}, χ_{c1} and χ_{c2} production at $\sqrt{s} = 7$TeV*, *JHEP* **10** (2013) 115 [1307.4285].

[108] **ALICE** Collaboration, *Prompt and non-prompt J/ψ production cross sections at midrapidity in proton-proton collisions at $\sqrt{s}$ = 5.02 and 13 TeV*, 2108.02523.

[109] **ATLAS** Collaboration, *Measurement of quarkonium production in proton–lead and proton–proton collisions at 5.02 TeV with the ATLAS detector*, *Eur. Phys. J. C* **78** (2018) 171.

[110] **CMS** Collaboration, *Measurement of prompt and nonprompt J/ψ production in pp and pPb collisions at $\sqrt{s_{\mathrm{NN}}}$ = 5.02 TeV*, *Eur. Phys. J. C* **77** (2017) 269.

[111] **CMS** Collaboration, *Measurement of quarkonium production cross sections in pp collisions at $\sqrt{s_{\mathrm{NN}}}$ = 13 TeV*, *Phys. Lett. B* **780** (2018) 251.

[112] M. Butenschön and B. A. Kniehl, *Reconciling J/ψ Production at HERA, RHIC, Tevatron, and LHC with Nonrelativistic QCD Factorization at Next-to-Leading Order*, *Phys. Rev. Lett.* **106** (2011) 022003.

[113] Y.-Q. Ma, K. Wang, and K.-T. Chao, *$J/\psi(\psi')$ production at the Tevatron and LHC at $O(\alpha_s^4 v^4)$ in nonrelativistic QCD*, *Phys. Rev. Lett.* **106** (2011) 042002 [1009.3655].

[114] S. P. Baranov and A. V. Lipatov, *Are there any challenges in the charmonia production and polarization at the LHC?*, *Phys. Rev. D* **100** (2019) 114021 [1906.07182].

[115] Y.-Q. Ma and R. Venugopalan, *Comprehensive Description of J/ψ Production in Proton-Proton Collisions at Collider Energies*, *Phys. Rev. Lett.* **113** (2014) 192301 [1408.4075].

[116] V. Cheung and R. Vogt, *Production and polarization of prompt J/ψ in the improved color evaporation model using the k_T-factorization approach*, *Phys. Rev. D* **98** (2018) 114029 [1808.02909].

[117] H. Han et al., *$\Upsilon(nS)$ and $\chi_b(nP)$ production at hadron colliders in nonrelativistic QCD*, *Phys. Rev. D* **94** (2016) 014028 [1410.8537].

[118] **LHCb** Collaboration, *Measurement of J/ψ polarization in pp collisions at $\sqrt{s} = 7$ TeV*, *Eur. Phys. J. C* **73** (2013) 2631 [1307.6379].

[119] **ALICE** Collaboration, *Measurement of the inclusive J/ψ polarization at forward rapidity in pp collisions at $\sqrt{s}$ = 8 TeV*, *Eur. Phys. J. C* **78** (2018) 562.

[120] A. Andronic et al., *Heavy-flavour and quarkonium production in the LHC era: from proton–proton to heavy-ion collisions*, *Eur. Phys. J. C* **76** (2016) 107.

[121] **ALICE** Collaboration, *Measurement of transverse energy at midrapidity in Pb-Pb collisions at $\sqrt{s_{\rm NN}} = 2.76$ TeV*, *Phys. Rev. C* **94** (2016) 034903 [1603.04775].

[122] F.-M. Liu and S.-X. Liu, *Quark-gluon plasma formation time and direct photons from heavy ion collisions*, *Phys. Rev. C* **89** (2014) 034906 [1212.6587].

[123] G. Martinez, *Advances in Quark Gluon Plasma*, 4, 2013 [1304.1452].

[124] Y. L. Dokshitzer and D. E. Kharzeev, *Heavy quark colorimetry of QCD matter*, *Phys. Lett. B* **519** (2001) 199 [hep-ph/0106202].

[125] R. Snellings, *Elliptic flow: a brief review*, *New Journal of Physics* **13** (2011) 055008.

[126] **ALICE** Collaboration, *Prompt D^0, D^+, and D^{*+} production in Pb–Pb collisions at $\sqrt{s_{\rm NN}}$ = 5.02 TeV*, *JHEP* **01** (2022) 174 [2110.09420].

[127] **ALICE** Collaboration, *Transverse momentum spectra and nuclear modification factors of charged particles in pp, p–Pb and Pb–Pb collisions at the LHC*, *JHEP* **2018** (2018) 13.

[128] **ALICE** Collaboration, *Production of charged pions, kaons, and (anti-)protons in Pb–Pb and inelastic pp collisions at $\sqrt{s_{NN}} = 5.02$ TeV*, *Phys. Rev. C* **101** (2020) 044907.

[129] **ALICE** Collaboration, *Centrality and transverse momentum dependence of inclusive J/ψ production at midrapidity in Pb–Pb collisions at* $\sqrt{s_{\rm NN}}$ *= 5.02 TeV*, Phys. Lett. B **805** (2020) 135434.

[130] **CMS** Collaboration, *Measurement of prompt and nonprompt charmonium suppression in PbPb collisions at 5.02 TeV*, *Eur. Phys. J. C* **78** (2018) 509.

[131] **ALICE** Collaboration, *Anisotropic flow of identified particles in Pb-Pb collisions at* $\sqrt{s_{\rm NN}} = 5.02$ *TeV*, *JHEP* **09** (2018) 006 [1805.04390].

[132] **ALICE** Collaboration, *Transverse-momentum and event-shape dependence of D-meson flow harmonics in Pb–Pb collisions at* $\sqrt{s_{NN}}$ *= 5.02 TeV*, Phys. Lett. B **813** (2021) 136054 [2005.11131].

[133] **ALICE** Collaboration, *J/ψ elliptic and triangular flow in Pb-Pb collisions at* $\sqrt{s_{\rm NN}}$ *= 5.02 TeV*, *JHEP* **10** (2020) 141 [2005.14518].

[134] **ALICE** Collaboration, *Elliptic Flow of Electrons from Beauty-Hadron Decays in Pb-Pb Collisions at* $\sqrt{s_{NN}}$ *= 5.02 TeV*, Phys. Rev. Lett. **126** (2021) 162001 [2005.11130].

[135] **ALICE** Collaboration, *Measurement of* $\Upsilon(1S)$ *Elliptic Flow at Forward Rapidity in Pb-Pb Collisions at* $\sqrt{s_{NN}} = 5.02$ TeV, Phys. Rev. Lett. **123** (2019) 192301.

[136] M. He and R. Rapp, *Hadronization and Charm-Hadron Ratios in Heavy-Ion Collisions*, Phys. Rev. Lett. **124** (2020) 042301.

[137] P. Braun-Munzinger and J. Stachel, *(Non)thermal aspects of charmonium production and a new look at* J/ψ *suppression*, Phys. Lett. B **490** (2000) 196.

[138] R. L. Thews, M. Schroedter, and J. Rafelski, *Enhanced* J/ψ *production in deconfined quark matter*, Phys. Rev. C **63** (2001) 054905.

[139] S. Digal, P. Petreczky, and H. Satz, *Quarkonium feed-down and sequential suppression*, Phys. Rev. D **64** (2001) 094015.

[140] F. Karsch, D. Kharzeev, and H. Satz, *Sequential charmonium dissociation*, Phys. Lett. B **637** (2006) 75 [hep-ph/0512239].

[141] T. Matsui and H. Satz, J/ψ *suppression by quark-gluon plasma formation*, Phys. Lett. B **178** (1986) 416.

[142] **CMS** Collaboration, *Nuclear modification of* Υ *states in pPb collisions at* $\sqrt{s_{\rm NN}}$ *= 5.02 TeV*, 2202.11807.

[143] **ALICE** Collaboration, *J/ψ suppression at forward rapidity in Pb–Pb collisions at* $\sqrt{s_{\rm NN}} = 5.02$ *TeV*, Phys. Lett. B **766** (2017) 212 [1606.08197].

[144] **PHENIX** Collaboration, *J/ψ suppression at forward rapidity in Au+Au collisions at $\sqrt{s_{NN}} = 200$ GeV*, *Phys. Rev. C* **84** (2011) 054912 [1103.6269].

[145] **CMS** Collaboration, *Measurement of nuclear modification factors of Υ(1S), Υ(2S), and Υ(3S) mesons in PbPb collisions at $\sqrt{s_{\mathrm{NN}}}$ = 5.02 TeV*, *Phys. Lett. B* **790** (2019) 270 [1805.09215].

[146] H.-S. Shao, *HELAC-Onia: An automatic matrix element generator for heavy quarkonium physics*, *Comput. Phys. Commun.* **184** (2013) 2562 [1212.5293].

[147] J.-P. Lansberg and H.-S. Shao, *Towards an automated tool to evaluate the impact of the nuclear modification of the gluon density on quarkonium, D and B meson production in proton-nucleus collisions*, *Eur. Phys. J. C* **77** (2017) 1 [1610.05382].

[148] H.-S. Shao, *HELAC-Onia 2.0: an upgraded matrix-element and event generator for heavy quarkonium physics*, *Comput. Phys. Commun.* **198** (2016) 238 [1507.03435].

[149] F. Gelis, E. Iancu, J. Jalilian-Marian, and R. Venugopalan, *The Color Glass Condensate*, *Ann. Rev. Nucl. Part. Sci.* **60** (2010) 463 [1002.0333].

[150] J. W. Cronin et al., *Production of hadrons at large transverse momentum at 200, 300, and 400 GeV*, *Phys. Rev. D* **11** (1975) 3105.

[151] **LHCb** Collaboration, *Measurement of B^+, B^0 and Λ_b^0 production in pPb collisions at $\sqrt{s_{\mathrm{NN}}} = 8.16$ TeV*, *Phys. Rev. D* **99** (2019) 052011.

[152] **ALICE** Collaboration, *Measurement of electrons from beauty-hadron decays in p–Pb collisions at $\sqrt{s_{\mathrm{NN}}} = 5.02$ TeV and Pb–Pb collisions at $\sqrt{s_{\mathrm{NN}}} = 2.76$ TeV*, *JHEP* **07** (2017) 052 [1609.03898].

[153] **ALICE** Collaboration, *Measurement of nuclear effects on $\psi(2S)$ production in p-Pb collisions at $\sqrt{s_{\mathrm{NN}}} = 8.16$ TeV*, *JHEP* **07** (2020) 237 [2003.06053].

[154] **ALICE** Collaboration, *Υ production in p–Pb collisions at $\sqrt{s_{\mathrm{NN}}}$ = 8.16 TeV*, *Phys. Lett. B* **806** (2020) 135486.

[155] E. G. Ferreiro and J.-P. Lansberg, *Is bottomonium suppression in proton-nucleus and nucleus-nucleus collisions at LHC energies due to the same effects?*, *JHEP* **10** (2018) 094 [1804.04474].

[156] E. G. Ferreiro, *Global description of bottomonium suppression in proton-nucleus and nucleus-nucleus collisions at LHC energies*, *PoS* **DIS2018** (2018) 130 [1810.12874].

[157] **PHENIX** Collaboration, *Creation of quark–gluon plasma droplets with three distinct geometries*, *Nature Physics* **15** (2019) 214.

[158] **CMS** Collaboration, *Studies of charm and beauty hadron long-range correlations in pp and pPb collisions at LHC energies*, *Phys. Lett. B* **813** (2021) 136036.

[159] C. Zhang et al., *Elliptic Flow of Heavy Quarkonia in pA Collisions*, *Phys. Rev. Lett.* **122** (2019) 172302 [1901.10320].

[160] C. Zhang et al., *Collectivity of heavy mesons in proton-nucleus collisions*, *Phys. Rev. D* **102** (2020) 034010 [2002.09878].

[161] L. R. Evans and P. Bryant, *LHC Machine*, *JINST* **3** (2008) S08001.

[162] E. Mobs, *The CERN accelerator complex - August 2018*, Aug, 2018. General Photo, https://cds.cern.ch/record/2636343.

[163] M. Benedikt et al., *LHC Design Report*, CERN Yellow Reports: Monographs, CERN (2004), 10.5170/CERN-2004-003-V-3.

[164] M. Vretenar et al., *LINAC4 design report*, CERN Yellow Reports: Monographs, CERN (2020), 10.23731/CYRM-2020-006.

[165] K. Hanke, *Past and present operation of the CERN PS Booster*, *Int. J. Mod. Phys. A* **28** (2013) 1330019.

[166] J.-P. Burnet et al., *Fifty years of the CERN Proton Synchrotron: Volume 1*, CERN Yellow Reports: Monographs, CERN (2011), 10.5170/CERN-2011-004.

[167] L. Dumas et al., *Operation of the GTS-LHC Source for the Hadron Injector at CERN*, Tech. Rep. CERN-LHC-PROJECT-Report-985, CERN (Jan, 2007).

[168] M. Chanel, *LEIR: The low energy ion ring at CERN*, *Nucl. Instrum. Meth. A* **532** (2002) 137.

[169] N. Angert et al., *CERN heavy-ion facility design report*, CERN Yellow Reports: Monographs, CERN, Geneva (1993), 10.5170/CERN-1993-001.

[170] **ALICE** Collaboration, *The ALICE experiment at the CERN LHC*, *JINST* **3** (2008) S08002.

[171] **ATLAS** Collaboration, *The ATLAS Experiment at the CERN Large Hadron Collider*, *JINST* **3** (2008) S08003.

[172] **CMS** Collaboration, *The CMS Experiment at the CERN LHC*, *JINST* **3** (2008) S08004.

[173] **LHCb** Collaboration, *The LHCb Detector at the LHC*, *JINST* **3** (2008) S08005.

[174] J. Jowett, *Colliding Heavy Ions in the LHC*, in *9th International Particle Accelerator Conference*, June, 2018, DOI.

[175] **ALICE** Collaboration, *Centrality Dependence of the Charged-Particle Multiplicity Density at Midrapidity in Pb-Pb Collisions at $\sqrt{s_{NN}} = 5.02$ TeV*, *Phys. Rev. Lett.* **116** (2016) 222302.

[176] **ALICE** Collaboration, *A schematics of the ALICE detector*, May, 2017. ALICE-PHO-SKE-2017-001, https://cds.cern.ch/record/2263642.

[177] **L3** Collaboration, *The construction of the L3 experiment*, *Nucl. Instrum. Meth. A* **289** (1990) 35.

[178] G. Volpe, *PID performance of the High Momentum Particle IDentification (HMPID) detector during LHC-Run 2*, *Nucl. Instrum. Meth. A* **952** (2020) 161803.

[179] D. Attié, *TPC review*, *Nucl. Instrum. Meth. A* **598** (2009) 89.

[180] D. R. Nygren, *Proposal to investigate the feasibility of a novel concept in particle detection*, 1974. https://inspirehep.net/literature/1365360.

[181] **ALICE** Collaboration, G. Dellacasa et al., *ALICE: Technical design report of the time projection chamber*, 1, 2000. https://cds.cern.ch/record/451098.

[182] J. Alme et al., *The ALICE TPC, a large 3-dimensional tracking device with fast readout for ultra-high multiplicity events*, *Nucl. Instrum. Meth. A* **622** (2010) 316.

[183] E. Hellbär, *The ALICE TPC: Optimization of the Performance in Run 2 and Developments for the Future*, *PoS* **LHCP2019** (2019) 240.

[184] E. Hellbär, *Ion Movement and Space-charge Distortions in the ALICE TPC*, Master's thesis, Goethe-Universität, Frankfurt am Main, 2015.

[185] **ALICE** Collaboration, *Upgrade of the ALICE Time Projection Chamber*, Tech. Rep. CERN-LHCC-2013-020 (Oct, 2013).

[186] W. Blum, W. Riegler, and L. Rolandi, *Particle Detection with Drift Chambers*, Springer Berlin Heidelberg, Berlin, Heidelberg (2008), 10.1007/978-3-540-76684-1.

[187] **ALICE** Collaboration, *TPC dE/dx distribution for p-Pb collisions*, Nov, 2013. ALI-PERF-60751, https://alice-figure.web.cern.ch/node/5321.

[188] C. Lippmann, *Particle identification*, *Nucl. Instrum. Meth. A* **666** (2012) 148.

[189] **ALICE** Collaboration, *Alignment of the ALICE Inner Tracking System with cosmic-ray tracks*, *JINST* **5** (2010) P03003.

[190] S. Beolè et al., *The ALICE silicon drift detectors: Production and assembly*, *Nucl. Instrum. Meth. A* **582** (2007) 733.

[191] **ALICE** Collaboration, *Performance of the ALICE Experiment at the CERN LHC*, *Int. J. Mod. Phys. A* **29** (2014) 1430044.

[192] A. Maire, *Track reconstruction principle in ALICE for LHC run I and run II.*, Oct, 2011. General Photo, https://cds.cern.ch/record/1984041.

[193] Y. Belikov, K. Safarík, and B. Batyunya, *Kalman Filtering Application for Track Recognition and Reconstruction in ALICE Tracking System*, Tech. Rep. CERN-ALICE-INT-1997-24, CERN (1997).

[194] Z. Drasal and W. Riegler, *An extension of the Gluckstern formulae for multiple scattering: Analytic expressions for track parameter resolution using optimum weights*, Nucl. Instrum. Meth. A **910** (2018) 127.

[195] R. Veenhof, *Garfield-simulation of gaseous detectors, User Guide*, 2010.

[196] **ALICE** Collaboration, *The ALICE Transition Radiation Detector: Construction, operation, and performance*, Nucl. Instrum. Meth. A **881** (2018) 88.

[197] A. Andronic, *Electron identification performance with ALICE TRD prototypes*, Nucl. Instrum. Meth. A **522** (2004) 40.

[198] **ALICE** Collaboration, *Particle Identification with the ALICE Transition Radiation Detector*, Nucl. Instrum. Meth. A **766** (2014) 292 [1402.3508].

[199] J. Stiller, *Gain Calibration of the ALICE TRD using the Decay of 83mKr and Alignment of the ALICE TRD*, Diploma's thesis, Ruprecht-Karls-Universität Heidelberg, 2011.

[200] V. Angelov, *Design and performance of the ALICE TRD front-end electronics*, Nucl. Instrum. Meth. A **563** (2006) 317.

[201] J. Klein, *Commisioning of and Preparations for Physics with the Transition Radiation Detector in A Large Ion Collider Experiment at CERN*, Diploma's thesis, Ruprecht-Karls-Universität Heidelberg, 2008.

[202] J. de Cuveland, *A Track Reconstructing Low-latency Trigger Processor for High-energy Physics*, Doctoral thesis, Ruprecht-Karls-Universität Heidelberg, 2009.

[203] R. Bailhache and C. Lippmann, *New test beam results with prototypes of the ALICE TRD*, Nucl. Instrum. Meth. A **563** (2006) 310.

[204] O. Schmidt, *Simulation and commissioning of the rejection of late conversions in the TRD triggers of ALICE*, Master's thesis, Ruprecht-Karls-Universität Heidelberg, 2016.

[205] Y. C. Pachmayer, M. Kim, M. K. Köhler, and J. Stachel, "Measurement of J/ψ in TRD-triggered p-Pb collisions at 8.16 TeV with ALICE at the LHC." ALICE Internal Note ANA-1136, https://alice-notes.web.cern.ch/node/1136.

[206] **ALICE** Collaboration, *ALICE luminosity determination for p-Pb collisions at* $\sqrt{s_{\mathrm{NN}}} = 8.16$ *TeV*, Apr, 2018. https://cds.cern.ch/record/2314660.

[207] T. Pierog et al., *EPOS LHC: Test of collective hadronization with data measured at the CERN Large Hadron Collider*, Phys. Rev. C **92** (2015) 034906.

[208] **ALICE** Collaboration, *Inclusive J/ψ production at forward and backward rapidity in p-Pb collisions at* $\sqrt{s_{\mathrm{NN}}}$ *= 8.16 TeV*, JHEP **07** (2018) 160.

[209] D. J. Lange, *The EvtGen particle decay simulation package*, Nucl. Instrum. Meth. A **462** (2001) 152.

[210] E. Barberio and Z. Was, *PHOTOS: A Universal Monte Carlo for QED radiative corrections. Version 2.0*, Comput. Phys. Commun. **79** (1994) 291.

[211] R. Brun et al., *GEANT 3: user's guide Geant 3.10, Geant 3.11; rev version*, CERN, Geneva (1987).

[212] T. Dahms, *Measurement of photons via conversion pairs with the PHENIX experiment at RHIC*, Master's thesis, Stony Brook University, 2005.

[213] P. G. Zamora, *Measurement of π^0 meson properties through its Dalitz decay channel in pp and p-Pb collisions with the ALICE experiment at the LHC*, Doctoral thesis, UCM, Madrid, Dept. Phys., Madrid, CIEMAT, 2016.

[214] **CDF** Collaboration, *Measurement of the J/ψ meson and $b-$hadron production cross sections in $p\bar{p}$ collisions at $\sqrt{s} = 1960$ GeV*, Phys. Rev. D **71** (2005) 032001 [hep-ex/0412071].

[215] Y. C. Pachmayer and M. Kim, "Measurement of non-prompt J/ψ in p-Pb collisions at 8.16 TeV." ALICE Internal Note ANA-1103, https://alice-notes.web.cern.ch/node/1103.

[216] J. E. Gaiser, *Charmonium Spectroscopy From Radiative Decays of the J/ψ and ψ'*, Doctoral thesis, Stanford Linear Accelerator Center, Stanford University, 8, 1982.

[217] **LHCb** Collaboration, *Measurement of b hadron fractions in 13 TeV pp collisions*, Phys. Rev. D **100** (2019) 031102 [1902.06794].

[218] F. James and M. Roos, *Minuit: A System for Function Minimization and Analysis of the Parameter Errors and Correlations*, Comput. Phys. Commun. **10** (1975) 343.

[219] W. Verkerke and D. P. Kirkby, *The RooFit toolkit for data modeling*, *eConf* **C0303241** (2003) MOLT007.

[220] **LHCb** Collaboration, *Prompt and nonprompt J/ψ production and nuclear modification in pPb collisions at $\sqrt{s_{NN}} = 8.16$ TeV*, Phys. Lett. B **774** (2017) 159 [1706.07122].

[221] **ALICE** Collaboration, *Inclusive, prompt and non-prompt J/ψ production at midrapidity in $p-$Pb collisions at $\sqrt{s_{\rm NN}} = 5.02$ TeV*, 2105.04957.

[222] **ALICE** Collaboration, *Beauty production in pp collisions at $\sqrt{s}$ = 2.76 tev measured via semi-electronic decays*, Phys. Lett. B **738** (2014) 97.

[223] **ALICE** Collaboration, *Measurement of electrons from beauty hadron decays in pp collisions at $\sqrt{s}$ = 7 TeV*, Phys. Lett. B **721** (2013) 13.

[224] **ALICE** Collaboration, *Corrigendum to "measurement of electrons from beauty hadron decays in pp collisions at $\sqrt{s}$ = 7 tev" [phys. lett. b 721 (1-3) (2013) 13-23] and "beauty production in pp*

collisions at $\sqrt{s}$ = 2.76 tev measured via semi-electronic decays" [phys. lett. b 738 (2014) 97-108], Phys. Lett. B **763** (2016) 507.

[225] **ATLAS** Collaboration, *Measurement of differential J/ψ production cross sections and forward-backward ratios in p + Pb collisions with the ATLAS detector*, Phys. Rev. C **92** (2015) 034904 [1505.08141].

[226] **ALICE** Collaboration, *Measurement of prompt J/ψ and beauty hadron production cross sections at mid-rapidity in pp collisions at $\sqrt{s} = 7$ TeV*, JHEP **11** (2012) 065 [1205.5880].

[227] **ATLAS** Collaboration, *Measurement of the differential cross-sections of prompt and non-prompt production of J/ψ and $\psi(2S)$ in pp collisions at $\sqrt{s} = 7$ and 8 TeV with the ATLAS detector*, Eur. Phys. J. C **76** (2016) 283 [1512.03657].

[228] **ALICE** Collaboration, *Inclusive, prompt and non-prompt J/ψ production at midrapidity in p–Pb collisions at $\sqrt{s_{NN}} = 5.02$ TeV*, 2105.04957.

[229] **LHCb** Collaboration, *Measurement of forward J/ψ production cross-sections in pp collisions at $\sqrt{s}$ = 13 TeV*, JHEP **10** (2015) 172.

[230] **LHCb** Collaboration, *Erratum to: Measurement of forward J/ψ production cross-sections in pp collisions at $\sqrt{s}$ = 13 TeV*, JHEP **2017** (2017) 63.

[231] P. Duwentäster et al., "Impact of heavy quark and quarkonium data on nuclear gluon PDFs." Private communication. Paper in preparation.

[232] P. Duwentäster, "Constraining the nuclear gluon PDF with quarkonium production data." https://indico.cern.ch/event/1084752/contributions/4632844/attachments/2369883/4047366/nPDF_Quarkonia.pdf. Contribution at *Quarkonia As Tools 2022.*

[233] ***ALICE*** *Collaboration,* Inclusive J/ψ production at forward and backward rapidity in p-Pb collisions at $\sqrt{s_{NN}}$ = 8.16 TeV*,* JHEP ***07*** *(2018) 160 [1805.04381].*

[234] ***CMS*** *Collaboration,* Measurement of prompt and nonprompt J/ψ production in pp and pPb collisions at $\sqrt{s_{NN}} = 5.02$ TeV*,* Eur. Phys. J. C ***77*** *(2017) 269 [1702.01462].*

[235] ***CMS*** *Collaboration,* Prompt and Non-Prompt J/ψ Production in pp Collisions at $\sqrt{s} = 7$ TeV*,* Eur. Phys. J. C ***71*** *(2011) 1575 [1011.4193].*

[236] A. Kusina, J.-P. Lansberg, I. Schienbein, and H.-S. Shao, Gluon Shadowing in Heavy-Flavor Production at the LHC*,* Phys. Rev. Lett. ***121*** *(2018) 052004 [1712.07024].*

[237] J. L. Albacete et al., Predictions for Cold Nuclear Matter Effects in p+Pb Collisions at $\sqrt{s_{NN}} = 8.16$ TeV*,* Nucl. Phys. A ***972*** *(2018) 18 [1707.09973].*

[238] X. Du and R. Rapp, In-Medium Charmonium Production in Proton-Nucleus Collisions*,* JHEP ***03*** *(2019) 015 [1808.10014].*

[239] **LHCb** *Collaboration,* Study of prompt D^0 meson production in pPb collisions at $\sqrt{s_{NN}} = 5$ TeV, JHEP **10** (2017) 090 [1707.02750].

[240] *K. J. Eskola, H. Paukkunen, and C. A. Salgado,* EPS09: A New Generation of NLO and LO Nuclear Parton Distribution Functions, JHEP **04** (2009) 065 [0902.4154].

[241] *F. Arleo, R. Kolevatov, S. Peigné, and M. Rustamova,* Centrality and $p_\perp$ dependence of J/ψ suppression in proton-nucleus collisions from parton energy loss, JHEP **05** (2013) 155 [1304.0901].

[242] *Y.-Q. Ma, R. Venugopalan, and H.-F. Zhang,* J/ψ production and suppression in high energy proton-nucleus collisions, Phys. Rev. D **92** (2015) 071901 [1503.07772].

[243] *B. Chen, T. Guo, Y. Liu, and P. Zhuang,* Cold and Hot Nuclear Matter Effects on Charmonium Production in p+Pb Collisions at LHC Energy, Phys. Lett. B **765** (2017) 323 [1607.07927].

[244] *M. Cacciari et al.,* Theoretical predictions for charm and bottom production at the LHC, JHEP **10** (2012) 137 [1205.6344].

[245] *D. de Florian, R. Sassot, P. Zurita, and M. Stratmann,* Global Analysis of Nuclear Parton Distributions, Phys. Rev. D **85** (2012) 074028 [1112.6324].

[246] **ALICE** *Collaboration,* Upgrade of the ALICE Time Projection Chamber, *Oct, 2013. CERN-LHCC-2013-020, ALICE-TDR-016, https://cds.cern.ch/record/1622286.*

[247] **ALICE** *Collaboration,* Technical Design Report for the Upgrade of the ALICE Inner Tracking System, *Nov, 2013. CERN-LHCC-2013-024, ALICE-TDR-017, https://cds.cern.ch/record/1625842.*

[248] *F. Arleo and S. Peigné,* Disentangling Shadowing from Coherent Energy Loss using the Drell-Yan Process, Phys. Rev. D **95** (2017) 011502 [1512.01794].